Structure and Phase Behavior
of
Colloidal Rod Suspensions

Structure and phase behavior of colloidal rod suspensions
Svyatoslav Viktorovich Savenko
Ph. D. Thesis Utrecht University, May 2006
ISBN: 90-393-4239-3
Cover illustration: Tatyana Abanina ”In the Winter”

Structure and phase behavior
of
colloidal rod suspensions

Structuur en fasengedrag
van
suspensies van colloïdale staven

(met een samenvatting in het Nederlands)

Proefschrift

ter verkrijging van de graad van doctor aan de Universiteit Utrecht op gezag van de rector magnificus, prof. dr. W.H. Gispen, in gevolge het besluit van het College voor promoties in het openbaar te verdedigen op maandag 8 mei 2006 des ochtends te 10.30 uur

door

Svyatoslav Viktorovich Savenko

geboren op 27 december 1978 te Odessa, USSR

Promotor: Prof. dr. A. van Blaaderen
Co-promotor: Dr. M. Dijkstra

Contents

1

Introduction

1.1 Liquid crystals

Gas, liquid and solid are known as the three states of matter. The solid phase is recognized by preserving the volume and the shape of a specimen and is usually associated with low temperatures (and high pressures), an ice for example. As the temperature increases at sufficiently high pressure the solid melts and the liquid state is obtained, an ice transforms into water. This phase is still hardly compressible, but does not keep its shape, water flows. Increasing the temperature further the water starts to boil and the gaseous phase appears. Gases retain neither volume nor shape and tend to fill all the volume available.

In addition to the three basic states of matter, liquid crystalline phases are possible for anisotropic particles. The properties of matter in the liquid-crystalline state are intermediate between those of an isotropic liquid and of a crystalline solid. Like liquids, liquid crystals lack true long-range translational order, but at the same time the molecules maintain long-range orientational order, and are just like crystalline solids anisotropic.

Let us consider the particle properties that are responsible for the existence of all the phases. As Van der Waals showed in 1873 the gas-liquid transition can be explained by assuming that the atoms and the molecules attract each other at large distances, and repel each other at short distances. Computer simulation studies in 1957 revealed the presence of a crystalline phase in a system of hard spheres, showing that attractive forces are not required for crystallization. The origin of the liquid crystalline phases lies in the anisotropy of the interactions between the particles. In this case not only positional degrees of freedom, but also orientational ones should be taken into account. The introduction of orientational degrees of freedom leads to a large variety of orientationally and/or partially spatially ordered states, called mesophases or liquid crystals.

The discovery of liquid crystals is attributed to Reinitzer [1] who noted that cholesteryl benzoate exhibits an unusual type of melting, consisting of two melting points: at 145.5 °C

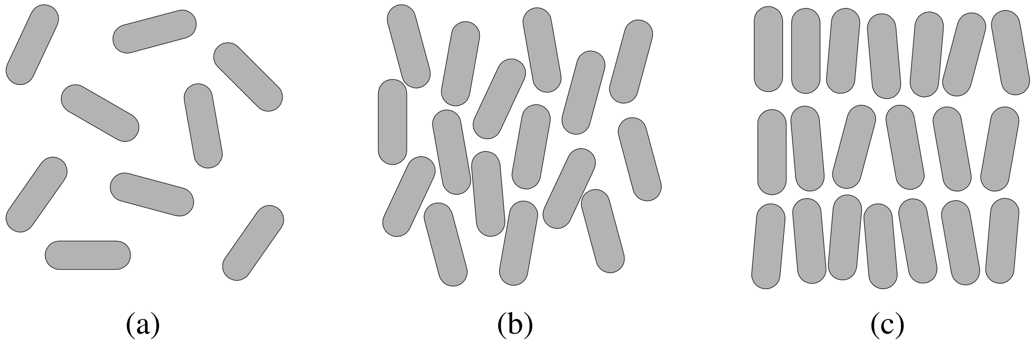

Figure 1.1: Schematic representation of (a) an isotropic fluid phase, (b) a nematic liquid crystalline phase, (c) a smectic liquid crystalline phase.

the solid melts into a cloudy liquid which becomes clear at 178.5 °C. Subsequent studies established that the intermediate phases of cholesteryl benzoate and a number of other compounds represent new states of matter that are distinct from the isotropic liquid phase. Depending on the precise details of the molecular interactions, the system may pass through one or more mesophases before it is transformed into the isotropic liquid. Transitions to liquid crystalline phases may be driven by thermal processes (thermotropic liquid crystals) or by the influence of solvents (lyotropic liquid crystals).

Thermotropic and lyotropic liquid crystals are classified broadly into three types: nematic, cholesteric and smectic [2]. The nematic liquid crystal has a high degree of long-range orientational order of the molecules, but no long-range translational order. It differs from the isotropic fluid in the sense that the molecules are spontaneously oriented with their long axes approximately parallel. The preferred direction usually varies from point to point in the medium, but a homogeneously aligned specimen is optically uniaxial, positive and strongly birefringent. The mesophase is fluid and at the same time anisotropic because of the ease with which the molecules can slide along each other whilst still retaining their parallelism. The cholesteric mesophase is also a nematic type of liquid crystal except that it is composed of optically active molecules. As a consequence the structure has a screw axis superimposed perpendicular to the preferred molecular direction. Optically inactive molecules or racemic mixtures result in a helix of infinite pitch which corresponds to the true nematic. Thermodynamically, the cholesteric is very similar to the nematic. Smectic liquid crystals have stratified structures but a variety of molecular arrangements are possible within each stratification. In smectic A the molecules are upright in each layer with their centers irregularly spaced in a 'liquid-like' fashion, thus the smectic-A phase is orientationally ordered, positionally ordered in only one direction, and disordered in the other two. The thickness of the layer is of the order of the length of a single molecule. The interlayer attractions are weak as compared with the lateral forces between molecules and consequently the layers are able to slide over each other relatively easily. Thus this mesophase has fluid properties, though it is usually very much more viscous than the nematic mesophase. In this thesis I focus on suspensions of rod-like colloidal particles, which are classified as lyotropic liquid crystals. These systems can be synthesized in a chemical laboratory or may be obtained from biological systems.

Examples are inorganic colloidal particles (V_2O_5), β-FeOOH, γ-AlOOH, rodlike micelles, DNA, etc. Probably the best examples of rodlike particles are virus particles such as the tobacco mosaic virus (TMV) and the fd-virus. TMV is a cylindrical particle consisting of a rigid protein shell enclosing double stranded RNA, while the cylindrical fd-virus particle consists of a rigid protein shell wound around a single ribbon of a single stranded DNA. Viewed at low resolution in an electron microscope, TMV appears as a rigid rod of length $L = 3000$Å and diameter $D = 180$Å and light-scattering studies do not detect any flexibility. In addition, in the pH range of 7-8 TMV has a high negative charge density distributed uniformly along its length. It was first recognized in 1936 that suspensions of TMV formed a nematic phase at a sufficiently high particle concentration. TMV had also been observed to form more highly ordered phases, although the identification of the phases had remained to be determined. Recently the smectic and cholesteric phases in suspensions of fd-virus were identified and the kinetics of the transition was studied [3, 4]. As early as 1939 Best [5] studied the phase diagram of TMV as a function of added salt. Without added salt there is coexistence between an isotropic phase of 15 mg ml^{-1} and a nematic phase of 23 mg ml^{-1}. As the ionic strength increased the concentrations of virus in the coexisting phases increased but the ratio of concentrations remained constant. In 1989 Fraden *et al* [6] measured the coexisting isotropic and nematic phases over a wide range of ionic strengths. They showed that replacing the electrostatic potential between TMV particles by a hard-rod interaction with an appropriate effective diameter and subsequently using this effective diameter (and of course the corresponding packing fraction) gives a reasonably good description of their experimentally observed phase boundaries.

Experimental techniques that are frequently used to distinguish the different phases are e.g. birefringence measurements and x-ray diffraction. Usually, the X-ray diffraction pattern of rod-like molecules in the nematic phase consists of two partially oriented diffuse rings. One diffuse ring located at small angles corresponds roughly to the interparticle scatter whereas the wide angle ring is related to the intraparticle scatter. The same type of diffraction pattern was also observed in the nematic phase of side-chain polymers. The orientational distribution function and the nematic order parameter is usually obtained through the inspection of the 'wide angle diffuse ring' which in side-chain polymers is due to lateral interference between side groups. This procedure is based on the treatment of Leadbetter and coworkers, [7] and recently Purdy *et al* [8] have shown that the same type of analysis can be applied to small-angle diffraction patterns producing results, which are in good agreement with birefringence measurements.

1.2 Overview of theoretical results

1.2.1 Onsager model

The first microscopic theory for the isotropic-nematic (I-N) phase transition in a hard-rod system was developed by Onsager [9]. Onsager modeled a TMV suspension as a fluid of long rods of length L and diameter D with an aspect ratio $L/D \to \infty$. In the case of nematic liquid crystals a non-uniform orientational distribution function $f(\Omega)$, which gives the probability density of finding a (rigid) particle with an orientation characterized by the solid angle Ω has to be taken into account. This orientational distribution function is normalized as

$$\int d\Omega f(\Omega) = 1. \tag{1.1}$$

In the isotropic phase all orientations are equally probable and the orientational distribution function is given by

$$f_{iso}(\Omega) = \frac{1}{4\pi} \tag{1.2}$$

which is compatible with the normalization (1.1). Considering particles with different orientations as different species Onsager derived the following expression for the Helmholtz excess free energy

$$\frac{\beta\Delta F}{N} = \int d\Omega f(\Omega)\ln[4\pi f(\Omega)] - \frac{1}{2}\int d\Omega_1 d\Omega_2 f(\Omega_1)f(\Omega_2)v_{exc}(\Omega_1,\Omega_2) \tag{1.3}$$

where the first contribution is the orientational (or mixing) entropy, and the latter term is the second virial coefficient, i.e. the cluster integral averaged over all mutual orientations. This term can be seen as the entropy of packing. The volume excluded to a rod with orientation Ω_1 due to presence of another rod with orientation Ω_2 is denoted by $v_{exc}(\Omega_1,\Omega_2)$. If we model the rods by spherocylinders which consist of a cylindrical part with length L and diameter D and two hemispheres of diameter D at both ends, the excluded volume reads

$$v_{exc} = 2L^2D|\sin\gamma| + 2\pi D^2L + \frac{4}{3}\pi D^3 \tag{1.4}$$

where γ is the angle between two spherocylinders. Although for rods with finite diameter the virial expansion converges slowly, Onsager showed that $B_3^{iso}/(B_2^{iso})^2 \propto \frac{D}{L}(\ln\frac{L}{D} + const)$, and thus the expression (1.3) is exact in the limit of infinitely thin rods.

Minimization of the functional (1.3) can be performed either numerically, or by assuming some functional form for the orientational distribution function with one or more variational parameters. The free energy is then obtained by minimizing it with respect to these parameters. In the original work of Onsager the following expression for the distribution function was chosen

$$f_O(\cos\theta) = \frac{\alpha\cosh(\alpha\cos\theta)}{4\pi\sinh\alpha} \tag{1.5}$$

which works reasonably well. Resulting coexistence number densities are $(\pi/4)L^2D\rho_I = 3.340$, $(\pi/4)L^2D\rho_N = 4.486$, while the numerical solution gives $(\pi/4)L^2D\rho_I = 3.290$, $(\pi/4)L^2D\rho_I = 4.191$.

Although the Onsager theory is exact in the limit of infinitely thin rods, subsequent studies [10, 11] showed that the Onsager theory describes the isotropic-nematic transition well for rods with length-to-diameter ratios $L/D \geqslant 100$. Moreover this theory shows that the isotropic-nematic transition can be driven by entropy alone.

1.2.2 Spherical harmonic expansion of correlation functions

To provide an accurate theoretical description of systems of rods with *finite* length-to-diameter ratio, higher order virial coefficients should be incorporated. One of the most successful approaches in theories of simple fluids is the integral equation theory, which is based on the Ornstein-Zernike equation

$$h(12) = c(12) + \int d3\rho(3)c(13)h(32), \tag{1.6}$$

It relates the total pair correlation function $h(12)$ of two particles to a direct correlation function $c(12)$. While $h(12)$ describes the real correlations between two particles, $c(12)$ only involves their direct correlation, i.e. excluding the indirect correlation which is transmitted through correlations with other particles in the neighborhood. Equation (1.6) must be supplemented by a second relation for both correlation functions, which reflects the interaction between the particles. A number of such closure relations were proposed, among which the Percus-Yevick and hypernetted chain are the most generally known. Unfortunately, the state of affairs is less advanced for non-spherical particles because of the extra angular variables.

To treat the angular variables in $h(12)$ and $c(12)$ Blum and Toruella [12] suggested to expand all the angular dependencies in a complete set of rotational invariants, which for linear molecules can be written as

$$f(\mathbf{r},\omega_1,\omega_2) = \sum_{l_1 l_2 l} f_{l_1 l_2 l}(r)\Phi_{l_1 l_2 l}(\omega_r,\omega_1,\omega_2), \tag{1.7}$$

with the functions $\Phi_{l_1 l_2 l}(\omega_r,\omega_1,\omega_2)$ defined as

$$\Phi_{l_1 l_2 l}(\omega_r,\omega_1,\omega_2) = \sum_{m_1 m_2 m} C(l_1 l_2 l; m_1 m_2 m) Y_{l_1 m_1}(\omega_1) Y_{l_2 m_2}(\omega_2) Y^*_{lm}(\omega_r), \tag{1.8}$$

where $C(l_1 l_2 l; m_1 m_2 m)$ are the Clebsch-Gordan coefficients, and $Y_{lm}(\omega)$ the spherical harmonics.

The harmonic expansions are convenient for calculating correlation functions by computer simulations. The Ornstein-Zernike equation can be rewritten in terms of the harmonic expansion coefficients as [13]

$$\begin{aligned} h_{l_1 l_2 l}(k) &= c_{l_1 l_2 l}(k) + (4\pi)^{-\frac{3}{2}}\rho \sum_{l_3 l' l''} c_{l_1 l_3 l'}(k) h_{l_3 l_2 l''}(k) \\ &\quad \times (-)^{l_1+l_2+l_3}(2l'+1)(2l''+1)\begin{pmatrix} l' & l'' & l \\ 0 & 0 & 0 \end{pmatrix}\begin{Bmatrix} l_1 & l_2 & l \\ l'' & l' & l_3 \end{Bmatrix}. \end{aligned} \tag{1.9}$$

Although this may seem complicated at first sight, the simple Ornstein-Zernike structure in (1.9) is apparent, and the equation is not difficult to use in practice.

1.3 Simulations

Computer simulations are in between experimental measurements and theories of condensed matter. Typically the aim of a theory is to predict the properties of a system in terms of the interactions between the molecules. However, theory is always based on a model system, and when disagreement with experiments is found one likes to know whether the theory is wrong or the model is inappropriate. Computer simulations play the role of an experiment designed to test both the model and the theory, providing ‘exact’ numbers corresponding to the model. There are basically two approaches to molecular simulations, the first one is the Monte Carlo scheme based on the calculation of statistical sums by integration over a set of random points in phase space (usually distributed with some weight) [14], hence it allows to calculate ensemble averages. Another one is the Molecular Dynamics scheme [15], in which the equations of motion are numerically solved, thus recovering the evolution of the model system, and allowing to calculate time averages.

1.3.1 Monte Carlo Simulations

Simulations usually aim to calculate average values of observables A like internal energy or order parameters. The average value $\langle A\rangle$ can be calculated as a phase space integral

$$\langle A\rangle = \int d\Gamma A(\Gamma)f(\Gamma). \tag{1.10}$$

Here Γ is a point in the phase space $(\mathbf{r}_1,\ldots,\mathbf{r}_n,\mathbf{p}_1,\ldots,\mathbf{p}_n)$, and $f(\Gamma)$ is the distribution function (probability density) in the phase space. The idea of Monte Carlo simulations is to estimate this integral by sampling the values of A on a set of configurations distributed in phase space with probability density $f_0(\Gamma)$

$$\langle A\rangle = \int d\Gamma f_0(\Gamma)\frac{A(\Gamma)f(\Gamma)}{f_0(\Gamma)} \approx \frac{1}{M}\sum_{j=1}^{M}\frac{A(\Gamma_j)f(\Gamma_j)}{f_0(\Gamma_j)}. \tag{1.11}$$

Usually it is convenient to use a phase space distribution with probability density $f_0(\Gamma) = f(\Gamma)$ which can be achieved by using the Metropolis algorithm described below.

In the canonical ensemble (NVT), in which the number of particles N, volume V and temperature T are fixed, the distribution function $f(\Gamma)$ is given by

$$f(\Gamma) = \frac{\exp\left(-\beta H(\Gamma)\right)}{Z}, \tag{1.12}$$

where $H(\Gamma)$ is the Hamiltonian of the system, and $Z = \int d\Gamma \exp\left(-\beta H(\Gamma)\right)$ is the canonical partition function.

Generating a set of points distributed in phase space with a probability density $f(\Gamma)$ can be performed using the Metropolis algorithm [14]. A numerical representation of the Markov process $\Gamma_1, \Gamma_2, \ldots$ is generated through the transition probability

$$P(\Gamma_j \rightarrow \Gamma_{j+1}) = p(\Gamma_j \rightarrow \Gamma_{j+1}) \times acc(\Gamma_j \rightarrow \Gamma_{j+1}), \tag{1.13}$$

where $p(\Gamma_j \rightarrow \Gamma_{j+1})$ is the probability of trying the new phase space point Γ_{j+1} if the current configuration is Γ_j, and $acc(\Gamma_j \rightarrow \Gamma_{j+1})$ is the probability to accept this change. Assuming that the trial probability is symmetric $p(\Gamma_j \rightarrow \Gamma_{j+1}) = p(\Gamma_{j+1} \rightarrow \Gamma_j)$ (which is not always the case) one can write

$$acc(\Gamma_j \rightarrow \Gamma_{j+1}) = \min\left(1, \frac{f(\Gamma_{j+1})}{f(\Gamma_j)}\right). \tag{1.14}$$

Now since

$$\frac{f(\Gamma_{j+1})}{f(\Gamma_j)} = \exp(-\beta[H(\Gamma_{j+1}) - H(\Gamma_j)]), \tag{1.15}$$

the acceptance probability can be calculated without knowing the partition function Z. A good test for the validity of a Monte Carlo scheme is the so called ‘detailed balance’ condition

$$P(\Gamma_j \rightarrow \Gamma_{j+1})f(\Gamma_j) = P(\Gamma_{j+1} \rightarrow \Gamma_j)f(\Gamma_{j+1}), \tag{1.16}$$

which is important for developing novel Monte Carlo schemes.

Time plays no role in Monte Carlo simulations, and thus only the equilibrium properties can be extracted by this method. Discussions of extensions of the Monte Carlo method to calculate some dynamical properties can be found elsewhere [16].

1.3.2 MC Simulations of hard rod fluids

An efficient way to generate a new trial configuration is to start from the previous one and to perform a random displacement of one or more molecules, i.e. to perform a trial move. If the move is accepted we sample the variables of interest and continue, if not, we retreat to the previous configuration. It is important to perform sampling even if the move is rejected, such that the contribution from the given configuration gets properly weighted. In the case of non-spherical particles one should generate not only positional but also orientational moves. The new orientation should be uniformly distributed in some solid angle around the previous one.

In Monte Carlo simulations of hard-core fluids, only those trial moves are accepted that do not lead to hard-core overlap of the particles, and they are rejected otherwise. This requires an efficient evaluation of a pair overlap function. The simulations presented in this thesis are performed on a model liquid crystal consisting of hard spherocylinders, for which simple and efficient overlap criteria are developed [17].

Just as a sphere can be defined as a set of points that are within a distance R from a given origin, so the spherocylinder can be thought of as a set of points that are within a distance R from a line segment of length L. Thus, the test for overlap between two spherocylinders can be constructed by computing the shortest distance between the two line segments that form the 'core' of the spherocylinders. If this distance of closest approach is less then $D_{12} \equiv R_1 + R_2$, the two spherocylinders overlap.

To find the closest approach distance for two segments it is convenient to solve first the corresponding problem for infinite lines. Any point on a line can be described parametrically as

$$\mathbf{r}(\lambda) = \mathbf{r}(\lambda = 0) + \lambda \hat{\mathbf{n}}, \tag{1.17}$$

where $\hat{\mathbf{n}}$ determines the orientation of the line, and $\mathbf{r}(\lambda = 0)$ is chosen to be the center of the corresponding segment. The distance between two points on these lines is given by

$$\mathbf{r}_{12}(\lambda_1, \lambda_2) = \mathbf{r}_{12} + \lambda_2 \hat{\mathbf{n}}_2 - \lambda_1 \hat{\mathbf{n}}_1. \tag{1.18}$$

Minimizing the $|\mathbf{r}_{12}|^2$ with respect to the parameters λ_1, λ_2 yields a linear set of two equations which can be solved easily

$$\begin{pmatrix} \lambda_1 \\ \lambda_2 \end{pmatrix} = \frac{1}{1 - (\hat{\mathbf{n}}_1 \hat{\mathbf{n}}_2)^2} \begin{pmatrix} -\hat{\mathbf{n}}_1 \cdot \mathbf{r}_{12} + (\hat{\mathbf{n}}_1 \cdot \hat{\mathbf{n}}_2)(\hat{\mathbf{n}}_2 \cdot \mathbf{r}_{12}) \\ +\hat{\mathbf{n}}_2 \cdot \mathbf{r}_{12} - (\hat{\mathbf{n}}_1 \cdot \hat{\mathbf{n}}_2)(\hat{\mathbf{n}}_1 \cdot \mathbf{r}_{12}) \end{pmatrix}. \tag{1.19}$$

We now have to verify if there is an overlap on two line segments of length L_i. If both λ_1, λ_2 belong to the line segments ($|\lambda_i| \leqslant L_i/2$) then the distance of the closest approach between two line segments is given by (1.19). Otherwise one should use only one of the equations and replace λ_i for which $|\lambda_i| > L_i/2$ by the closest end of the line segment to λ_i.

1.3.3 Phase diagram

Fluids consisting of hard spherocylinders serve as a simple model to investigate general properties of fluids of anisotropic molecules as well as a reference state to study more complicated systems. In this respect the equation of state and the phase diagram of hard spherocylinders is crucial for any subsequent study on this subject.

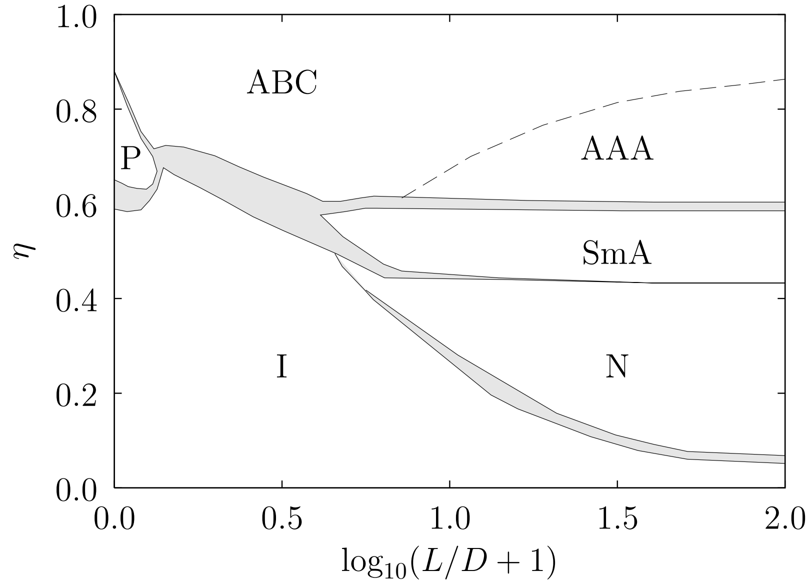

Figure 1.2: Phase diagram of hard spherocylinders with length-to-diameter ratio $0 \leqslant L/D \leqslant 100$. In order to give equal emphasis to all parts of the phase diagram the spherocylinder packing fraction $\eta = \pi D^3 N/6V(1 + 3L/2D)$ is plotted as a function of $\log(L/D + 1)$. The phases are denoted by I (isotropic), N (nematic), SmA (smectic-A), P (plastic crystal), ABC (crystal with ABC layer stacking), AAA (crystal with AAA stacking). Gray areas correspond to coexistence regions and the tielines connecting the coexisting phases are vertical. Based on the data from [18].

Hard spherocylinders exhibit most of the phases observed in experiments, and below we describe the phase diagram based on the data calculated in [18]. At sufficiently low packing fractions $\eta = \pi D^3 N/6V(1+3L/2D)$ the system is isotropic. As η increases the phase behavior of the system depends on the elongation of the particles. Particles with anisotropy larger then $L/D \gtrapprox 3.7$ exhibit a first order isotropic-nematic transition, while for smaller elongations the isotropic phase coexists immediately with an ABC crystal phase. For yet smaller anisotropies $L/D \lessapprox 0.4$ the plastic phase enters, which in turn transforms to an ABC crystal upon increasing the packing fraction. For longer rods the nematic phase transforms into a smectic upon compression. This transition is of first order for moderate particle anisotropies while the order of the transition remains still an open question in the limit of infinitely thin particles [18, 19]. The smectic phase is followed by the ABC crystal phase for anisotropies $L/D \lessapprox 0.7$, while for larger anisotropies the AAA crystal phase appears first, subsequently turning into ABC at densities close to the maximum packing limit. Typical configurations of the phases are shown in figure 1.3.

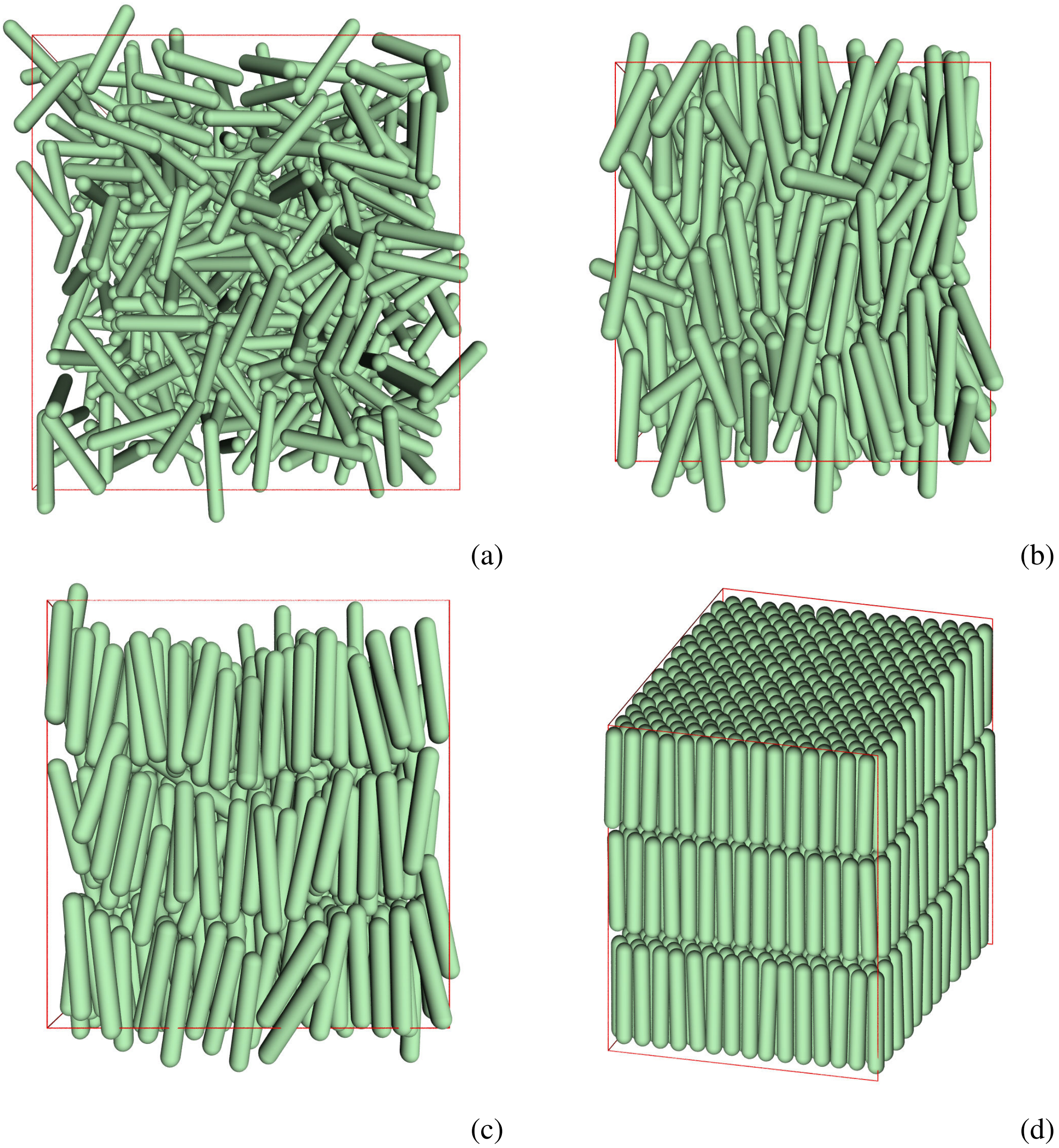

Figure 1.3: Typical configurations of a system consisting of hard spherocylinders with a length-to-diameter ratio $L/D = 5.0$. a) Isotropic $\eta = 0.20$, b) nematic $\eta = 0.43$, c) smectic-A $\eta = 0.55$ and d) ABC crystal $\eta = 0.80$ phases are demonstrated.

2

Sedimentation and multi-phase equilibria in suspensions of colloidal hard rods

Sedimentation and multi-phase equilibria in a suspension of hard colloidal rods are explored by analyzing the (macroscopic) osmotic equilibrium conditions. We observe that gravity enables the system to explore a whole range of phases varying from the most dilute phase to the densest phase, i.e., from the isotropic (I), nematic (N), smectic (Sm), to the crystal (K) phase. We determine the phase diagrams for hard spherocylinders with a length-to-diameter ratio of 5 for a semi-infinite system and a system with fixed container height using a bulk equation of state obtained from simulations. Our results show that gravity leads to multiphase coexistence for the semi-infinite system, as we observe I, I+N, I+N+Sm, or I+N+Sm+K coexistence, while the finite system show I, N, Sm, K, I+N, N+Sm, Sm+K, I+N+Sm, N+Sm+K, and I+N+Sm+K phase coexistence. In addition, we compare our theoretical predictions for the phase behavior and the density profiles with Monte-Carlo simulations for the semi-infinite system and we find good agreement with our theoretical predictions.

2.1 Introduction

Gravity is often non-negligible in colloidal suspensions, as the gravitational energy becomes comparable to the thermal energy for colloid sizes of about a micrometer. Hence, a spatial inhomogeneous suspension is obtained due to the gravitational field, which is characterized by a density profile $\rho(z)$ that varies with altitude z. The parameter that is associated with a gravitational field is the so-called gravitational length and reads $\ell = (\beta m g)^{-1}$ where m is the effective or buoyancy mass of the colloidal particle, and $\beta = (k_B T)^{-1}$ the inverse temperature with k_B Boltzmann's constant, and g the gravitational acceleration. Typically, ℓ is of the order of $\mu m - mm$ for colloidal particles. The density profile $\rho(z)$ follows from a competition between minimal energy (all colloids at the bottom) and maximum entropy (a homogeneous distribution in the available volume). In the case of a very dilute colloid concentration or at high altitude, where the suspension becomes sufficiently dilute, the system behaves like an ideal gas and the system obeys the Boltzmann distribution, yielding an exponential density profile with a decay length given by ℓ. In 1910, Jean Perrin measured such a density profile under the microscope which enabled him to determine Boltzmann's constant and hence, Avogadro's number [20]. However when the interactions become important, the density profile becomes highly non-exponential. Density profiles have been calculated for suspensions of hard and charged colloidal spheres using density functional theory [21], and are measured by light scattering techniques [22]. The measured concentration profiles can be inverted to obtain the osmotic equation of state [21–23]. Non-trivial sedimentation profiles have been predicted recently for charged colloids [24–28] (and measured experimentally [29]), colloid-polymer mixtures [30–33], and binary hard-sphere mixtures [34].

In this chapter we consider suspensions of hard rods, which serve as a simple model for colloidal rod-like particles, like the tobacco mosaic virus (TMV), fd virus, boehmite or silica rods. The bulk phase behavior of hard rod fluids has been studied thoroughly in many theoretical and simulation studies [9, 18, 35]. Suspensions of colloidal rods show lyotropic liquid crystalline behavior and form an isotropic, nematic, smectic and crystal phase upon increasing the concentration. Despite the fact that gravity is often non-negligible for colloidal rods, there are only a few theoretical studies that include its effect on the phase behavior [36] and on the structure of the fluid [37]. In this chapter we determine the phase diagram and density profiles from macroscopic equilibrium conditions using the bulk equation of state of hard spherocylinders with a length-to-diameter ratio $L/D = 5$ obtained from Monte-Carlo simulations [38]. We consider two situations: 1) a semi-infinite system that extends to infinity in the vertical z-direction and 2) the finite system. Refs. [36, 37] were both focussed on the finite system, while disregarding the situation of a semi-infinite system. Surprisingly, the phase behavior depends drastically on the boundary conditions of the system. Finally, we compare directly our results derived from macroscopic equilibrium conditions with Monte-Carlo simulations for the semi-infinite system. Moreover, we examine the accuracy of the osmotic equation of state derived from an inversion of the sedimentation profiles of hard spherocylinders.

This chapter is organized as follows. In Sec. 2.2 we describe the model and the macroscopic description of sedimentation equilibria. In Sec. 2.3, we determine phase diagrams for the finite and semi-infinite system. We present Monte-Carlo simulation results in Sec. 2.4 and we end with some concluding remarks in Sec. 2.5.

2.2 Macroscopic description of Sedimentation equilibrium

We consider a system of hard spherocylinders with a length-to-diameter ratio of L/D suspended in a solvent. The suspending solvent is regarded as an incompressible structureless continuum, characterized by its mass density $\tilde{\rho}$. The effective or buoyancy mass of a spherocylinder is according to Archimedes' principle

$$m = m_0 - \tilde{\rho} v \tag{2.1}$$

where m_0 is the bare mass of the rod and $v = \pi(LD^2/4 + D^3/6)$ the volume of the rod. In a gravitational field oriented along the z-direction of the vessel, the rods are subjected to the external potential

$$\phi(z) = mgz \tag{2.2}$$

where z is the vertical coordinate, and g is the gravitational acceleration.

When the particles are not too large and heavy the density does not vary rapidly with height. In this case the macroscopic description of the system is applicable and and the equilibrium condition reads [39]

$$\frac{dP(z)}{dz} = -mg\rho(z). \tag{2.3}$$

where P is the osmotic pressure.

Eq. (2.3) allows us to determine the equation of state of the system from a single measurement of the concentration profile, which is convenient in experimental or simulation studies [21, 23]. The pressure at arbitrary height z can be obtained using

$$\beta P(z) = \beta P(0) - \ell^{-1} \int_0^z dz' \rho(z') \tag{2.4}$$

where $\beta = (k_B T)^{-1}$ and $\ell = (\beta mg)^{-1}$. If the concentration profile $\rho(z)$ is measured, elimination of z between $\rho(z)$ and $P(z)$ leads directly to the osmotic equation of state $P(\rho)$ of the colloidal suspension.

On the other hand, if the temperature is assumed to be constant throughout the sample, the pressure depends only on the local density and Eq. (2.3) can be rewritten as a nonlinear differential equation for $\rho(z)$

$$\frac{d\rho(z)}{dz} = -\frac{\chi_T(\rho)\rho(z)}{\ell}, \tag{2.5}$$

where $\chi_T = (\partial \beta P/\partial \rho)_T^{-1}$ is the reduced osmotic compressibility of the bulk fluid at density ρ. If the osmotic equation of state $P(\rho)$ is known explicitly, the density profile at various values for the gravitational length can be obtained from Eq. (2.5).

2.3 Phase diagrams for colloidal rods in a gravitational field

We determine phase diagrams for colloidal rods in a gravitational field using the macroscopic conditions for sedimentation equilibrium. We model the colloidal rods as hard spherocylinders, for which the bulk phase diagram is well explored [18, 38]. The phase diagram shows an isotropic fluid phase, nematic and smectic A phases, and a crystalline phase. In order to determine the phase behavior for colloidal rods in a gravitational field, we employ fits to the equation of states obtained from Monte-Carlo simulations of hard spherocylinders with a length-to-diameter ratio $L/D = 5$ [38]. We determine the phase diagrams for two situations: 1) a semi-infinite system, and 2) a finite system. We show that the phase behavior depends sensitively on the boundary conditions of the system. Below, we discuss the two situations in more detail.

2.3.1 Semi-infinite system

We first consider the case of a semi-infinite system extending from $z = 0$ to $z = \infty$. We confine N rods in an open rectangular vessel with a horizontal xy cross section of area S. The bottom of the system is located at $z = 0$ and vertical confinement is determined by the gravitational force exerted on the particles. We determine the phase behavior using the values for the pressure at phase coexistence determined by previous simulations in Ref. [38]. Direct integration of Eq. (2.3) using the boundary condition $\int_0^\infty dz\rho(z) = N/S \equiv n_s$, i.e. keeping the number of particles per unit surface fixed, and employing $P(z = \infty) = 0$, yields a simple relation for the pressure at $z = 0$, i.e. at the bottom of the sample

$$P\,(z = 0) = mgn_s. \tag{2.6}$$

Equating the pressure at phase coexistence with the pressure at the bottom of our sample, given by Eq. (2.6), we can determine easily the phase boundaries of our system, i.e. which phase appears at the bottom of our system followed by the more dilute phases at higher altitudes. In Fig. 2.1, three phase boundaries denoted by the solid lines, are shown in the phase diagram for a semi-infinite system. At low gravity, i.e. low values of D/ℓ, and low n_sD^2, we observe an isotropic phase throughout the whole system. This regime is denoted by I in our phase diagram. At higher gravity or n_s, $P(z = 0)$ becomes larger than P_{IN}, i.e. the pressure at I-N coexistence and we observe a nematic phase at the bottom of our sample. At higher altitudes, we still observe an isotropic phase as the system becomes more and more dilute at higher z. Hence, we observe two phases simultaneously in our sample with the densest phase (N) at the bottom and the isotropic phase at the top. When $P(z = 0)$ becomes larger than the pressure P_{NSm} at N-Sm coexistence, we find three-phase coexistence with the smectic phase at the bottom of the container followed by the nematic and the isotropic phase at higher altitudes. For $P(z = 0) > P_{SmK}$, four-phase coexistence is predicted with the crystal phase at $z = 0$. The pressure at Sm-K coexistence is denoted by P_{SmK}. It is worth mentioning that the phase diagram shows one-, two-, three-, and four-phase coexistence regions and that the isotropic phase is always present in a semi-infinite system at sufficiently high altitudes.

2.3.2 Finite system

In the previous subsection we considered a situation of a suspension in an open vessel unlimited in the z-direction, which becomes infinitely dilute in the limit of $\ell \to \infty$, i.e. no gravity. In this section, we consider a suspension of N colloidal rods confined in all directions to a volume V. The bottom of the system is again located at $z = 0$,

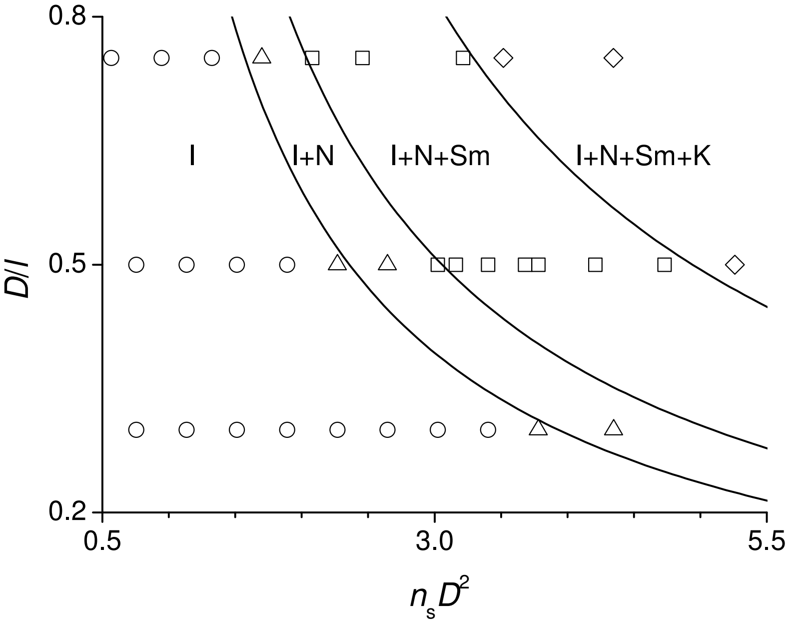

Figure 2.1: Phase diagram for hard spherocylinders (colloidal rods) with $L/D = 5$ in a gravitational field for a semi-infinite system. We plot the gravitational length of the rods D/ℓ versus the number of rods per unit surface $n_s D^2$. The symbols denote the state points employed in our simulations of spherocylinders. ○ denotes the isotropic phase, △ the isotropic-nematic (I+N) coexistence, □ isotropic-nematic-smectic A (I+N+Sm) coexistence, and ◇ isotropic-nematic-smectic A-crystal (I+N+Sm+K) coexistence.

while the height of the vessel H is fixed. In the absence of gravity, the suspension is homogeneously distributed with a uniform density N/V. Employing Eq. (2.5) using the boundary condition $\int_0^H dz\rho(z)/H = N/V$ yields the density at the bottom $\rho(z = 0)$ and at the top $\rho(z = H)$ of the sample from which we can determine the phase diagram. Fig. 2.2 shows the phase diagram in the reduced sample height H/ℓ - dimensionless rod density ρD^3 representation. On the horizontal axis we find bulk coexistence densities of the isotropic-nematic, nematic-smectic, and smectic-crystal transition for zero gravity, i.e. $H/\ell = 0$. At sample heights of about 3 times the gravitational length, we observe an extremely rich phase behavior. For instance, at rod densities $\rho D^3 \sim 0.1$, we find a pure nematic phase at low sample heights, which is sandwiched by a more dilute phase (I) at the top and a denser phase (Sm) at the bottom, as soon as the sample height exceeds $H/\ell = 3.55$. The resulting sample exhibit three-phase coexistence of an isotropic, nematic, and smectic phase. At rod densities $\rho D^3 \sim 0.125$, a pure smectic phase can be transformed in a three-phase (N+Sm+K) coexistence by increasing the sample height. On the other hand, at sample heights $H/\ell \sim 3$, a single I phase can be transformed upon increasing the rod density to a two-phase (I+N) coexistence, a single N phase, N+Sm coexistence, a single Sm, Sm+K coexistence, to a single crystal phase. At sample heights $H/\ell \sim 10$ the sequence is I, I+N,I+N+Sm, N+Sm, N+Sm+K, Sm+K, K, upon increasing the rod density. Four-phase coexistence is observed at rod densities $\rho D^3 \sim 0.115$ at sample heights more than about 11 gravitational lengths. It is worth noting that there are striking differences with the semi-infinite system. When phase coexistence is observed in the semi-infinite system, the most dilute phase at sufficiently high altitudes, is always the isotropic phase.

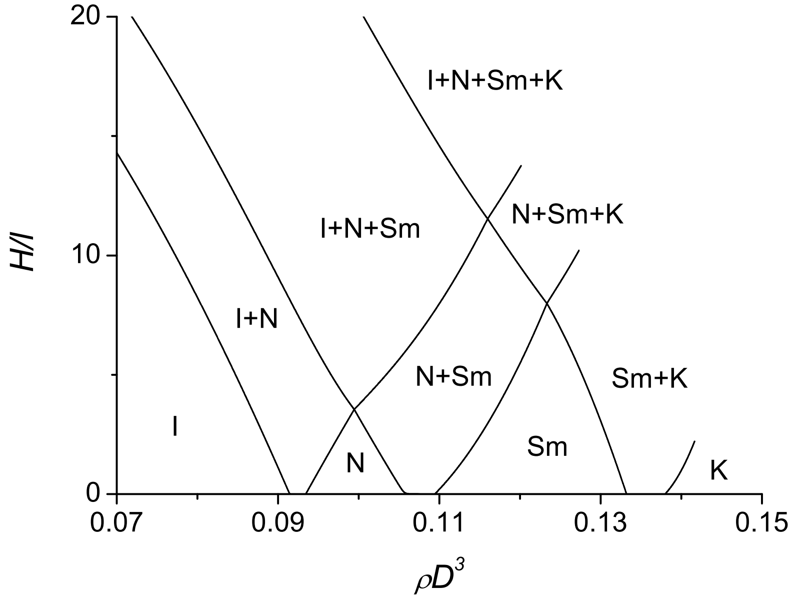

Figure 2.2: Phase diagram for hard spherocylinders (colloidal rods) with $L/D = 5$ in a gravitational field for a closed vessel. We plot the reduced sample height H/ℓ with ℓ the gravitational length of the rods versus the dimensionless rod density ρD^3.

This is not the case in the finite system, yielding many more possibilities for multi-phase coexistence and resulting in a much more complicated phase diagram as shown in Fig. 2.2 compared to the semi-infinite system in Fig. 2.1.

2.4 Simulations

In this section, we present a Monte-Carlo study of a system of hard spherocylinders with a length-to-diameter ratio $L/D = 5$ in a gravitational field. Each spherocylinder consists of a cylindrical part with diameter D and a length L with spherical caps of diameter D at both ends. The bulk phase diagram of hard spherocylinders is well explored [18, 38] and shows a rich phase behavior including isotropic, nematic, smectic A, and crystalline phases. In Ref. [40–42], the interfacial behavior of a hard-rod fluid is investigated using density functional theory and computer simulations. The authors find complete wetting of the nematic phase at the wall-isotropic fluid interface and a uniaxial to biaxial surface transition well below the bulk I-N transition. Moreover, when the hard-rod fluid is confined by two walls, a significant shift of the I-N transition is found to lower densities compared to bulk. In this section, we study the effect of a gravitational field on the phase behavior of hard rods using computer simulations. We compare our theoretical predictions based on the macroscopic equilibrium conditions on the phase diagram with simulation results. We study a system with a fixed number of hard spherocylinders N in a semi-infinite box with lateral dimensions L_x and L_y applying periodic boundary conditions in the x- and y- directions. The z-dimension of the box is infinite. While at $z = 0$ a planar hard wall is located, the rods are free to move upwards. The confinement of the system is implemented by a gravitational field along the z direction. Each rod is subjected to the external potential $\phi(z) = mgz$ with m the buoyancy mass, g the acceleration of gravity, and z the height of the center-of-mass of the rod. The number of particles and the dimensions of the box are varied in the simulations to adjust the pressure at the bottom of the system. The starting configuration is prepared as follows: a closed-packed face-centered-cubic (fcc) lattice of spheres of diameter D with its (001) plane in the xy plane was stretched in the x direction by a factor of $L/D + 1$ in order to accommodate the close-packed crystal of spherocylinders. This lattice was subsequently expanded in x and y direction. For inhomogeneous phases, such as the smectic and crystal phase, it is often essential that the simulation box can change its size (and maybe its shape), in order to accommodate the changes in the phase structures without creating high stresses in the sample. However, as the concentration varies with height in a gravitational field, it is impossible to avoid stresses at each height z. We have chosen the area of the sample such that the phase at the bottom is well-accommodated or is commensurate with the dimensions of the cross-section of the container. We check for equilibrium by monitoring the height of the center of mass of the system. When equilibrium is reached we perform sampling at $\sim 1.5 \times 10^6$ Monte-Carlo cycles (one cycle is one attempted move per particle), the profiles are sampled in bins of width $0.1D$. The sampled quantities are the density profile and the profiles of the eigenvalues of the standard 3×3 nematic order parameter tensor defined as [17]

$$Q_{\alpha\beta}(z_j) = \left\langle \frac{1}{n_j} \sum_{i=1}^{n_j} \frac{3u_\alpha^i u_\beta^i - \delta_{\alpha\beta}}{2} \right\rangle \tag{2.7}$$

where u_α^i is the α-component of the unit orientation vector of particle i with $\alpha = x, y, z$, and n_j is the number of particles present in bin j. The Kronecker delta is $\delta_{\alpha\beta}$. Diagonalizing this tensor gives three orientational ordering eigenvalues λ_+, λ_0, and λ_- for each bin.

We perform simulations of spherocylinders with $L/D = 5$ at three values of the inverse gravitational length $D/\ell = 0.3, 0.5$, and 0.75, and for varying number of particles per unit surface $n_s D^2$. The explicit values for D/ℓ and $n_s D^2$ which are employed in the simulations are displayed by the symbols in Fig. 2.1. We display coarse-grained density profiles for $D/\ell = 0.30$ and 0.75 for varying values of $n_s D^2$ in Figs. 2.3 and 2.4. Similar results were obtained for $D/\ell = 0.50$. We show plots for only a few values of $n_s D^2$ for clarity. At high altitudes (large z) we find that the density tends to zero, while the highest density is observed at the bottom of the sample as expected. For comparison, we also plot the density profiles obtained from Eq. (2.5) and employing the equation of state from Ref. [38]. We find good agreement of the simulation results with the theoretical predictions based on the macroscopic osmotic equilibrium conditions. We, therefore, believe that also the theoretical predictions on the phase behavior are reliable. The density fluctuations due to the ordering of the rods induced by the wall or due to the ordering in the smectic and crystal phase is, of course, missing in the density profiles obtained from the macroscopic osmotic equilibrium conditions. We like to mention that the phase at the bottom of the container, and hence, the phase diagram can be determined by comparing the theoretical or simulation contact densities at $z = 0.5D$ with the bulk coexisting densities. The coexisting densities are determined by McGrother *et al.* using computer simulations [38]. The reduced densities are at I-N coexistence $\rho D^3 = 0.0914$ (I) and $\rho D^3 = 0.0932$ (N), at N-Sm coexistence $\rho D^3 = 0.1061$ (N) and $\rho D^3 = 0.1094$ (Sm), and at Sm-K coexistence $\rho D^3 = 0.1319$ (Sm) and $\rho D^3 = 0.1380$ (K) [38]. For the two lowest density profiles in Figs. 2.3 and 2.4, we find that the contact density is lower than the coexisting density of the nematic phase at I-N coexistence, hence, the whole sample is in the isotropic phase in agreement with the theoretical phase diagram in Fig. 2.1. The contact densities for $n_sD^2 = 4.348$ in Fig. 2.3 and $n_sD^2 = 1.701$ in Fig. 2.4 are higher than the coexisting density of the nematic phase at I-N coexistence, but lower than that at N-Sm coexistence, and we find two-phase coexistence of the isotropic phase and the nematic phase. We find that the contact density for $n_sD^2 = 2.457$ in Fig. 2.4 is higher than the coexisting density of the smectic phase at N-Sm coexistence, but lower than that at Sm-K coexistence. For this state point, we observe three-phase coexistence of a smectic, nematic, and an isotropic phase. For all these density profiles, we find good agreement with the theoretical predictions for the phase behavior, as one might expect on the basis of the good agreement of the density profiles with the theoretical ones. Closer inspection of Fig. 2.1 shows that the I+N coexistence starts at lower n_sD^2 for $D/\ell = 0.5$ and 0.3 compared with the theoretical predictions. A similar shift was also found in previous simulations of a hard-rod fluid in contact with a planar hard wall: the uniaxial to biaxial surface transition occurs well below the bulk I-N transition [40–42]. However, it is impossible to determine the contact density from the density profiles obtained from simulations at high n_sD^2 due to the large density fluctuations close to the wall. Even coarse-graining the density profiles does not give us a sufficiently accurate value for the contact density. However, the appearance of the crystal phase can be observed in the raw (not coarse-grained) density profiles. The inset of Fig. 2.4 shows the raw density profile for $n_sD^2 = 4.34$. We clearly observe the formation of crystalline layers at the bottom and smectic layers at higher altitudes: the density drops to zero between the density peaks close to the wall (crystal phase), while only pronounced peaks are observed at higher z (smectic phase). The system is in the four-phase coexistence region for $n_sD^2 = 4.34$ and $D/\ell = 0.75$. This multi-phase coexistence can also be appreciated from the snapshots in Fig. 2.5 that shows nice crystalline ordering at the bottom of the container in Fig. 2.5c and hexagonal ordering in Fig. 2.5b. At higher altitudes, the hexagonal ordering is destroyed, and a smectic phase appears. The smectic layers disappear at even higher heights as can be seen in Fig. 2.5a, and we observe a nematic phase. At high altitudes, we observe the isotropic phase.

In Fig. 2.6, we plot the order parameter profiles for $D/\ell = 0.75$ and varying values of n_sD^2. In bulk, the value of the largest eigenvalue of this tensor determines the nematic ordering, which is zero for an isotropic fluid phase and one for perfectly aligned rods. In the presence of the wall at the bottom of the sample the lowest eigenvalue of this tensor approaches $-1/2$ as the rods close to the wall have to be oriented parallel to the surface. Consequently, the two largest eigenvalues are equal to $1/4$ when there is no in-plane order, see Fig. 2.6 (the short-dashed lines for $n_sD^2 = 0.567$). The onset of biaxial and nematic ordering at the bottom can be observed from the difference of the two largest eigenvalues, that shows the appearance of a preferred in-plane orientation (the dash-double dotted lines for $n_sD^2 = 1.323$). As n_sD^2 increases this difference increases. The nematic phase appears at the bottom of the container when the largest eigenvalue exceeds 0.5 at $z = 0$ (dash-dot line for $n_sD^2 = 1.701$), which corresponds well with the value of the nematic order parameter of 0.471 for the nematic phase at I-N coexistence [38]. Three-phase coexistence is observed when the largest eigenvalue is roughly 0.9 at the bottom (dotted and dashed line for $n_sD^2 = 2.457$ and 3.51, respectively), again in agreement with the fact that the nematic order parameter of the smectic phase in bulk is about 0.893 at N-Sm coexistence [38]. A crystal phase (solid line for $n_sD^2 = 4.34$) is found at the bottom of the container when the largest eigenvalue approaches 1, while the order parameter of the

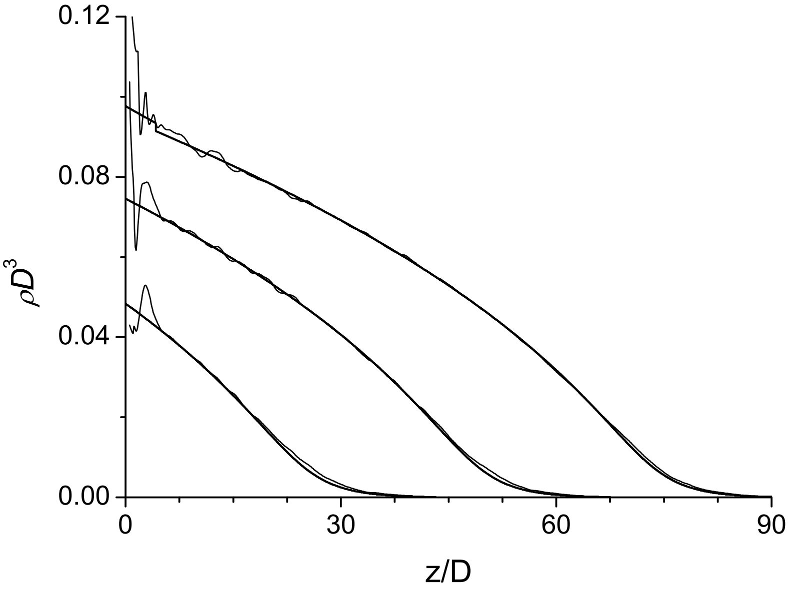

Figure 2.3: Density profiles ρD^3 versus z/D for a semi-infinite system with inverse gravitational length $D/\ell = 0.30$, and for varying number of particles per unit surface $n_s D^2 = 0.756$, 2.268, 4.348 (from bottom to top). The thin lines are the coarse-grained density profiles from computer simulations, while the thick lines are those obtained from Eq. (2.5) using the equation of state of Ref. [38].

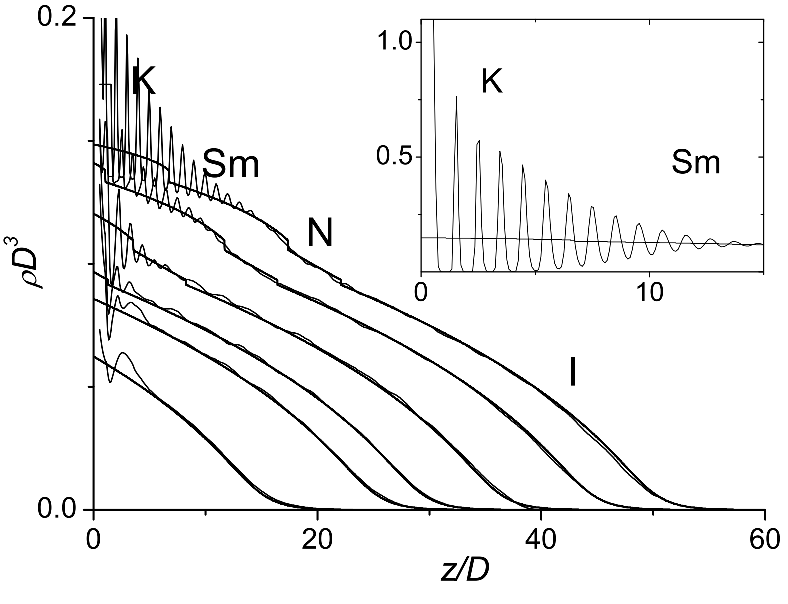

Figure 2.4: Density profiles ρD^3 versus z/D for a semi-infinite system with inverse gravitational length $D/\ell = 0.75$, and for varying number of particles per unit surface $n_s D^2$ of 0.567, 1.323, 1.701, 2.457, 3.51, 4.34 (from bottom to top). The thin lines are the coarse-grained density profiles from computer simulations, while the thick lines are those obtained from Eq. (2.5) using the equation of state of Ref. [38]. The inset shows the raw density profile from simulations for $n_s D^2 = 4.34$.

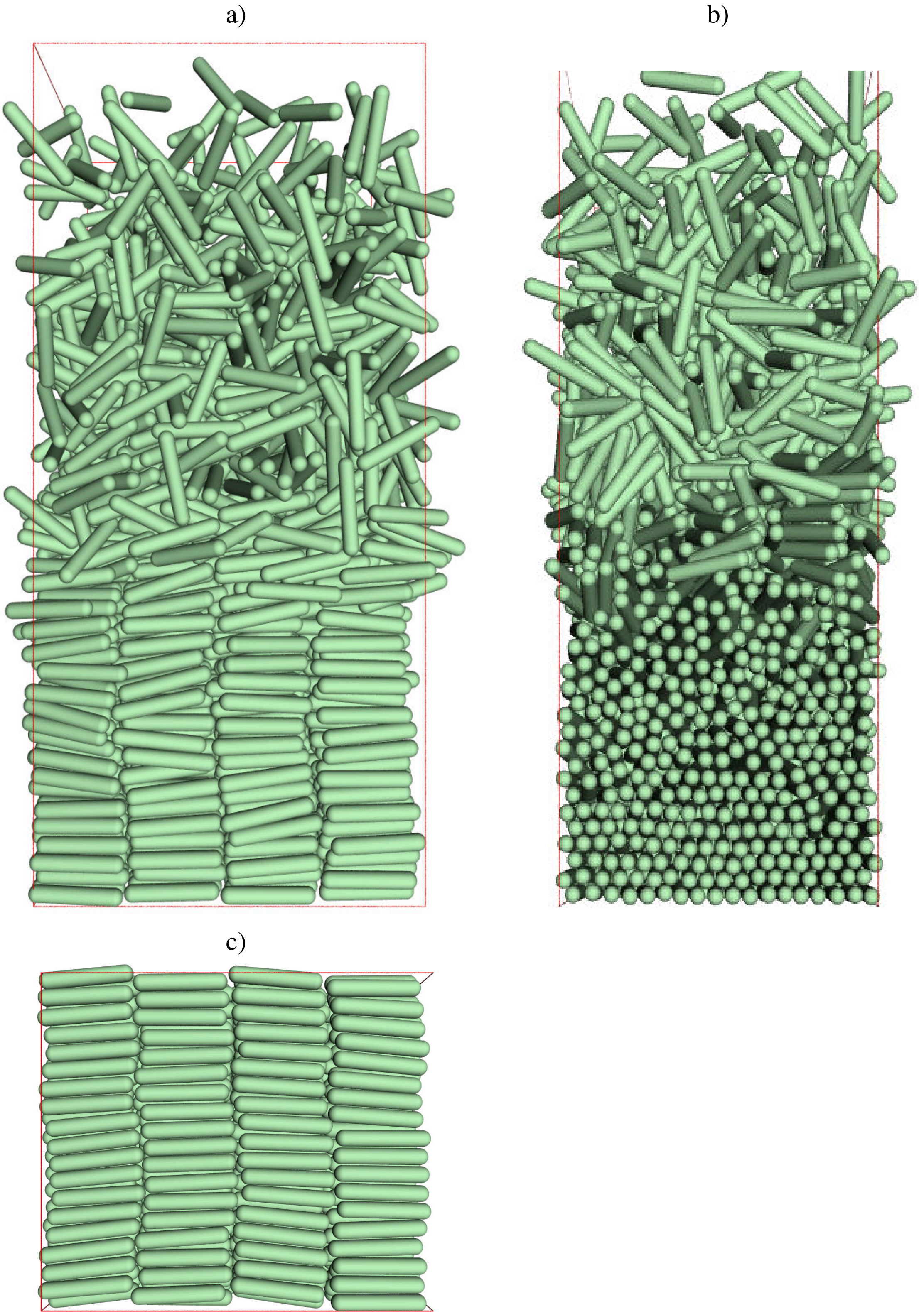

Figure 2.5: Snapshots of typical configurations: two sideviews a) and b), and a bottom view c), obtained from simulations of hard spherocylinders with $L/D = 5$, for number of particles per unit surface $n_s D^2 = 4.34$ and for an inverse gravitational length $D/\ell = 0.75$.

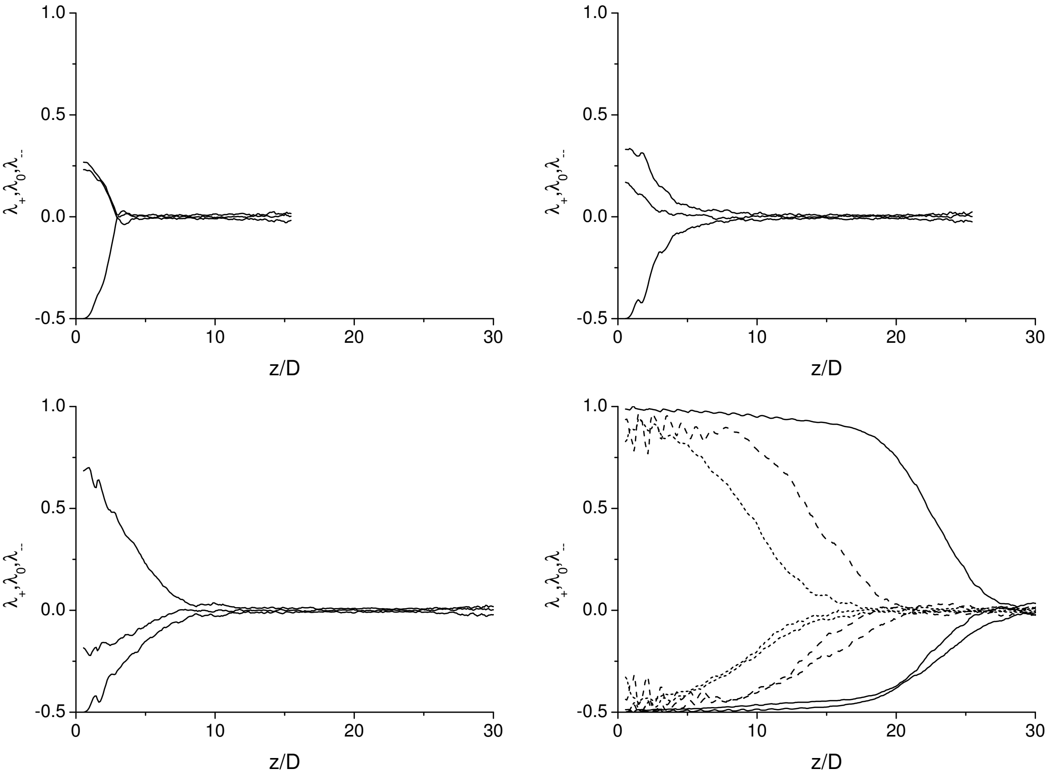

Figure 2.6: The profiles of the eigenvalues λ_+, λ_0, and λ_- of the nematic order parameter tensor (2.7) versus z/D for a semi-infinite system with inverse gravitational length $D/\ell = 0.75$, and varying number of particles per unit surface a) $n_sD^2 = 0.567$, b) $n_sD^2 = 1.323$, c) $n_sD^2 = 1.701$, d) $n_sD^2 = 2.457$ (short-dash), 3.51 (dashed), 4.34 (solid).

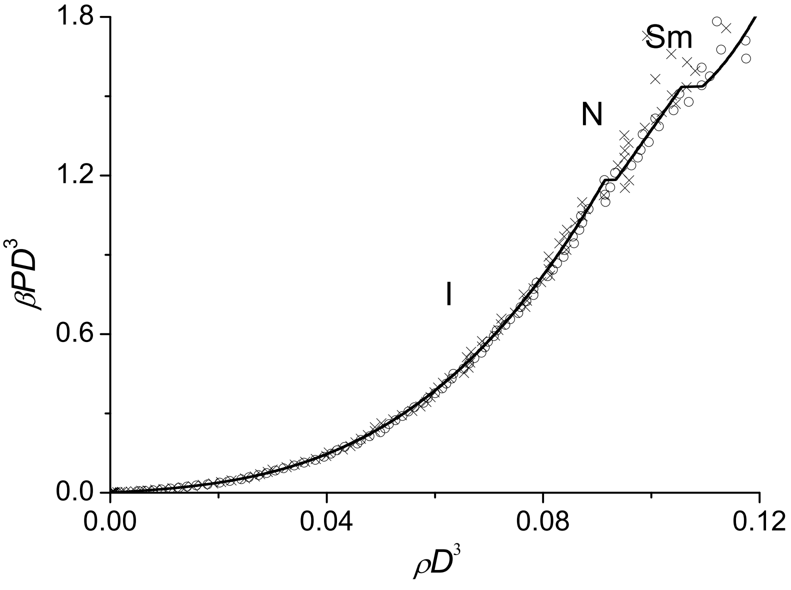

Figure 2.7: Equation of state of hard spherocylinders with a length-to-diameter ratio $L/D = 5$ obtained by inverting the coarse-grained density profiles from Fig. 2.4 versus reduced densities ρD^3 for $n_sD^2 = 3.21$ ($\times$) and $n_sD^2 = 4.34$ ($\circ$), while — represents the bulk equation of state from Ref. [38]

crystal phase in bulk is about 0.974 at Sm-K coexistence [38].

Finally, we obtain the osmotic equation of state for hard spherocylinders by inverting the coarse-grained simulation sedimentation profiles using Eq. (2.4) and by eliminating z between $\rho(z)$ and $P(z)$. In Fig. 2.7, we show the results using the profiles for inverse gravitational length $D/\ell = 0.75$ and number of particles per unit surface $n_s D^2 = 3.21$ and 4.34. For comparison, we also plot the osmotic equation of state obtained from bulk simulations performed at many different densities of Ref. [38] and we find good agreement, even for densities higher than those at I-N coexistence. Similar good agreement of the equation of state of the isotropic *and* of the nematic phase was also found by inverting sedimentation profiles for $D/\ell = 0.30$ and 0.50, and other values of $n_s D^2$ that we considered.

2.5 Conclusions

We have investigated sedimentation and phase equilibria in suspensions of hard spherocylinders with a length-to-diameter ratio $L/D = 5$ by analyzing the (macroscopic) osmotic equilibrium conditions. We present phase diagrams for a semi-infinite system and for a finite system. We find that the phase behavior depends in great detail on the boundary conditions of the system. To the best of our knowledge, we believe that this is the first study that investigates the dependence of the phase behavior on the boundary conditions of the system. In addition, we compare our theoretical predictions for the phase behavior and sedimentation profiles with Monte-Carlo simulations for the semi-infinite system. We find very good agreement between the two sets of results. Moreover, we find excellent agreement of the osmotic equation of state obtained from inverting the coarse-grained sedimentation profiles from a single simulation with the bulk equation of state determined from bulk simulations at many different densities [38], even for densities in the nematic phase. This surprisingly good agreement for densities beyond I-N coexistence can be understood as the interfacial width of the isotropic-nematic interface is very small for the gravitational lengths considered in this work.

It is interesting to study the effect of the addition of an extra component to the sedimentation profiles of a suspension of hard rods, e.g. non-adsorbing polymer that might yield a floating liquid phase similar as was found in Ref. [32, 33] or thinner rods that might give a non-trivial density profile of floating thick rods in a suspension of thin rods similar as Ref. [34]. We plan to study the sedimentation profiles of colloidal rod-mixtures in future work.

Acknowledgments

We thank René van Roij for stimulating discussions and we like to thank the Dutch National Computer Facilities foundation for access to the SGI Origin3800. The High Performance Computing group of Utrecht University is gratefully acknowledged for ample computer time.

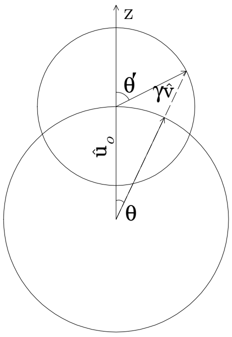

Figure 2.8: Procedure to generate a trial move that changes the initial orientation of a particle $\hat{\mathbf{u}}_0$ which is oriented along the z-axis: 1) Generate a unit vector $\hat{\mathbf{v}}$ with an angle θ' to the z-axis. 2) Scale it by a factor γ. 3) Normalize the sum vector $\gamma\hat{\mathbf{v}} + \hat{\mathbf{u}}_0$. 4) The normalized vector has an angle θ with the z-axis.

2.A A note on rotational moves

Monte-Carlo simulations of molecular systems require an efficient algorithm to generate a new orientation uniformly distributed in a solid angle around the previous orientation. However, several widely used algorithms generate rotational displacements which are not uniformly distributed. Nonuniform distributions act as a local external field, and introduces a bias to the sampling. Here we calculate the local field corresponding to the algorithm described in [43]. First, it suggests to generate a random unit vector $\hat{\mathbf{v}}$, then scale it by a factor γ, which determines the maximum rotation angle, add it to the initial orientation vector $\hat{\mathbf{u}}_o$, and finally normalize the sum $\hat{\mathbf{u}}_n = (\gamma\hat{\mathbf{v}} + \hat{\mathbf{u}}_o)/|\gamma\hat{\mathbf{v}} + \hat{\mathbf{u}}_o|$.

The problem is equivalent of finding the radial projection of the distribution uniform on a sphere with radius γ and its center on the surface of a unit sphere onto this sphere. To this end we need to relate the cosines in the two coordinate systems, one with the origin in the center of the γ- sphere, and another with the origin in the center of the unit sphere

$$\cos\theta' = \frac{\cos^2\theta - 1 \pm \cos\theta\sqrt{\cos^2\theta + \gamma^2 - 1}}{\gamma}, \tag{2.A.1}$$

where plus and minus signs correspond to two possible positions of a point on the γ-sphere corresponding to the same value of $\cos\theta$.

Now, if we generate a uniform random variable x from the distribution $p(x)$ and then take some function $y(x)$ of it, then the probability distribution of y is determined via the transformation law of probabilities

$$|p(y)dy| = |p(x)dx|. \tag{2.A.2}$$

Recalling that a uniform distribution of points on the surface of a sphere implies a uniform distribution of $\cos\theta'$, and that the derivative is given by

$$\frac{\partial\cos\theta'}{\partial\cos\theta} = \frac{1}{\gamma}\frac{(\cos\theta \pm \sqrt{\cos^2\theta + \gamma^2 - 1})^2}{\sqrt{\cos^2\theta + \gamma^2 - 1}},$$

we can easily find the distribution of generated rotational moves on a surface of a unit sphere

$$p(\cos\theta) = \frac{2\cos^2\theta + \gamma^2 - 1}{\gamma\sqrt{\cos^2\theta + \gamma^2 - 1}}. \tag{2.A.3}$$

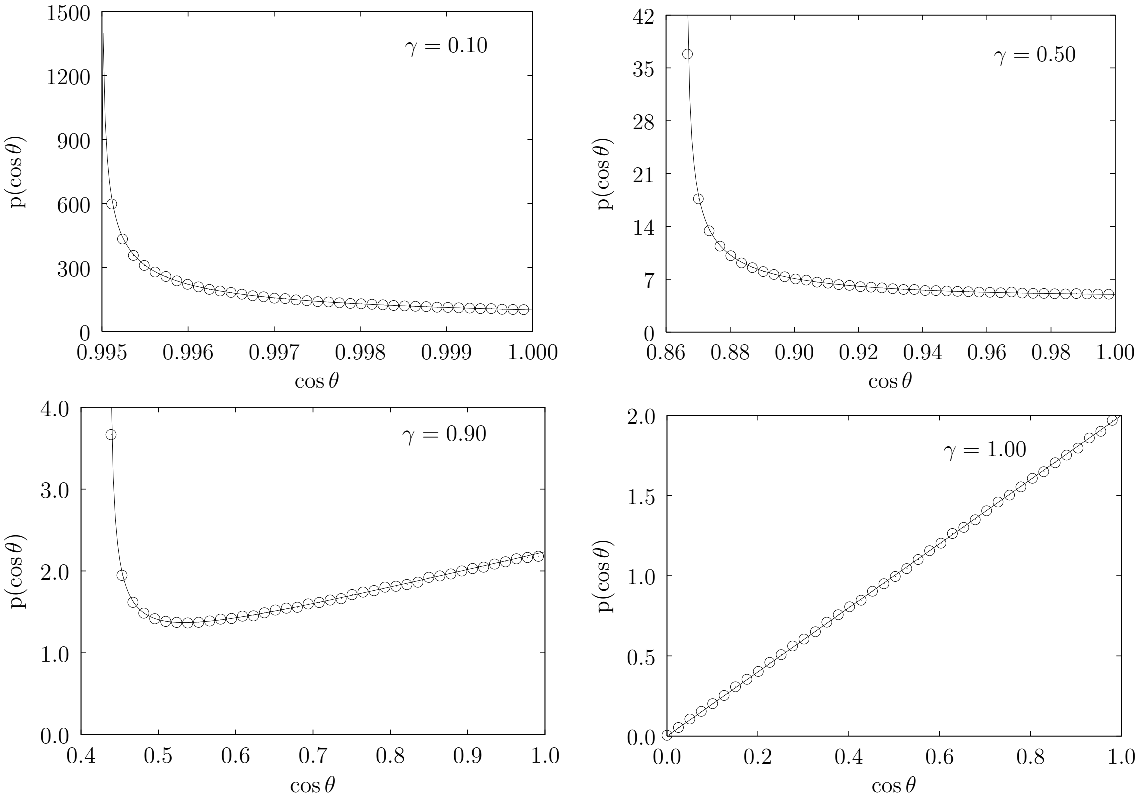

Figure 2.9: The probability distribution of $\cos\theta$ for varying γ. The open circles denote simulation data while Eq. (2.A.3) is denoted by the solid line.

Fig. 2.9 shows the probability distribution $p(\cos\theta)$ using the procedure described above for varying γ. The unbiased $p(\cos\theta)$ should be constant for all possible values of $\cos\theta$. Fig. 2.9 shows clearly that this procedure to generate orientational moves yields a non-trivial non-uniform probability distribution as a function of γ. Changing γ during simulation to adjust the acceptance ratio is even more hazardous. The corresponding local field is given by

$$\beta\varphi(\cos\theta) = -\ln(p(\cos\theta)). \tag{2.A.4}$$

We performed simulations of a bulk nematic phase at varying densities. We found that this scheme does not produce any significant bias for the order parameter. However, we found that in the case of hard platelets in the external field of a hard wall, the system can get trapped in a configuration with the platelets severely absorbed at the wall.

Here we propose another scheme to generate rotational moves uniformly distributed in the angle $\cos\theta_{max} \leqslant \cos\theta \leqslant 1$. The efficiency of this procedure is similar to the previous method. First we generate a unit vector uniformly distributed on a circle in the plane perpendicular to the initial orientation $\hat{\mathbf{u}}_o$, we then generate a random rotation of the initial orientation around this vector.

3

On the accuracy of measuring the nematic order from X-ray diffraction: a simulation study

The determination of the nematic order parameter S and the orientational distribution function (ODF) from scattering data involve severe approximations. The validity of these are studied here using Monte-Carlo simulations of hard spherocylinders with an aspect ratio of 15 for varying densities in the isotropic and nematic phase. The "exact" ODF of the rods, the "exact" value of S, and the scattered intensity $I(\vec{q})$ are determined directly in simulation. In addition, we determine the ODF and S from the simulated scattered intensity which includes spatial and orientational correlations of the particles. We investigate whether correlations present in the interparticle scatter influences the determination of the single particle orientational distribution function by comparing the results obtained from scattering with the "exact" results measured directly in our simulations. We find that the nematic order parameter determined from the scattered intensity underestimates the actual value by 2-9%. We also find that the values of S and the ODF are insensitive to the absolute value of the scattering vector for $1.2\pi < |\vec{q}|D < 2\pi$ which agrees well with the assumption proposed by Leadbetter that $I(q, \psi)$ along the equatorial arc is independent of $|\vec{q}|$. We also observe that the best fit of the "exact" ODF is given by the Maier-Saupe distribution when nematic director fluctuations are ignored, while the Gaussian distributions provides the best fit when these fluctuations are included.

3.1 Introduction

Liquids consisting of anisotropic molecules exhibit a number of liquid-crystalline phases, that are intermediate between the well-ordered crystalline solid and the isotropic fluid phase (see Fig. 3.1a). The simplest liquid-crystal phase is the so-called nematic phase, in which the particles exhibit long-range orientational order but no translational order (see Fig. 3.1b). Extensive theoretical and simulation studies are performed on hard-rod fluids, which serve as a good model for rodlike colloidal particles like the inorganic boehmite rods [44] or the biological TMV and fd virus particles [45]. The phase behavior of colloidal hard rods starts with the seminal work of Onsager, who showed that infinitely thin hard rods exhibit an entropy-driven isotropic-nematic phase transition at sufficiently high densities [9]. Subsequently, extensive computer simulation studies showed that also finite hard rods show a nematic phase [11, 46–48], a smectic phase [11, 46, 47, 49] and a columnar phase [46]. More recently, the phase diagram of hard rods is determined as a function of the aspect ratio and density of the rods [18].

The focus of this chapter is, however, not on the phase behavior as many previous studies, but on the structure of the fluid, in particularly, the single particle distribution and two-body distribution functions. The nematic phase is often characterized by the orientational distribution function (ODF) $f(\theta)$, which is a single-particle distribution function and describes the distribution of orientations of the particles about a preferred direction, i.e., director. The angle between the long molecular axis and the director is denoted by $\theta \in [0, \pi/2]$. This function plays a key role in understanding the properties of nematic phases and many theoretical investigations rely on the explicit functional form of it. The nematic order parameter S of a system is quantified by

$$S = \int_0^{\pi/2} d\theta \sin\theta P_2(\cos\theta) f(\theta) \tag{3.1}$$

where P_2 is the second Legendre polynomial. The orientational distribution function can be determined experimentally by various methods; one of them is based on diffraction experiments, which measures the Fourier transform of a two-body correlation function. It is interesting to investigate how a single-particle distribution can be obtained from measurements of the two-body correlations. If we consider N identical particles with orientations given by the unit vectors $\{\hat{\omega}\}$, and $\rho(\vec{r};\hat{\omega})$ describes the internal (electron) density of each individual particle, then the scattered intensity of the total system is given by

$$\begin{aligned} I(\vec{q}) &= \langle \sum_{i=1}^{N} \sum_{j=1}^{N} \int \int d\vec{r} d\vec{r}' \rho(\vec{r} - \vec{r}_i; \hat{\omega}_i) \rho(\vec{r}' - \vec{r}_j; \hat{\omega}_j) \exp[i\vec{q} \cdot (\vec{r} - \vec{r}')] \rangle \\ &= \langle \sum_{i=1}^{N} \sum_{j=1}^{N} \exp[i\vec{q} \cdot (\vec{r}_i - \vec{r}_j)] \vartheta(\vec{q}; \hat{\omega}_i) \vartheta(-\vec{q}; \hat{\omega}_j) \rangle \end{aligned} \tag{3.2}$$

with $\vartheta(\vec{q};\hat{\omega}_i) = \int d\vec{r} \rho(\vec{r};\hat{\omega}_i) \exp[i\vec{q}\cdot\vec{r}]$, the Fourier transform of the (electron) density distribution $\rho(\vec{r};\hat{\omega}_i)$ of particle i. Note that $\rho(\vec{r};\hat{\omega}_i)$ depends on the orientation of particle i. The total scattered intensity can be split into a part $F(\vec{q})$ that depends on a single-particle distribution function and a second part $S(\vec{q})$ that includes the spatial and orientational correlations

$$I(\vec{q}) = NF(\vec{q})S(\vec{q}). \tag{3.3}$$

The intraparticle scatter or form factor $F(\vec{q})$ is given by

$$F(\vec{q}) = \left\langle |\vartheta(\vec{q};\hat{\omega})|^2 \right\rangle \tag{3.4}$$

and the angular brackets denote an average over all the particles with their orientations given by the unit vectors $\{\hat{\omega}\}$. The interparticle scatter or structure factor term $S(\vec{q})$ reads [50]

$$S(\vec{q}) = 1 + \frac{1}{NF(\vec{q})} \left\langle \sum_{i \neq j}^{N} \exp[i\vec{q} \cdot (\vec{r}_i - \vec{r}_j)] \vartheta(\vec{q};\hat{\omega}_i) \vartheta(-\vec{q};\hat{\omega}_j) \right\rangle . \tag{3.5}$$

The structure factor depends on the positions of the rods and their relative orientations. For spherical symmetric particles, the (electron) density distribution $\rho(\vec{r};\hat{\omega})$ is independent of the orientation of the particle, and $\vartheta(\vec{q};\hat{\omega}_i) = \vartheta(\vec{q};\hat{\omega}_j)$. The structure factor is then decoupled from the form factor. However, for anisotropic density distributions, $\vartheta(\vec{q};\hat{\omega}_i) \neq \vartheta(\vec{q};\hat{\omega}_j)$ and the structure factor is not decoupled from the form factor, hence, the structure factor includes spatial and orientational correlations. In the isotropic and nematic phase, it is often assumed that $S(\vec{q}) \to 1$ at high angle and the intensity depends only on the form factor, i.e., $I(\vec{q}) = F(\vec{q})$. If the intensity can be measured at high angle, the orientational distribution function can be obtained directly from the intensity. At low angle, i.e., $|\vec{q}|D < 2\pi$, the scattering intensity depends on $S(\vec{q})$ which includes angular and spatial correlations between neighboring rods. In our simulations, we observe that $S(\vec{q}) \neq 1$ for $|\vec{q}|D < 2\pi$ and it is interesting to investigate the validity and consequences of the assumption $I(\vec{q}) \simeq F(\vec{q})$ that is often employed experimentally in the determination of S and the ODF from scattered intensity. Leadbetter [7, 51] showed that the intensity distribution along the equatorial arc, thus at fixed $|\vec{q}|$, can be related to the ODF of the sample. The integral equation relating these two quantities was inverted by Deutsch [52]. However, using scattering data that includes experimental errors, a numerical inversion of the integral equation is very inaccurate. Therefore, one often assumes an analytical form of the ODF with some fitting parameters which are chosen such that it provides the best fit of the measured intensity distribution [8, 53, 54]. The resulting ODF and the nematic order parameter derived from the ODF may depend sensitively on the precise trial function of the ODF. The validity of these approaches to measure the nematic order and ODF in scattering experiments was studied by Purdy *et al.* [8] by comparing the nematic order parameter obtained from low angle scattering experiments (which include spatial and orientational correlations) with high angle scattering experiments (which depends only on the single particle ODF). However, both approaches to obtain the nematic order parameter from low and high angle scattering involve approximations and are based on trial functions.

In this chapter we test the validity of these approaches by determining the ”exact” orientational distribution function of the rods, the ”exact” nematic order parameter, and the scattered intensity directly in simulation. We compare the orientational distribution function and nematic order parameter obtained from the simulated scattered intensity using several trial functions with the “exact” results measured directly in our simulations.

The chapter is organized as follows: In Section 3.2 we describe the simulations, Section 3.3 presents the results, and the conclusions are drawn in Section 3.4.

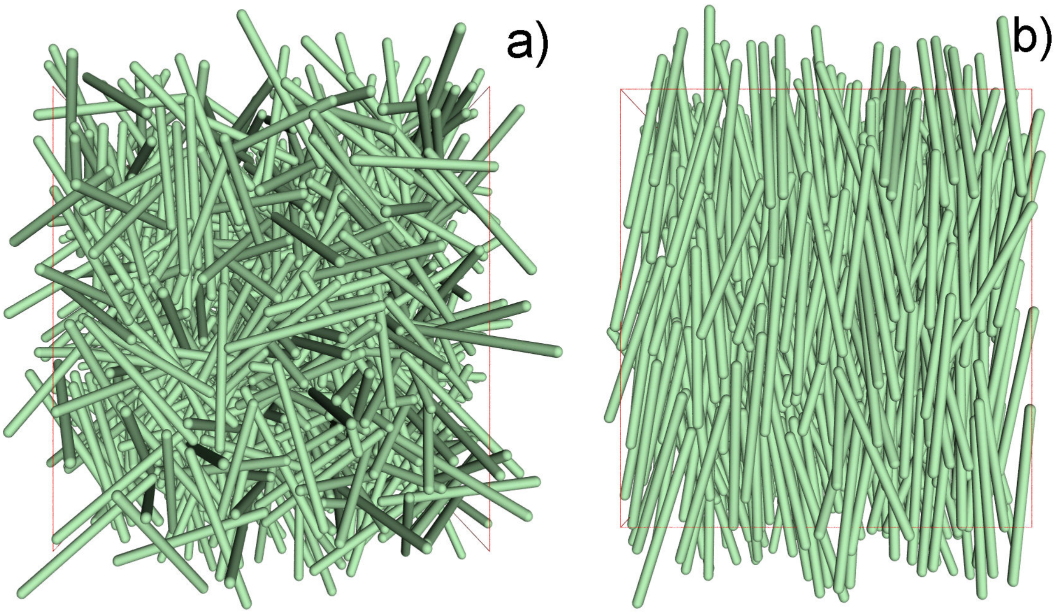

Figure 3.1: Snapshot of a fluid of hard spherocylinders for packing fraction a) $\eta = 0.1723$ (Isotropic phase) and b) $\eta = 0.2338$ (Nematic phase)

3.2 Simulations

Extensive simulation studies are performed to determine the phase behavior of fluids consisting of hard spherocylinders [11, 18, 46, 47, 49]. The focus of this chapter is, however, not on the phase behavior, but on the structure of the fluid, in particularly, the single particle distribution and two-body distribution functions. The ”exact” orientational distribution function of the rods, the ”exact” nematic order parameter, and the scattered intensity are determined directly in simulation. We study a system of hard spherocylinders in a cubic box with periodic boundary conditions. Each rod consists of a cylindrical part with diameter D and length $L = 15D$ and of spherical caps at both ends with diameter D. We present Monte-Carlo simulations in the canonical ensemble, so we fix the number of particles at $N = 1000$, and the volume V of the system. We perform simulations at varying packing fractions $\eta = \pi(D^3/6 + D^2L/4)N/V$ in the isotropic and nematic phase. In Fig. 3.1, we present snapshots of the isotropic and nematic phase at packing fractions $\eta = 0.1723$ and 0.2338, respectively. The packing fractions of the coexisting isotropic and nematic phases are predicted to be $\eta_I = 0.1777$ and $\eta_N = 0.2058$, while the packing fraction of the nematic-smectic transition is at about $\eta_{Sm} \simeq 0.4438$. [18].

The simulations are started from an initial condition in which the orientations of the rods are randomly distributed in a cone with $0 \leqslant \theta \leqslant 0.15\pi$, where θ is the angle between the z-axis and the orientation of the rod. The deviations of the nematic director from the initial direction, which is along the z-axis, are often assumed to be small [55]. However, we find that during our simulations the director fluctuations have significant impact on the value of the order parameter and moreover on the best fitting distribution of the ODF. We therefore determine for each configuration the actual nematic director and we determine the ODF and the nematic order parameter with respect to the present director. In this way we ignore the fluctuations of the nematic director, which can be achieved experimentally by switching on a magnetic field that fixes the nematic director of the sample. The current nematic director and the nematic order parameter are determined from the standard 3×3 nematic order parameter tensor defined as [56]

$$Q_{\alpha\beta} = \frac{1}{N} \sum_{i=1}^{N} \frac{3u_{\alpha}^{i} u_{\beta}^{i} - \delta_{\alpha\beta}}{2} \tag{3.6}$$

where u_{α}^{i} is the α-component of the unit orientation vector of particle i, and $\delta_{\alpha\beta}$ is the Kronecker delta. The nematic order parameter is given by the largest eigenvalue of this tensor and the corresponding eigenvector is the nematic director of the sample.

We check for equilibration by monitoring the nematic order parameter of the system. The maximum allowed values for displacement and rotational moves are chosen such that the product of acceptance ratio and maximum displacement is maximum which corresponds with an acceptance ratio of about 25-30%. When equilibrium is reached, we perform a production run of 1.5×10^{6} sweeps (one displacement attempt per particle), while sampling is performed once every sweep. The quantities that are sampled are the nematic order parameter, the orientation distribution function $f(\theta)$, which is proportional to the probability to find a rod with an angle within $[\theta, \theta + d\theta]$ relative to the nematic director, and the scattered intensity $I(\vec{q})$ given by Eq. (3.3). It is convenient to write the reciprocal vector in cylindrical coordinates $\vec{q} = (q_r, q_z, q_\phi)$. If the system possesses uniaxial symmetry relatively to the nematic director lying along the z-axis, the scattered intensity depends only on r and z coordinates, and is independent of ϕ.

The Fourier transform of the (electron) density of a spherocylinder $\vartheta(\vec{q}; \hat{\omega})$ can be approximated by the Fourier transform of only the cylindrical part of length L and diameter D as the contribution from the caps is negligible for the given length-to-diameter ratio

$$\vartheta(\vec{q}; \hat{\omega}) \sim j_0 \left(\frac{L}{2} q_z \right) \frac{J_1 \left(\frac{D}{2} q_r \right)}{\frac{D}{2} q_r} \tag{3.7}$$

where $j_0(x)$ is the spherical Bessel function of the zeroth order, and $J_1(x)$ is the cylindrical Bessel function of the first order. Note that in Eq. (3.7) the polar axis of the coordinate system is defined along $\hat{\omega}$, which can easily be transformed to the coordinate system where the polar axis coincides with the direction of scattering vector $\vec{q}$. For infinitely thin rods, the Fourier transform is defined by $j_0(x)$ only and $J_1(x)/x$ allows for a finite diameter of the rods. The averaged square $\langle |\vartheta(\vec{q}; \hat{\omega})|^2 \rangle$ of this property is the formfactor $F(\vec{q})$ of the system that contains information about the shape, the inner structure of the molecule, and the ODF. The structure factor $S(\vec{q})$ of the system contains information about the positional and orientational correlations between the scattering particles. Equation (3.3) with (3.4) and (3.5), however, is not convenient for sampling the scattered intensity in simulations as it contains a double summation, and the difference $\vec{r}_i - \vec{r}_j$ in the exponent requires paying attention to the periodic boundary conditions. Using simple algebra the scattered intensity can be written as

$$I(\vec{q}) = \left(\sum_{i=1}^{N} \cos(\vec{q} \cdot \vec{r}_i) \vartheta(\vec{q}; \hat{\omega}_i) \right)^2 + \left(\sum_{i=1}^{N} \sin(\vec{q} \cdot \vec{r}_i) \vartheta(\vec{q}; \hat{\omega}_i) \right)^2 \tag{3.8}$$

which does not contain double summation and allows for twice the higher resolution as the smallest nonzero q_{min} is given by $q_{min} = 2\pi/L_i$ due to periodic boundary conditions compared to Eq. (3.3) where $q_{min} = 4\pi/L_i$ with L_i the dimension of the box in the i-th direction (due to the difference $\vec{r}_i - \vec{r}_j$ in Eq. (3.5)).

3.3 Results and discussion

As we wish to investigate whether correlations present in the interparticle scatter influences the determination of the ODF and S from scattered intensity, we first determine the "exact" value of S and the "exact" ODF of the rods directly in simulation. We perform simulations at varying packing fractions η in the isotropic and nematic phase. We measure S from Eq. (3.6), the ODF $f(\theta)$, and the scattered intensity $I(\vec{q})$. The latter two are both measured from simulations i) where the z-axis is taken to be the fixed nematic director, i.e., nematic director fluctuations are included and ii) where for each configuration the present nematic director is calculated such that nematic director fluctuations are disregarded. The latter can be achieved experimentally by applying a magnetic field that fixes the nematic director of the sample. We present results for the case that nematic director fluctuations are disregarded, unless stated differently. Table 3.1 shows S as a function of η for the statepoints we considered in this study. Note that the statepoint corresponding with a packing fraction $\eta \approx 0.185$ lies in the $I-N$ coexistence region. For this statepoint, we observe large fluctuations in the nematic order parameter during our simulations. Figs. 3.2 and 3.3 show typical examples of the "exact" orientational distribution function $f(\theta)$.

The measured ODF's are fitted with three different trial functions containing one fitting parameter α

$$f_1(\theta) = N_1(\alpha) \exp\left(\alpha \cos^2 \theta\right), \tag{3.9a}$$

$$f_2(\theta) = N_2(\alpha) \mathrm{e}^{-\frac{\theta^2}{2\alpha^2}}, \tag{3.9b}$$

$$f_3(\theta) = \frac{\alpha}{\sinh \alpha} \cosh\left(\alpha \cos \theta\right) \tag{3.9c}$$

where $N_i(\alpha)$ are the normalization constants, such that $\int_0^{\pi/2} d\theta \sin\theta f_i(\theta) = 1$. The first ODF is the Maier-Saupe distribution, the second is the Gaussian distribution introduced by Odijk, and the third one was proposed by Onsager [9]. The trial function introduced by Oldenbourg [57] is not considered here as the fitting parameter can be chosen such that it coincides with the Maier-Saupe distribution. We determine the nematic order parameter S from the three fitted ODF's using Eq. (3.1). The values of S are listed in Table 3.1 and plotted in Fig. 3.4. Figs. 3.2 and 3.3 and Table 3.1 show that at all densities the measured orientational distribution function is perfectly fitted by the Maier-Saupe distribution for all values of θ when nematic director fluctuations are ignored. The value of S calculated with the fitted Maier-Saupe distribution matches closely to the one measured as the largest value of the nematic order parameter tensor (3.6). The fits of the ODF's using the Onsager and Gaussian distributions are less peaked then the measured ones, which result in a slightly overestimated nematic order parameter. However the nematic order parameters obtained from the different distributions differ only by a few percent. Increasing the density, the fits of the ODF's using different trial functions and the resulting values for S approach each other.

We also study the influence of nematic director fluctuations on the ODF by comparing simulations where the z-axis is chosen to be the fixed nematic director with simulations where the nematic director is calculated for each configuration. As expected, we observe

η	0.1846	0.1969	0.2092	0.2215	0.2338
”Exact”	0.627	0.747	0.799	0.825	0.861
Maier-Saupe fit of ODF	0.631	0.754	0.805	0.824	0.866
Onsager fit of ODF	0.674	0.777	0.819	0.835	0.872
Gaussian fit of ODF	0.683	0.781	0.822	0.837	0.874
Maier-Saupe fit of $I(\psi)$	0.568	0.708	0.762	0.775	0.832
Gaussian fit of $I(\psi)$	0.596	0.732	0.779	0.790	0.840

Table 3.1: The nematic order parameter S of a fluid of hard spherocylinders for different packing fractions η determined directly in simulations (”exact”), determined from a fit of the ”exact” orientational distribution function, and determined from a fit of the scattering intensity $I(\psi)$.

nematic director fluctuations	no	yes
”Exact”	0.799	0.785
Maier-Saupe fit of ODF	0.805	0.769
Gaussian fit of ODF	0.822	0.793

Table 3.2: The nematic order parameter S of a fluid of hard spherocylinders with packing fraction $\eta = 0.2092$ determined directly in simulations with and without nematic director fluctuations.

that the ODF is slightly broader and gives lower values of S (see Table 3.2) when we use the z-axis as the nematic director and, thus, allow for nematic director fluctuations. These findings are a logical consequence of the method we used for taking into account director fluctuations, i.e., via a reference to the fixed z-axis. More surprisingly, we find that the ODF is best fitted by the Gaussian distribution, when we allow for nematic director fluctuations, while the one without nematic director fluctuations is best fitted by the Maier-Saupe distribution. The values of S are shown in Table 3.2. In the sequel, we calculate the actual nematic director for each configuration and ignore nematic director fluctuations.

We plot the scattered intensity $I(\vec{q})$ in Fig. 3.5. As the simulated rods do not have any inner structure we do not observe a diffusive ring at high values of scattering angle, and the scattered patterns resemble those obtained from interparticle scatter in experiments [8]. In experiments, the interparticle scatter is measured for $0 \leqslant |\vec{q}|D \leqslant 2\pi$. We therefore focus ourselves to this range in simulations. Moreover, for $|\vec{q}|D \gg 2\pi$, the statistical accuracy of $I(\vec{q})$ decreases significantly as $F(\vec{q}) \rightarrow 0$ and the computational cost in measuring $I(\vec{q})$ increases dramatically. Fig. 3.5a shows $I(\vec{q})$ for the isotropic phase at $\eta = 0.1723$. We clearly see that $I(\vec{q})$ is isotropic and does only depend on $|\vec{q}|$. Figs. 3.5b-3.5d show the scattered intensity for the nematic phase at varying η. We observe the typical anisotropic pattern of the scattering as also found experimentally for nematic solutions of the TMV and fd virus [8, 50].

In order to obtain information about the spatial order of the system, we investigate the scattered intensity $I(q_r, q_z)$ along the equators $q_z = 0$ and $q_r = 0$. We plot $I(q_r, 0)/N$, $F(q_r, 0)$, and $I(0, q_z)/N$ in Fig. 3.6 for a nematic phase at $\eta = 0.2092$ and $\eta = 0.2338$. The inset shows $S(q_r, 0)$ which is obtained by dividing the scattered intensity per particle by the formfactor (3.3). The intensity at $|\vec{q}| = 0$ is related to the isothermal compressibility χ_T, i.e. $I(0,0) = Nk_BT\chi_T/V$, where k_B is Boltzmann's constant, T the temperature, and $\chi_T = -1/V(\partial V/\partial P)$ with P the pressure. In the Gaussian approximation, the pressure of the nematic phase reads $P \simeq 3Nk_BT/V$, yielding $I(0,0) \simeq 1/3$. Fig. 3.6 shows indeed that $I(0,q_z) \simeq 1/3$ for $q_z \rightarrow 0$ and that $I(q_r,0) \simeq 1/3$ for $q_r \rightarrow 0$. However, it is difficult to obtain an accurate estimate of the intensity $I(0,q_z)$ for $q_z \rightarrow 0$ as the intensity is a rapidly varying function of q_z near the origin.

While the well-pronounced intensity peak as observed in x-ray diffraction experiments of suspensions of colloidal fd virus and TMV [8, 50] is missing in our $I(\vec{q})$, we do clearly observe a very broad peak in the structure factor, as found experimentally. The main reason for the absence of the intensity peak is that the virus particles used in the experiments carry a surface charge and are dressed with a cloud of co- and counterions, resulting in a much larger effective diameter D_{eff} of the particles compared to the actual (scattering) diameter D_{scat}. Although the effective length-to-diameter ratio L/D_{eff} of the fd or TMV virus is close to our value for the length-to-diameter ratio L/D of the simulated rods, the scattering length-to-diameter ratio L/D_{scat} is much larger than L/D_{eff}. If we use in our simulations of rods with $L/D = 15$, the formfactor of infinitely thin rods (which is of course much broader than the one shown in Fig. 3.6 for finite L/D), we obtain an intensity peak similar to the one found in experiments. The diameters D_{eff} and D_{scat} in the simulations can be varied such that it matches the experiments. However, varying the diameters does not change significantly the normalized arc intensity distribution, and we therefore decided to use the same diameters for D_{eff} and D_{scat}. The structure factor peak is at about $q_rD \sim 4$ corresponding with scattering from typical distances $2\pi/q_r \sim 1.57D$, which can be associated with the average rod separation in radial direction. We also observe that the structure factor peak moves to higher q_r at increasing η as expected. Compared to the strongly peaked structure factor peak in experiments of colloidal fd virus and TMV, we find a very broad structure factor peak in our simulations. Again, the discrepancy in the sharpness of the structure factor peak can be explained by the surface charge of the experimental rods, which increases the effective diameter of the rods considerable compared to the actual scattering diameter D_{scat} in experiments. Moreover, we expect that the flexibility of the fd virus particles broadens the structure factor peak compared to the rigid rods used in the simulations and counterbalances the effect of charge. It is worth noting that no structure factor peak was found by Van der Schoot et al. [58] using infinitely thin rods, i.e., $D = 0$ and ignoring the cylindrical Bessel function of the first order in Eq. (3.7). An explanation is still lacking and it is interesting to study this in more detail.

We also find parallel to the nematic director presmectic correlation peaks in the intensity $I(0,q_z)$ at about $q_zD \sim 0.4$ corresponding with scattering from a typical distance $2\pi/q_z \sim 16D$ which is associated with the length of the rods. The appearance of presmectic peaks are in agreement with theoretical predictions by Van der Schoot [59], who observed that the primary peak diverges at the spinodal instability to the smectic phase. It is worth noting that the presmectic peaks are already observed at packing fractions which are a factor of two smaller than the packing fraction at which the nematic-smectic phase transition occurs.

The scattered intensity in the direction of a vector $\vec{q}$ can be related to the orientational distribution function. At small absolute values of the scattering angle where the diffraction pattern depends on the structure factor one does not measure the single particle ODF but

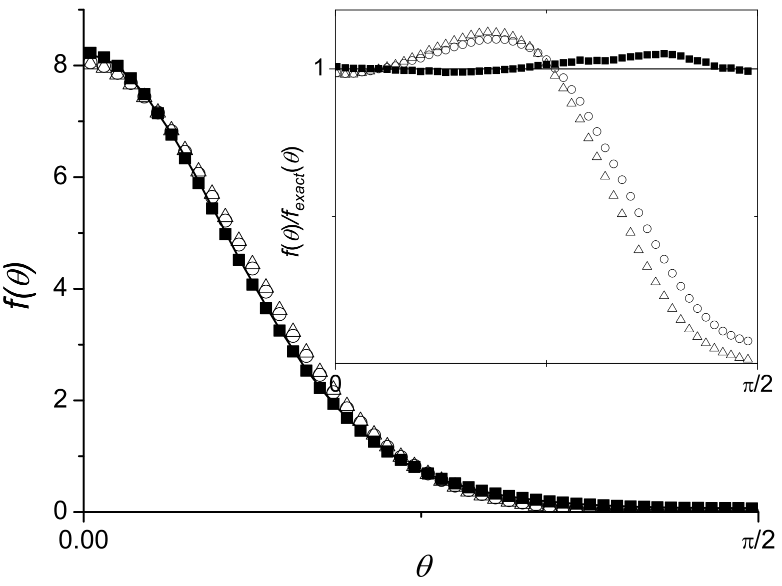

Figure 3.2: Orientational distribution functions $f(\theta)$ for packing fraction $\eta = 0.1846$. The solid line denotes the "exact" ODF measured directly in simulation. The "exact" ODF is fitted with the Maier-Saupe distribution (■), the Onsager distribution (○), and the Gaussian distribution (△). The inset shows the fits divided by the "exact" ODF.

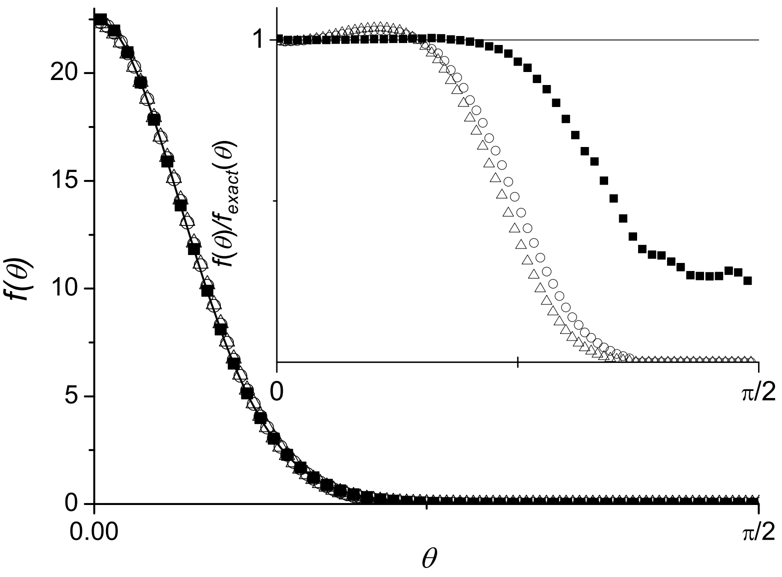

Figure 3.3: Orientational distribution functions $f(\theta)$ for packing fraction $\eta = 0.2338$. The solid line denotes the "exact" ODF measured directly in simulation. The "exact" ODF is fitted with the Maier-Saupe distribution (■), the Onsager distribution (○), and the Gaussian distribution (△). The inset shows the fits divided by the "exact" ODF.

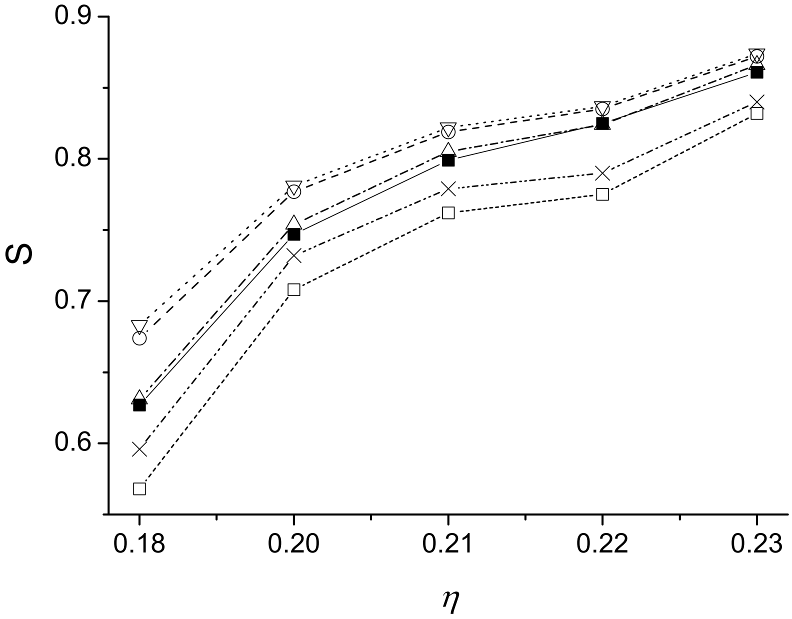

Figure 3.4: The nematic order parameter S as a function of the packing fraction η obtained from different routes: direct measurement of (3.6) –■–, using a Maier-Saupe fit of the ODF –△–, using a Gaussian distribution fit of the ODF –▽–, using an Onsager distribution fit of the ODF –○–, using an Onsager distribution fit of the scattered intensity –×–, using a Maier-Saupe fit of the scattered intensity –□–.

the coupled fluctuations of adjacent rods. This is expected to result in overestimation of the order parameter [7, 60]. At sufficiently high values of the scattering vector, it is often assumed that the structure factor approaches unity and the diffraction is determined by the form factor only. Note, however, that Fig. 3.6 shows that our structure factor does not approach unity for $q_r D < 2\pi$. Averaging over all possible orientations of the rods, we can approximate the scattering intensity to be

$$I(\vec{q}) \simeq F(\vec{q}) = \left\langle |\vartheta(\vec{q};\hat{\omega})|^2 \right\rangle = \int d\Omega\, f(\Omega) |\vartheta(q_r(\Omega), q_z(\Omega))|^2 \tag{3.10}$$

where Ω is the solid angle (θ, φ) of a rod with respect to the nematic director (θ) and azimuthally with respect to the incident beam (φ). Due to the axial symmetry relatively to nematic director $f(\Omega)$ simplifies to $f(\theta)$. Using the explicit form of the Fourier transform (3.7) this expression can be easily related to the intensity distribution along the equatorial arc of diffraction pattern

$$I(q,\psi) = \int_0^{2\pi} d\varphi \int_0^{\pi/2} d\theta \sin\theta f(\theta) \left[j_0\left(\frac{L}{2} q \cos\alpha\right) \frac{J_1\left(\frac{D}{2} q \sin\alpha\right)}{\frac{D}{2} q \sin\alpha} \right]^2 \tag{3.11}$$

where q is the absolute value of the scattering vector $\vec{q}$ along the arc, ψ is the angle with the q_r-axis as denoted in Fig. 3.5, and α is defined by $\cos\alpha = \sin\psi\cos\theta + \cos\psi\sin\theta\cos\varphi$. This formula is difficult to use in the analysis of experimental data, and instead the ex-

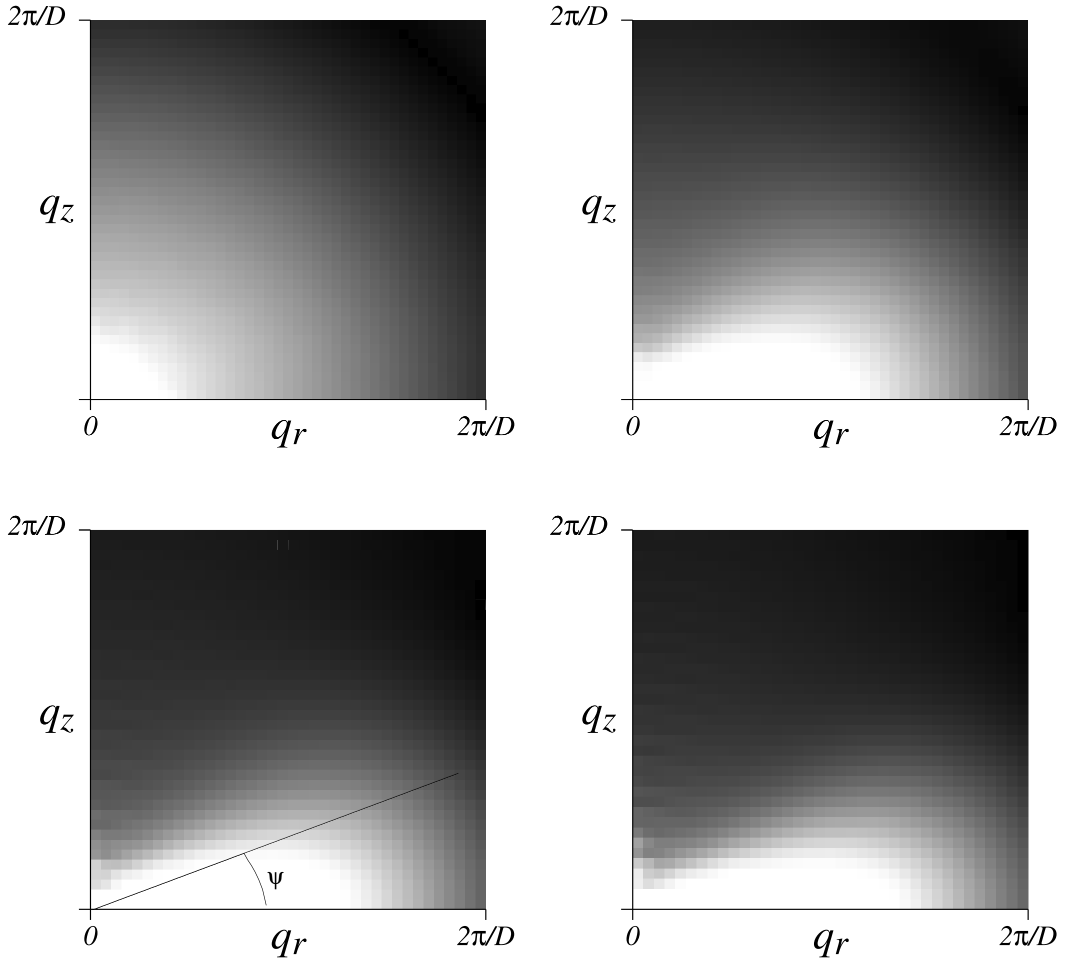

Figure 3.5: Density plots of the scattered intensity $I(q_r, q_z)$ for varying packing fractions: a) $\eta = 0.1723$ (isotropic), b) $\eta = 0.1846$, c) $\eta = 0.2092$, d) $\eta = 0.2338$. Bright areas correspond to high and dark areas correspond to low scattered intensity.

pression relating $I(\psi)$ to $f(\theta)$ proposed by Leadbetter is commonly used [7, 53]

$$I(\psi) = \int_{\psi}^{\pi/2} d\theta \frac{f(\theta)\sin\theta}{\cos^2\psi\sqrt{\tan^2\theta - \tan^2\psi}}. \tag{3.12}$$

It does not depend on the absolute value of the scattering vector and is based on several drastic assumptions which are discussed in [53, 60]. Leadbetter proposed it for the intensity distribution along the "wide angle ring" corresponding to the lateral mean distance between neighboring molecules. An analytical inversion of this formula (3.12) was proposed by Deutsch [52] and reads

$$f(\theta) = -\frac{1}{N\sin\theta}\frac{d}{d\theta}\int_{\theta}^{\pi/2} d\psi I(\psi)\frac{\tan\psi}{\sqrt{\tan^2\psi - \tan^2\theta}}. \tag{3.13}$$

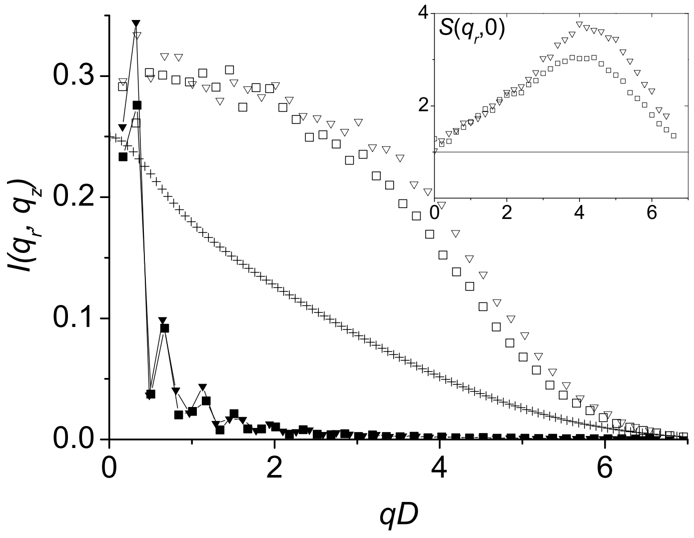

Figure 3.6: Intensity distribution per particle along the $q_r = 0$ and $q_z = 0$ directions: □ $I(q_r, 0)$, −■− $I(0, q_z)$ for $\eta = 0.2092$, ▽ $I(q_r, 0)$, −▼− $I(0, q_z)$ for $\eta = 0.2338$, together with the formfactor $F(q_r, 0)$ (+), which is not significantly distinct for these two packing fractions. The inset shows the structure factor $S(q_r, 0)$ for the two packing fractions

with normalization constant $N = \int_0^{\pi/2} f(\theta)\sin\theta d\theta$. This allows calculating the exact form of ODF from X-ray diffraction data. However, using scattering data that includes experimental and statistical errors, a numerical inversion of the integral equation is very inaccurate. Hence, one often employs a trial function for the ODF with some fitting parameters. If one uses the Maier-Saupe distribution function $f(\theta) = N(\alpha)\exp(\alpha\cos^2\theta)$, the scattered intensity is described by [61, 62]

$$I(\psi) = N_1(\alpha)\frac{\exp(\alpha\cos^2\psi)}{\sqrt{\alpha}\cos\psi}\frac{\sqrt{\pi}}{2}\mathrm{erf}(\sqrt{\alpha}\cos\psi) \tag{3.14}$$

with fitting parameter α. If we use the Onsager distribution function $f(\theta) = \alpha\cosh(\alpha\cos\theta)/\sinh\alpha$, the integration of (3.12) yields [63]

$$I(\psi) = \frac{\alpha}{\sinh\alpha}[1 + \frac{\pi}{2}L_1(\alpha\cos\psi)] \tag{3.15}$$

where $L_1(x)$ is the modified Struve function of the first order. Unfortunately, the Gaussian form for the ODF does not lead to a simple expression for the intensity distribution.

Comparison of different distribution functions is straightforward due to simple normalization rules. The Leadbetter expression provides similar normalization for scattered intensity; provided that an orientational distribution function is properly normalized we can integrate the intensity along the arc to obtain $\int_0^{\pi/2} d\varphi I(\varphi) = \pi/2$ which is independent of the particular form of the trial ODF.

We determine the ODF from the intensity distribution along the equatorial arc of the x-ray diffraction patterns for different absolute values of the scattering vector to check

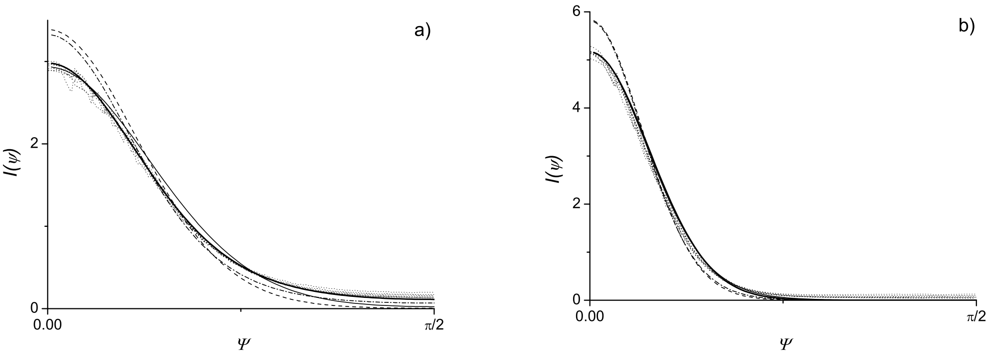

Figure 3.7: Equatorial intensity distributions $I(\psi, |\vec{q}|)$ for packing fractions $\eta = 0.1846$, $\eta = 0.2329$, dots represent the intensities measured along several arcs with absolute value of scattering vector between $1.2\pi < |q|\,D < 2\pi$, solid lines are fits of these intensities with distributions (3.14) (thick line) and (3.15) (thin line), dashed and dashed-dotted lines are the intensities obtained from the formula proposed by Leadbetter formula using the fits of the "exact" orientational distribution function with the Onsager and Maier-Saupe distributions, respectively.

how strong it depends on $|\vec{q}|$. This can serve as a test of the applicability of the formula proposed by Leadbetter Eq. (3.12) which is independent on $|\vec{q}|$. In Fig. 3.7, we plot equatorial intensity distributions for packing fractions $\eta = 0.1846$ and $\eta = 0.2338$ with $3.7 < |\vec{q}|\,D < 6.3$. We do not observe strong dependence on $|\vec{q}|$, which agrees with the assumption used in the formula proposed by Leadbetter. However, Fig. 3.6 shows that the structure factor only tends to approach unity at the highest value of q_r, i.e., $q_r D = 2\pi$ and, the approximation $I(\vec{q}) \simeq F(\vec{q})$ is not valid.

We, however, do fit our measured intensities with the intensity distributions using the Maier-Saupe distribution (3.14) and the Onsager distribution (3.15) and the corresponding ODF's are compared with the ones measured directly in simulation in Figs. 3.8 and 3.9. Figs. 3.8 and 3.9 show clearly that the ODF obtained from scattered intensity are less peaked than the "exact' ones. Using the ODF's from scattered intensity, we determine the nematic order parameter using (3.1). The values of the nematic order parameter obtained from scattered intensity underestimate the "exact" S by $2 - 9\%$. Although the "exact" ODF is best fitted by the Maier-Saupe distribution, the Onsager distribution gives a better estimate of the nematic order parameter calculated from scattered intensity as shown in Figs. 3.8 and 3.9. On the other hand, the result of the Leadbetter formula supplied with the fits using the Onsager and Maier-Saupe distribution of the "exact" ODF is compared to the measured intensities in Fig. 3.7. Fig. 3.7 shows, that the intensity distributions obtained from the fits of the "exact" ODF is more peaked than the measured intensity distributions.

3.4 Conclusions

The orientational distribution function, the nematic order parameter, and the scattered intensity are calculated in simulations for a system of hard spherocylinders with an aspect ratio of 15 for varying densities in the isotropic and nematic phase. The angular distribution function in the nematic phase is well described by the Maier-Saupe distribution when nematic director fluctuations are ignored. Including nematic director fluctuations, the ODF is best fitted by the Gaussian distribution. The Leadbetter approach is found to give a reasonable description of the x-ray scattering pattern, even when $S(\vec{q}) \neq 1$ and thus spatial and orientational correlations are present. The values of the nematic order parameter S and the ODF's obtained from interparticle scattering were compared with the "exact" ones determined directly in simulation in order to study the effect of correlations between the rods. We find that the values for S determined from interparticle scattering are smaller than the "exact" ones by about 2-9 $\%$ and that the ODF's are broader than the "real" ones. We also find that the values for S and the ODF are rather insensitive to the absolute value of the scattering vector which agrees well with the assumption proposed by Leadbetter that $I(q, \psi)$ along the equatorial arc does not dependent on $|\vec{q}|$.

The length-to-diameter ratio of the rods used in simulation are much smaller than those used in experiments on colloidal fd virus and TMV. However, the effective anisotropy, can be tuned by the salt concentration such that it approaches the value used in simulation. It is interesting to investigate in more detail what the effect of anisotropy is on the scattered intensity. As already explained above, one expects that the structure factor peak becomes more pronounced along the q_r-direction upon increasing the aspect ratio of the rods. When the structure factor peak is sharper, one expects that $S(\vec{q})$ approaches 1 more rapidly and that the influence of the structure factor and correlations become less important in the determination of the nematic order parameter and the ODF from scattered intensity. One might also argue that a more pronounced structure factor peak as expected at higher aspect ratios of the rods may yield a peak in the scattered intensity as observed experimentally [8, 50], but which was never predicted theoretically [58]. This will be investigated in future work.

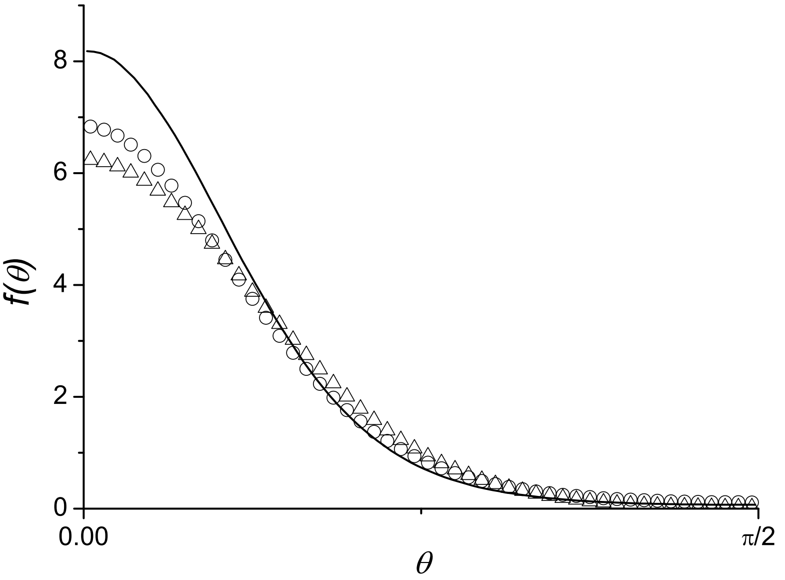

Figure 3.8: Orientational distribution functions $f(\theta)$ for packing fraction $\eta = 0.1846$. The solid line denotes the "exact" ODF measured directly in simulation. The scattered intensity is fitted with the Maier-Saupe distribution (○) and the Onsager distribution (△).

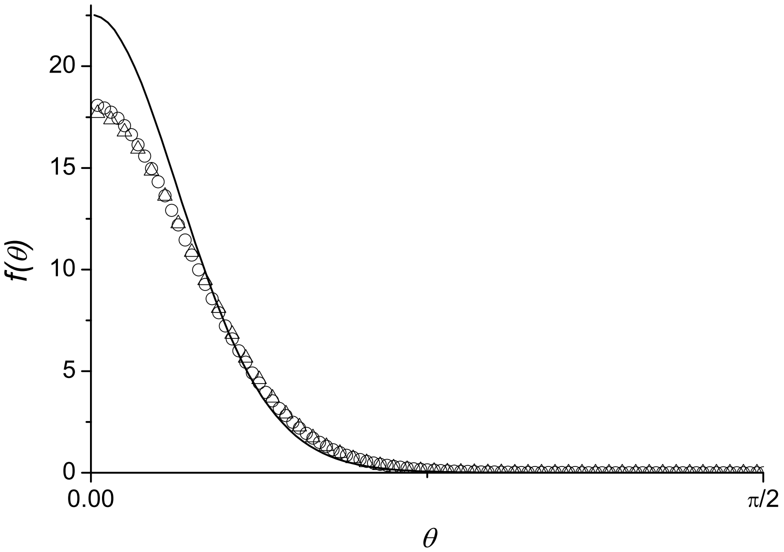

Figure 3.9: Orientational distribution functions $f(\theta)$ for packing fraction $\eta = 0.2338$. The solid line denotes the "exact" ODF measured directly in simulation. The scattered intensity is fitted with the Maier-Saupe distribution (○) and the Onsager distribution (△).

Acknowledgments

We thank Seth Fraden for stimulating discussions and we like to thank the Dutch National Computer Facilities foundation for access to the SGI Origin3800. The High Performance Computing group of Utrecht University is gratefully acknowledged for ample computer time.

3.A Formfactor of a spherocylinder

3.A.1 contribution of a cylinder

The form factor of a spherocylinder is constructed from contributions of the cylinder part, and of the spherical caps. First, let us consider the cylinder formfactor, which is basically the Fourier transform of a density, considered constant inside the volume of a cylinder and zero otherwise. To accomplish the integration over the volume of a cylinder it is convenient to change to new coordinates, which are defined as follows

$$\vec{r} = \begin{pmatrix} x \\ y \\ z \end{pmatrix} \rightarrow \begin{pmatrix} \frac{D}{2} p \cos\phi \\ \frac{D}{2} p \sin\phi \\ \frac{L}{2} t \end{pmatrix}. \tag{3.A.1}$$

It is basically cylindrical coordinates rescaled such that a cylinder of length L and diameter D is described by the parameters $-1 \leqslant t \leqslant 1$, $0 \leqslant p \leqslant 1$, and $0 \leqslant \phi \leqslant 2\pi$. Recalling the corresponding Jacobian the volume differential can be written as

$$d\vec{r} = \frac{LD^2}{8} dtdppd\phi. \tag{3.A.2}$$

The integral over the volume of cylinder can be calculated as follows

$$\begin{aligned}\int\limits_{V_{cyl}} d\vec{r}e^{i\vec{q}\vec{r}} &= \frac{LD^2}{8}\int\limits_{-1}^{1}dt\int\limits_{0}^{2\pi}d\phi\int\limits_{0}^{1}dpp\exp\left[i\left(\frac{D}{2}q_xp\cos\phi+\frac{D}{2}q_yp\sin\phi+\frac{L}{2}q_zt\right)\right]\\ &= \frac{LD^2}{8}2j_0\left(\frac{L}{2}q_z\right)\int\limits_{0}^{2\pi}d\phi\int\limits_{0}^{1}dpp\exp\left[i\frac{D}{2}p\sqrt{q_x^2+q_y^2}(\cos\psi\cos\phi+\sin\psi\sin\phi)\right]\\ &= \frac{LD^2}{8}2j_0\left(\frac{L}{2}q_z\right)2\pi\int\limits_{0}^{1}dppJ_0\left(\frac{D}{2}pq_r\right) = \frac{LD^2}{8}2j_0\left(\frac{L}{2}q_z\right)2\pi\frac{J_1\left(\frac{D}{2}q_r\right)}{\frac{D}{2}q_r}\\ &= 2V_{cyl}j_0\left(\frac{L}{2}q_z\right)\frac{J_1\left(\frac{D}{2}q_r\right)}{\frac{D}{2}q_r},\end{aligned} \tag{3.A.3}$$

where $j_0(x)$ is the zero order spherical Bessel function, $J_1(x)$ is the first order cylindrical Bessel function and where V_{cyl} is the volume of a cylinder, and $q_r = \sqrt{q_x^2+q_y^2}$.

3.A.2 contribution of the caps

Similarly, for the contribution of the semi-spherical caps

$$\vec{r} = \pm\begin{pmatrix}0\\0\\\frac{L}{2}\end{pmatrix} \pm \frac{D}{2}t\begin{pmatrix}\sin\theta\cos\phi\\\sin\theta\sin\phi\\\cos\theta\end{pmatrix}, \quad d\vec{r} = \frac{D^3}{8}t^2\cos\theta dtd\theta d\phi. \tag{3.A.4}$$

The caps are described by $0 \leqslant t \leqslant 1$, $0 \leqslant \theta \leqslant \pi$, and $0 \leqslant \phi \leqslant 2\pi$. The Fourier transform reads

$$\begin{aligned}\int\limits_{V_{caps}} d\vec{r}e^{i\vec{q}\vec{r}} =&\frac{D^3}{8}\int\limits_{0}^{1}dt\,t^2\int\limits_{0}^{\pi/2}d\theta\sin\theta\int\limits_{0}^{2\pi}d\phi\,e^{i\frac{D}{2}(q_z\cos\theta+q_x\sin\theta\cos\phi+q_y\sin\theta\sin\phi)t}e^{iq_z\frac{L}{2}}+\\ &\frac{D^3}{8}\int\limits_{0}^{1}dt\,t^2\int\limits_{\pi/2}^{\pi}d\theta\sin\theta\int\limits_{0}^{2\pi}d\phi\,e^{i\frac{D}{2}(q_z\cos\theta+q_x\sin\theta\cos\phi+q_y\sin\theta\sin\phi)t}e^{-iq_z\frac{L}{2}}\\ =&\frac{D^3}{8}e^{iq_z\frac{L}{2}}\int\limits_{0}^{1}dt\,t^2\int\limits_{0}^{1}d\cos\theta\int\limits_{0}^{2\pi}d\phi\,e^{i\frac{D}{2}(q_z\cos\theta+q_r\sin\theta\cos\phi)t}+\\ &\frac{D^3}{8}e^{-iq_z\frac{L}{2}}\int\limits_{0}^{1}dt\,t^2\int\limits_{-1}^{0}d\cos\theta\int\limits_{0}^{2\pi}d\phi\,e^{i\frac{D}{2}(q_z\cos\theta+q_r\sin\theta\cos\phi)t}\\ =&\frac{D^3}{8}2\pi e^{iq_z\frac{L}{2}}\int\limits_{0}^{1}dt\,t^2\int\limits_{0}^{1}d\cos\theta\,e^{iq_z\frac{D}{2}t\cos\theta}J_0(q_r\frac{D}{2}t\sin\theta)+\\ &\frac{D^3}{8}2\pi e^{-iq_z\frac{L}{2}}\int\limits_{0}^{1}dt\,t^2\int\limits_{-1}^{0}d\cos\theta\,e^{iq_z\frac{D}{2}t\cos\theta}J_0(q_r\frac{D}{2}t\sin\theta).\end{aligned} \tag{3.A.5}$$

As long as the Fourier transform of the point-symmetric object is real, it is convenient to separate the real and the imaginary parts of the integral over the volume of the caps

$$\begin{aligned}\int_{V_{caps}} d\vec{r}e^{i\vec{q}\vec{r}} =& 2\pi\frac{D^3}{8}2\cos\left(q_z\frac{L}{2}\right)\int_0^1 dt\, t^2\int_0^1 d\cos\theta\cos\left(q_z\frac{D}{2}t\cos\theta\right)J_0\left(q_r\frac{D}{2}t\sin\theta\right)+\\ & i2\pi\frac{D^3}{8}2\sin\left(q_z\frac{L}{2}\right)\int_0^1 dt\, t^2\int_0^1 d\cos\theta\sin\left(q_z\frac{D}{2}t\cos\theta\right)J_0\left(q_r\frac{D}{2}t\sin\theta\right).\end{aligned} \tag{3.A.6}$$

Indeed, the angular integral in the imaginary part of this expression is recognized as the Gegenbauer sine-integral [64] and equals zero, while the integration of the real part yields [65]

$$\begin{aligned}\int_{V_{caps}} d\vec{r}e^{i\vec{q}\vec{r}} =& \frac{\pi D^3}{2}\cos\left(q_z\frac{L}{2}\right)\int_0^1 dt\, t^2\int_0^1 dx\,\frac{x}{\sqrt{1-x^2}}\cos\left(q_z\frac{D}{2}t\sqrt{1-x^2}\right)J_0\left(q_r\frac{D}{2}tx\right)\\ =& \frac{\pi D^3}{2}\cos\left(q_z\frac{L}{2}\right)\int_0^1 dt\, t^2 j_0\left(\frac{D}{2}t\sqrt{q_z^2+q_r^2}\right)\\ =& \frac{\pi D^3}{2}\cos\left(q_z\frac{L}{2}\right)\frac{j_1\left(\frac{D}{2}q\right)}{\frac{D}{2}q},\end{aligned} \tag{3.A.7}$$

where $j_1(x)$ is the spherical Bessel function of the first order and $q=\sqrt{q_z^2+q_r^2}$. For the length-to-diameter ratio $L/D = 15$ used in the chapter, the contribution of the caps is negligible and we set these to zero in our calculations of the diffraction patterns.

3.B Intensity distributions based on trial functions

The equation (3.12) proposed by Leadbetter for the intensity distribution $I(\psi)$ can be integrated for several trial functions. Here we give the expressions obtained by employing the Maier-Saupe and the Onsager distribution functions. We were not able to find an analytic expression using the Gaussian distribution function. Employing the Maier-Saupe distribution function $f(\theta) = N(\alpha)\exp(\alpha\cos^2\theta)$ yields

$$\begin{aligned}I(\psi) =& \int_{\psi}^{\frac{\pi}{2}} d\theta\frac{e^{\alpha\cos^2\theta}\sin\theta}{\cos^2\psi\sqrt{\tan^2\theta-\tan^2\psi}} = \frac{1}{\cos\psi}\int_0^{\cos\psi} d\cos\theta\,\cos\theta\frac{e^{\alpha\cos^2\theta}}{\sqrt{\cos^2\psi-cos^2\theta}} =\\ & \frac{1}{\sqrt{\alpha}\cos\psi}\int_0^{\sqrt{\alpha}\cos\psi} dx\, x\frac{e^{x^2}}{\sqrt{\alpha\cos^2\psi-x^2}} = \frac{e^{\alpha\cos^2\psi}}{\sqrt{\alpha}\cos\psi}\int_0^{\sqrt{\alpha}\cos\psi} d\sqrt{\alpha\cos^2\psi-x^2}e^{\alpha\cos^2\psi-x^2}\\ & = \frac{e^{\alpha\cos^2\psi}}{\alpha\cos^2\psi}\frac{\sqrt{\pi}}{2}\mathrm{erf}(\sqrt{\alpha}\cos\psi).\end{aligned} \tag{3.B.8}$$

And for the Onsager distribution function $f(\theta) = \alpha \cosh(\alpha \cos\theta)/\sinh\alpha$:

$$I(\psi) = \int_{\psi}^{\frac{\pi}{2}} d\theta\, \sin\theta \frac{\cosh(\alpha\cos\theta)}{\cos^2\theta\sqrt{\tan^2\theta - \tan^2\psi}} = \frac{1}{\cos\psi} \int_{0}^{\cos\psi} d\cos\theta\, \frac{\cosh(\alpha\cos\theta)\cos\theta}{\sqrt{\cos^2\psi - \cos^2\theta}} =$$

$$\int_0^1 dx\, x \frac{\cosh(\alpha x\cos\psi)}{\sqrt{1-x^2}} = -\sqrt{1-x^2}\cosh(\alpha x\cos\psi)\Big|_0^1 + \alpha\cos\psi \int_0^1 dx\, \sqrt{1-x^2}\,\sinh(\alpha x\cos\psi)$$

$$= 1 + \frac{\pi}{2} L_1(\alpha\cos\psi). \quad (3.B.9)$$

Here $L_1(x)$ is the modified Struve function of the first order.

4

Asymptotic decay of the pair correlation function in molecular fluids: application to hard rods

We investigate the asymptotic decay of the total correlation function $h(1,2)$ in molecular fluids. To this end, we expand the angular dependence of $h(1,2)$ and the direct correlation function $c(1,2)$ in the Ornstein-Zernike equation in a complete set of rotational invariants. We show that all the harmonic expansion coefficients $h_{l_1 l_2 l}(r)$ are governed by a common exponential decay length and a common wavelength of oscillations in the isotropic phase. We determine the asymptotic decay of the total correlation functions by investigating the pole structure of the reciprocal ($\mathbf{q}$-space) harmonic expansion coefficients $h_{l_1 l_2 l}(q)$. The expansion coefficients in laboratory frame of reference $h_{l_1 l_2 l}(r)$ are calculated in computer simulations for an isotropic fluid of hard spherocylinders. We find that the asymptotic decay of $h(1,2)$ is exponentially damped oscillatory for hard spherocylinders with a length-to-diameter ratio $L/D \leqslant 10$ for all statepoints in the isotropic fluid phase. We compare our results on the pole structure using different theoretical Ansätze for $c(1,2)$ for hard ellipsoids. The theoretical results show that the asymptotic decay of $h(1,2)$ is exponentially damped oscillatory for all elongations of the ellipsoids.

4.1 Introduction

The asymptotic analysis of pair correlation functions dates back to the work of Kirkwood [66], who showed that the total correlation function $h(r)$ of a fluid with interatomic potentials decaying faster then a power law, can be presented as a sum of exponential contributions $rh(r) = \sum_n \mathcal{A}_n e^{-\alpha_{0,n} r} \cos(\alpha_{1,n} r + \theta_n)$ with $\mathcal{A}_n$ and θ_n the amplitude and phase, respectively. Consequently, the asymptotics, i.e., the ultimate or leading decay of $h(r)$ is determined by the pole or poles closest to the real axis (smallest $\alpha_{0,n}$).

The asymptotic behavior of the pair correlation function plays a significant role in the understanding of interfacial phenomena in fluids, e.g., it has an impact on the wetting transition at wall-fluid interfaces [67, 68] as well as on the structure of interfaces between coexisting phases [67, 69, 70]. For high temperatures and densities the asymptotic behavior is determined by repulsive forces, while at low densities and temperatures attractive forces are more important and correlations exhibit monotonic decay. Considering a one-dimensional model, Fisher and Widom showed that there exists a line in the temperature-density plane where the asymptotic decay of the pair correlation function crosses over from monotonic to exponentially damped oscillatory behavior [71]. The authors also conjectured that a similar transition should occur in three-dimensional systems provided that the potential is short-ranged. The Fisher-Widom line was calculated for three-dimensional model fluids, e.g., the square-well fluid [68], Lennard-Jones fluid [72, 73], (screened) Coulombic fluids [74, 75], hard-core attractive Yukawa fluids [76] and general binary mixtures [77], screened-Coulomb charged hard sphere binary fluids [78], binary Gaussian core mixtures [79], colloid-polymer mixtures [80], binary star-polymer solutions [81], and binary hard-sphere mixtures [82]. The asymptotic decay of the radial distribution function $\mathrm{g}(r)$ is determined by investigating the pole structure of the structure factor $S(q)$ [68, 77]. Moreover, the asymptotic decay was also studied recently in computer simulations [83]. Here, the longest range decay of the total correlation function $h(r) = \mathrm{g}(r) - 1$ was determined by calculating the direct correlation function $c(r)$ from the simulated $h(r)$ using the Ornstein-Zernike equation, in this way the truncated Lennard-Jones and a hard sphere fluid were studied. In conclusion, the asymptotic decay of pair correlations in simple fluids is well-studied by now. This should be contrasted to molecular fluids, which show the existence of orientational degrees of freedom that interplay in a nontrivial way with the translational degrees of freedom. To the best of our knowledge, we are not aware of any study on the asymptotic decay of the total correlation function $h(1, 2)$ in fluids interacting with anisotropic pair potentials.

In this chapter, we give a brief summary of the asymptotics of the pair correlation function of a fluid with short-ranged spherically symmetric pair potentials and we give a generalization for fluids interacting with anisotropic interaction potentials. Expanding the Ornstein-Zernike (OZ) equation in a complete set of rotational invariants, we show that in the isotropic phase the asymptotic decay of all $\mathbf{r}$-frame harmonic expansion coefficients $h_{l_1 l_2 l}(r)$ is governed by a common exponential decay length and a common wavelength of oscillations. The asymptotic decay is determined by the pole with the slowest exponential decay of the $\mathbf{q}$-space harmonic expansion coefficient $h_{l_1 l_2 l}(q)$, which is related through a Hankel transform to the $\mathbf{r}$-space harmonic expansion coefficient $h_{l_1 l_2 l}(r)$. Analogous to our previous study of the Lennard-Jones fluid [83], we measure the space-fixed harmonic expansion coefficients of the total correlation function $h_{l_1 l_2 l}(r)$, extract the expansion coefficients of the direct correlation function $c_{l_1 l_2 l}(r)$ using the harmonic expansion of the

OZ equation, and determine the asymptotic behavior from the latter. We compare our results for $c(1,2)$ with some theoretical Ansätze for $c(1,2)$.

This chapter is organized as follows: in Sec. 4.2, we briefly discuss the asymptotics of the pair correlation function of a simple fluid with spherically symmetric pair potentials, and we give a generalization for fluids interacting with anisotropic pair potentials. In Sec. 4.3, we present details on the simulations, from which we obtain the direct correlation function. The results of $c(1,2)$ are compared with several theoretical Ansätze. Finally, the results are discussed in Sec. 4.4.

4.2 Theory

4.2.1 Simple fluids

Below, we give a brief outline of the asymptotic decay of the pair correlation function of a fluid with short-ranged, spherically symmetric interaction potentials. For more details, we refer the reader to Refs. [68, 77]. The asymptotics of the total pair correlation function $h(r) = \mathrm{g}(r) - 1$ is most easily determined by investigating the pole structure of the structure factor $S(q)$.

In an isotropic homogeneous bulk fluid, all correlation functions depend on the absolute distance and the Ornstein-Zernike (OZ) equation reads

$$h(r) = c(r) + \rho \int d\mathbf{r}' c(|\mathbf{r} - \mathbf{r}'|) h(r'), \tag{4.1}$$

where ρ is the bulk density. The OZ equation relates the total pair correlation function $h(r)$ to the direct correlation function $c(r)$. The three-dimensional Fourier transform $\hat{f}(q)$ of a spherically symmetric function $f(r)$ reads

$$\begin{aligned} \hat{f}(q) &= 4\pi \int\limits_0^\infty dr\, r^2 f(r) \frac{\sin qr}{qr}, \\ f(r) &= \frac{1}{2\pi^2} \int\limits_0^\infty dq\, q^2 \hat{f}(q) \frac{\sin qr}{qr}, \end{aligned} \tag{4.2}$$

and the OZ equation (4.1) in Fourier representation reads

$$\hat{h}(q) = \frac{\hat{c}(q)}{1 - \rho \hat{c}(q)}, \tag{4.3}$$

where the convolution theorem is used. Applying the inverse Fourier transform, one obtains

$$rh(r) = \frac{1}{4\pi^2 i} \int\limits_{-\infty}^{\infty} dq q e^{iqr} \frac{\hat{c}(q)}{1 - \rho \hat{c}(q)}. \tag{4.4}$$

For short-ranged or exponentially decaying pair potentials, where $c(r)$ decays faster than a power law, the asymptotic behavior of $rh(r)$ is determined by the poles of $\hat{h}(q)$, i.e., complex values of the wave number $q = \alpha_1 + i\alpha_0$ that satisfy

$$1 - \rho \hat{c}(q) = 0. \tag{4.5}$$

Here $\alpha_0, \alpha_1 \in \mathbb{R}$. Eq. (4.4) can be evaluated by performing the contour integration on an infinite semicircle in the upper half-plane, and provided all poles are simple, one obtains

$$rh(r) = \sum_n R_n e^{iq_n r}, \tag{4.6}$$

where q_n is the n-th pole and $2\pi R_n$ is the corresponding residue of $q\hat{c}(q)/(1-\rho\hat{c}(q))$ at $q = q_n$. The poles can be found by equating the real and imaginary part in Eq. (4.5), yielding the following set of equations for α_1 and α_0

$$\begin{cases} 1 = 4\pi\rho \int\limits_0^\infty dr\, r^2\, c(r) \dfrac{\sinh(\alpha_0 r)}{\alpha_0 r} \cos(\alpha_1 r) \\ 1 = 4\pi\rho \int\limits_0^\infty dr\, r^2\, c(r) \cosh(\alpha_0 r) \dfrac{\sin(\alpha_1 r)}{\alpha_1 r}. \end{cases} \tag{4.7}$$

Provided $c(r)$ is known for a given statepoint, this set of equations can be used to find the poles. In general, an infinite number of poles can be expected. However, the pole or poles with the smallest imaginary part of q_n has the slowest exponential decay, and dominates the asymptotic behavior or longest range part of $h(r)$. Two scenarios are possible: (a) Pure exponential decay dominates at longest range, if a pole lying on the imaginary axis, i.e., $q = i\alpha_0$, has the smallest value of α_0. The pure imaginary pole can be obtained from the first equation of (4.7) with $\alpha_1 = 0$. Using Eq. (4.6), we find that the contribution of a pure imaginary pole to $rh(r)$ is $rh(r) \sim \mathcal{A}\exp(-\alpha_0 r)$ with $2\pi\mathcal{A}$ the corresponding residue. (b) Exponentially damped oscillatory decay with a wavelength $2\pi/\alpha_1$ dominates at longest range, if a conjugate pair of poles $q = \pm\alpha_1 + i\alpha_0$ has a smaller imaginary part than the pure imaginary pole. The decay of $rh(r)$ at longest range is then determined by the contribution of the conjugate pair of complex poles: $rh(r) \sim 2|\mathcal{A}|\exp(-\alpha_0 r)\cos(\alpha_1 r - \theta)$. Explicit formulas for the amplitude $|\mathcal{A}|$ and phase θ are given elsewhere [75, 77].

For potentials, which are purely repulsive and of finite range, $c(r)$ can be considered negative for all r and thus no solution can be found for a pure imaginary pole, the fast decaying positive tail of $c(r)$, which appear in some theories and also simulations, do not seem to play significant role for asymptotic decay. Consequently, one expects exponentially damped oscillatory decay for fluids interacting with purely repulsive short-ranged potentials.

4.2.2 Molecular Fluids

In molecular liquids, the interaction potential and, hence, the correlation functions, depend no longer only on the absolute center-of-mass distance of the two particles, but also on their orientations. We stress that this even holds in the isotropic phase. Consequently, the structure in molecular fluids is described by the total correlation function $h(\mathbf{r}_1, \mathbf{u}_1, \mathbf{r}_2, \mathbf{u}_2) \equiv h(1,2)$, where $\mathbf{r}_1$ and $\mathbf{r}_2$ are the center of mass coordinates of particle 1 and 2, and $\mathbf{u}_1$ and $\mathbf{u}_2$ denote the unit vectors defining the orientations of the molecules. The interaction potential in molecular systems is usually very complicated, i.e., Lennard-Jones potentials for each individual atom in a molecule and, thus, the orientational degrees of freedom mixes in a nontrivial way with the translational degrees of freedom. In this chapter, we limit ourselves to uniaxially symmetric particles, which are invariant under inversion of their principle axis. A simple model to study the interplay of translational and rotational degrees of freedom is a fluid consisting of hard spherocylinders or hard ellipsoids of revolution. These systems serve as simple models for molecular fluids and lyotropic liquid crystals.

It is convenient to expand the total correlation function in a complete set of angular functions with expansion coefficients depending on the separation $r = |\mathbf{r}_{12}|$ with $\mathbf{r}_{12} \equiv \mathbf{r}_1 - \mathbf{r}_2$ [13]. There are two common choices for this expansion. In one expansion, the molecular orientations are referred to an intermolecular reference frame in which the polar axis is along the intermolecular vector $\mathbf{r}_{12}$. In the other expansion, the molecular orientations are defined in a space-fixed or laboratory frame of reference. Here, we employ the latter expansion:

$$f(\mathbf{r}, \mathbf{u}_1, \mathbf{u}_2) = \sum_{l_1 l_2 l} f_{l_1 l_2 l}(r) \Phi_{l_1 l_2 l}(\mathbf{u}_1, \mathbf{u}_2, \mathbf{u}_r), \tag{4.8}$$

where $\mathbf{u}_r$ is the unit vector in the direction of $\mathbf{r}_{12}$, and $f_{l_1 l_2 l}(r)$ are the harmonic expansion coefficients based on a laboratory reference frame. The rotational invariants $\Phi_{l_1 l_2 l}(\mathbf{u}_1, \mathbf{u}_2, \mathbf{u}_r)$ are given by [12]

$$\Phi_{l_1 l_2 l}(\mathbf{u}_1, \mathbf{u}_2, \mathbf{u}_r) = \sum_{m_1 m_2 m} C(l_1 l_2 l; m_1 m_2 m) Y_{l_1 m_1}(\mathbf{u}_1) Y_{l_2 m_2}(\mathbf{u}_2) Y^*_{lm}(\mathbf{u}_r) \tag{4.9}$$

with $C(l_1 l_2 l; m_1 m_2 m)$ the Clebsch-Gordon coefficient, $Y_{lm}(\mathbf{u})$ the spherical harmonics, and * indicates the complex conjugate. Selection rules require that l_1, l_2, l form a triangle, for example, l must obey $|l_1 - l_2| \leqslant l \leqslant (l_1 + l_2)$ [13].

Since our particles have uniaxial and head-to-tail symmetry, l_1, l_2, l are all even and the harmonic expansion coefficients satisfy the symmetry property $h_{l_1 l_2 l}(r) = h_{l_2 l_1 l}(r)$ [12]. Moreover, all of the harmonic expansion coefficients are real, and consequently, their transforms in Fourier space are even.

The direct correlation function $c(1,2) \equiv c(\mathbf{r}_1, \mathbf{u}_1, \mathbf{r}_2, \mathbf{u}_2)$ is defined through the Ornstein-Zernike equation

$$h(1,2) = c(1,2) + \frac{\rho}{4\pi} \int d\mathbf{r}_3 d\mathbf{u}_3 c(1,3) h(3,2), \tag{4.10}$$

where ρ is the number density. Expanding $c(1,2)$ and $h(1,2)$ in rotational invariants (4.8), and applying the Fourier transform, one obtains [13]

$$h_{l_1 l_2 l}(q) = c_{l_1 l_2 l}(q) + (4\pi)^{-3/2} \rho \sum_{l_3 l' l''} h_{l_3 l_2 l''}(q) c_{l_1 l_3 l'}(q) K^{l_1 l_2 l}_{l'' l' l_3} \tag{4.11}$$

with the coefficients

$$K^{l_1 l_2 l}_{l'' l' l_3} = (2l' + 1)(2l'' + 1) \begin{pmatrix} l' & l'' & l \\ 0 & 0 & 0 \end{pmatrix} \begin{Bmatrix} l_1 & l_2 & l \\ l'' & l' & l_3 \end{Bmatrix}, \tag{4.12}$$

where $\begin{pmatrix} l' & l'' & l \\ 0 & 0 & 0 \end{pmatrix}$ and $\begin{Bmatrix} l_1 & l_2 & l \\ l'' & l' & l_3 \end{Bmatrix}$ are the $3j$ and $6j$ symbols, respectively. Here the $\mathbf{r}$-space harmonic expansion coefficients $f_{l_1 l_2 l}(r)$ are related to the $\mathbf{q}$-space harmonic expansion coefficients $f_{l_1 l_2 l}(q)$ through a Hankel transform

$$\begin{aligned} f_{l_1 l_2 l}(q) &= 4\pi i^l \int_0^\infty dr r^2 j_l(qr) f_{l_1 l_2 l}(r), \\ f_{l_1 l_2 l}(r) &= \frac{4\pi}{(2\pi)^3}(-i)^l \int_0^\infty dq q^2 j_l(qr) f_{l_1 l_2 l}(q), \end{aligned} \tag{4.13}$$

where $j_l(qr)$ is the spherical Bessel function. For $l = 0$, the Hankel transform coincides with the Fourier transform (4.2).

The pole analysis for simple fluids described in Section 4.2.1 can be extended to molecular fluids. If we truncate the expansion by imposing an upper limit $l_1, l_2, l \leqslant l_{max}$, the set (4.11) can be solved by rewriting it as a simple matrix equation $A_{ij} h_j = c_i$. The component j of vector h is short for $j = (l_1 l_2 l)$, the q-dependence is dropped for clarity and the elements of matrix A_{ij} are functions of $c_{l_1 l_2 l}(q)$. We give explicit expressions for A_{ij} in the Appendix for $l_{max} = 2$. It is straightforward to derive that $h_j = (A^{-1})_{ji} c_i$ where $(A^{-1})_{ji} = |A|_{ij}/|A|$ with $|A|_{ij}$ the cofactor of matrix element A_{ji}. Hence, $h_{l_1 l_2 l}(q)$ can be expressed as a function of $c_{l_1 l_2 l}(q)$ in the form $h_{l_1 l_2 l}(q) = D_{l_1 l_2 l}(q)/D(q)$. Here $D(q) = |A|$ is the determinant of the coefficients matrix of (4.11) and the determinants $D_{l_1 l_2 l}(q)$ are dependent on the indices $(l_1 l_2 l)$. Both determinants are polynomials in $c_{l_1 l_2 l}(q)$ [84].

The total pair correlation function can now be expressed as

$$h_{l_1 l_2 l}(r) = \frac{(-i)^l}{2\pi^2} \int_0^\infty dq\, q^2 j_l(qr) \frac{D_{l_1 l_2 l}(q)}{D(q)}. \tag{4.14}$$

By analogy with Eq. (4.4), the asymptotic behavior of $h_{l_1 l_2 l}(r)$ is determined by the poles of $h_{l_1 l_2 l}(q)$. This is similar to the case of binary mixtures, for which it was shown explicitly that a common denominator exists for all partial pair correlation functions in Ref. [77]. We stress that the situation here is more complicated than in the case of binary mixtures, although formally there exists a common denominator for all $h_{l_1 l_2 l}(q)$ [77]. The matrix equation (4.11) decouples into separate subsets each corresponding to a different value of l_2. In the Appendix we show explicitly that in the case of binary mixtures, the determinant of the subsets are all equal. For molecular fluids, the coefficients matrix of (4.11) has a block structure, but the dimension of the determinants varies for different values of l_2 as the selection rules exclude certain values of l_1, l_2, l for the expansion coefficients. We now define $|A^{(l_2)}|$ as the determinant of block l_2. The expansion coefficient can be expressed as $h_j = (A^{-1})_{ji}\, c_i$ where $(A^{-1})_{ji} = |A|_{ij}/|A|$ with $|A| = \prod_{l_2'} |A^{(l_2')}|$, and $|A|_{ij} = |A^{(l_2)}|_{ij} \prod_{l_2' \neq l_2} |A^{(l_2')})|$. Hence, $(A^{-1})_{ji}$ reduces to $(A^{-1})_{ji} = |A^{(l_2)}|_{ij}/|A^{(l_2)}|$. The asymptotic behavior of the total correlation functions is determined by the poles and residues of h_j and are thus determined by the zeros of the denominator $|A^{(l_2)}|$.

Consequently, only the harmonics belonging to a particular subset corresponding to a certain value of l_2 share the same determinant and the same pole structure. It should be noted that the determinants for all the subsets contain all the $c_{l_1 l_2 l}(q)$ expansion coefficients, which are allowed by the selection rules.

Employing the symmetry property that the harmonic expansion coefficients are invariant under $l_1 \leftrightarrow l_2$ permutation, we can conclude that determinants corresponding to blocks with different values of l_2, being not equal in general, do share the zeros, and thus all the expansion coefficients again share the same pole structure.

This is similar to the case of (binary) mixtures, where the total pair correlation functions $h_{\alpha\beta}(r)$ of species α and β possess the same characteristic decay length and, if present, oscillatory wavelength for the asymptotic decay [77, 79]. This analogy is clear as each harmonic expansion coefficient in the expansion of the Ornstein-Zernike equation can be regarded as a separate species in a multi-component mixture. It also means that the decay of correlations between two molecules at large distances from each other does not depend on their relative orientations but is determined by the integral properties of the fluid in between. We note that the amplitudes A and the phases θ are dependent on the indices $(l_1 l_2 l)$.

As mentioned before, Eq. (4.11) separates into independent subsets corresponding to different values of l_2. The most convenient subset is certainly the one corresponding to $l_2 = 0$. Selection rules imply that the only nontrivial expansion coefficients in this set are those of type $h_{l0l}(q) \equiv h_l(q)$. The $6j$ symbol contains now a zero in one of the six positions. Employing the symmetry property that the $6j$ symbol is invariant under permutations of the columns, one can evaluate the $6j$ symbol as follows

$$\left\{ \begin{array}{ccc} l_1 & 0 & l \\ l'' & l' & l_3 \end{array} \right\} = \left\{ \begin{array}{ccc} l_1 & l & 0 \\ l'' & l_3 & l' \end{array} \right\} = (-)^{l_1+l''+l'}[(2l_1+1)(2l''+1)]^{-1/2}\delta_{l_1 l}\delta_{l'' l_3}. \quad (4.15)$$

The corresponding set simplifies to a simple matrix equation, which reads

$$h_l(q) = c_l(q) + \rho \sum_k b_{lk}(q) h_k(q), \quad (4.16)$$

where the coefficients $b_{lk}(q)$ are defined as

$$b_{lk}(q) = (4\pi)^{-3/2} \sqrt{\frac{2k+1}{2l+1}} \sum_m (2m+1) \begin{pmatrix} m & k & l \\ 0 & 0 & 0 \end{pmatrix} c_{lkm}(q) \quad (4.17)$$

with $b_{lk}(q) = b_{kl}(q)(2k+1)/(2l+1)$. The asymptotic behavior of $h_{l0l}(r) \equiv h_l(r)$ is determined by the poles of $h_l(q)$

$$D[\delta_{lk} - \rho b_{lk}(\alpha_1 + i\alpha_0)] = 0. \quad (4.18)$$

Thus, the complex values of $q = \alpha_1 + i\alpha_0$, at which one of the eigenvalues of $\rho b_{lk}(q)$ equals 1, govern not only the asymptotic decay of the harmonic expansion coefficients of type $h_{l0l}(r)$ but also of all the other expansion coefficients. The q-space coefficients $b_{lk}(q)$ can be obtained by employing the Hankel transform (4.13) of $c_{l_1 l_2 l}(r)$. In the case of simple fluids, l_{max} can be set to 0 and Eq. (4.18) simplifies to (4.5). We follow the convention, where $c_{000}(r) = (4\pi)^{3/2}c(r)$, with $c(r)$ the direct correlation function averaged over all possible orientations.

We employ the following expression for the spherical Bessel functions

$$j_n(x) = m_{n+1}(x)\sin(x) + p_n(x)\cos(x), \quad (4.19)$$

where $m_{n+1}(x)$ and $p_n(x)$ are polynomials of order $-(n+1)$ and $-n$, respectively, which can be obtained from the recurrence relations [85]. The integration limits in (4.14) can be extended to $(-\infty; \infty)$ and the resulting integral (4.20) can be carried out by contour integration

$$h_l(r) = \frac{(-1)^{l/2}}{4\pi^2} \int_{-\infty}^{\infty} dq q^2 \exp(iqr)[-im_{l+1}(qr) + p_l(qr)] \frac{D_l[\delta_{lk} - \rho b_{lk}(q)]}{D[\delta_{lk} - \rho b_{lk}(q)]}. \quad (4.20)$$

Provided all the poles are simple and leaving only the leading order, we find

$$r^{l+1}h_l(r) = \frac{(-)^{l/2}M_{l+1}}{2\pi}\sum_n q_n^{1-l}\frac{D_l[\delta_{lk}-\rho b_{lk}(q_n)]}{D'[\delta_{lk}-\rho b_{lk}(q_n)]}\exp(iq_nr), \tag{4.21}$$

where M_{l+1} is the coefficient of the leading power in $m_{l+1}(q_nr)$ and $D'[\delta_{lk}-\rho b_{lk}(q_n)]$ denotes the derivative of the determinant of (4.18) at $q = q_n$. Eq. (4.21) generalizes the corresponding expression for simple fluids, and can be used to determine the character of asymptotic decay of correlations in molecular fluids provided the harmonic expansion coefficients $c_{l_1l_2l}(r)$ are known. If the pole with the lowest imaginary value lies on the imaginary axis then the asymptotic decay is pure exponential, otherwise it is determined by a conjugate pair of poles and the asymptotic decay is exponentially damped oscillatory.

The number of harmonic expansion coefficients grows very quickly as l_{max} increases. However, the determinant in (4.18) can be expanded in the density. If we keep only the linear terms in the density, Eq. (4.18) simplifies to

$$(4\pi)^{-3/2}\rho\sum_{lm}(2m+1)\begin{pmatrix} m & l & l \\ 0 & 0 & 0 \end{pmatrix}c_{llm}(\alpha_1+i\alpha_0) = 1. \tag{4.22}$$

In the low density approximation only the diagonal expansion coefficients of the form $c_{llm}(r)$ determine the asymptotic decay of the correlations.

4.3 Hard-rod fluids

The occurrence of both pure imaginary and complex poles in simple fluids is a consequence of the fact that the pair potential contains attractive and repulsive parts. In the case of simple fluids interacting with purely repulsive short-ranged potentials, the asymptotic decay is exponentially damped oscillatory, as the direct correlation function is negative (or close to zero) for all distances [83]. For instance, the asymptotic decay of $h(r)$ in the hard-sphere fluid is exponentially damped oscillatory for all statepoints, even for very low densities. More significantly, perhaps, we did not find any pure imaginary pole, that can give rise to monotonic asymptotic decay, using simulation data [86] for the $c(r)$ of hard spheres [83]. For molecular fluids interacting with purely repulsive short-ranged potentials, there is no such simple argument about whether the asymptotic decay is exponentially damped oscillatory or monotonic. The aim of this chapter is to study the asymptotic decay of the pair correlations in fluids consisting of hard spherocylinders and hard ellipsoids. In particular, we explore whether a pure imaginary pole can be present in hard-rod fluids and, if so, we investigate whether there is a crossover from damped oscillatory decay for hard spheres to monotonic decay upon increasing the aspect ratio. To this end, we determine the harmonic expansion coefficients of the direct correlation function $c_{l_1l_2l}(r)$ by simulations for hard spherocylinders and by different theoretical Ansätze for hard ellipsoids. We describe the simulation results in Sec. 4.3.1 and the theoretical results in Sec. 4.3.2

4.3.1 Simulations

We perform Monte-Carlo simulations of an isotropic fluid of hard spherocylinders, consisting of a cylindrical part with diameter D and length L, and capped with hemispheres

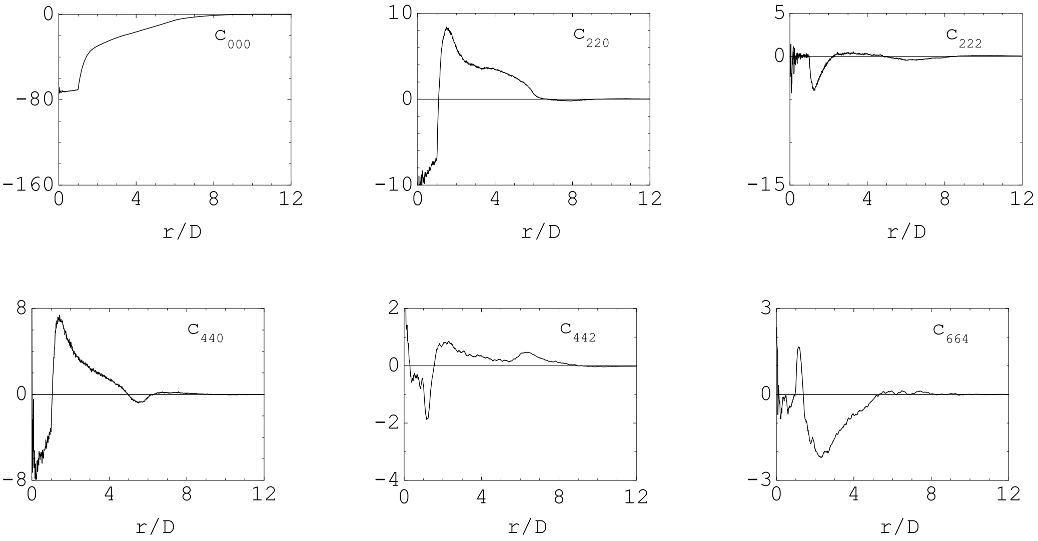

Figure 4.1: The selected harmonic expansion coefficients of the direct correlation function $c_{l_1 l_2 l}(r)$ with $l_1 l_2 l = 000, 220, 222, 440, 442$ and 664 for a fluid of hard spherocylinders with $L/D = 10$ and packing fraction $\eta = 0.1592$ obtained from simulations.

of diameter D at both ends. Note that the full length of the rod is equal to $L + D$. We wish to determine the harmonic expansion coefficients of the direct correlation function in laboratory frame. The approach is similar to Ref. [83], where the Ornstein-Zernike equation was used to determine the direct correlation function $c(r)$ from the total correlation function $h(r)$ measured directly in simulations. In contrast to experiments, where only information of a few harmonics are directly accessible, computer simulations provide a way to measure all the expansion coefficients of the pair correlation function. To this end, we calculate the harmonic expansion coefficients $g_{l_1 l_2 l}(r)$ in bins of width Δr. By applying the orthogonality condition of the spherical harmonics, Eq. (4.8) can be inverted to yield [87]

$$g_{l_1 l_2 l}(r_j) = \frac{(4\pi)^{3/2}[(2l_1+1)(2l_2+1)(2l+1)]^{1/2}}{\rho V(r_j) C(l_1 l_2 l; 000) N} \left\langle \sum_{i=1}^{n_j} P_{l_1}(\cos\theta_1) P_{l_2}(\cos\theta_2) P_l(\cos\theta_r) \right\rangle, \tag{4.23}$$

where N is the number of particles, n_j is the number of particle pairs whose center-of-mass distances are within a range of $r_j \pm \Delta r/2$, $V(r_j)$ denotes the volume of the spherical shell of thickness Δr centered at r_j, and $C(l_1 l_2 l; 000)$ are the Clebsch-Gordan coefficients. The standard polar and azimuthal angles $\mathbf{u}_i = (\theta_i, \phi_i)$ are used for the orientations of particle i with $0 \leqslant \theta_i \leqslant \pi$ and $0 \leqslant \phi_i \leqslant 2\pi$.

The only relevant parameters that determine the thermodynamic properties of a fluid of hard spherocylinders are the number density and the length-to-diameter ratio L/D. We perform simulations of a system consisting of hard spherocylinders with a length-to-diameter ratio of $L/D = 5$ and 10 at densities below the bulk isotropic-nematic transition ($\eta^{IN}_{L/D=5} = 0.40, \eta^{IN}_{L/D=10} \approx 0.24$ [18]). The simulations are started from an initial configuration with all the center-of-masses of the rods distributed randomly in the simulation box, but all the orientations aligned along one direction. We check for equilibrium by monitoring the nematic order parameter. When equilibrium is reached, we perform production runs of 10^6 sweeps. The harmonic expansion coefficients of the pair correlation function are sampled every sweep up to $l_{max} = 10$. The $g_{l_1 l_2 l}(r)$ profiles are accumulated in bins of width $\Delta r = D/10$. The simulations are computationally more expensive with increasing L/D. For instance, the simulation for $L/D = 10$ at a density just below the bulk isotropic-nematic transition takes about two months of '500MHz R14000' processor time. We are therefore restricted to length-to-diameter ratios $L/D \leqslant 10$.

In contrast to earlier simulations, where the expansion coefficients were sampled in molecular frame for calculating $c(1,2)$ in fluids of hard ellipsoids [88], we are able to apply the Hankel transform directly to obtain the set of $g_{l_1 l_2 l}(q)$ from which we can extract $h_{l_1 l_2 l}(q)$ through $h_{l_1 l_2 l}(q) = g_{l_1 l_2 l}(q) - (4\pi)^{3/2}\delta_{0l_1}\delta_{0l_2}\delta_{0l}$. Subsequently, we solve the set (4.11) to find $c_{l_1 l_2 l}(q)$. Applying the inverse Hankel transform, we obtain the harmonic expansion coefficients $c_{l_1 l_2 l}(r)$. Fig. 4.1 shows simulation results for a fluid of $N = 600 - 1200$ hard spherocylinders in a volume V with $L/D = 10$ and packing fraction $\eta = (\pi D^3/6 + \pi L D^2/4)N/V = 0.1592$. Fig. 4.1 shows only a selection of the harmonic expansion coefficients $c_{l_1 l_2 l}(r)$. All the functions are short-ranged and decay rapidly outside the overlap region $r > L + D$. At small r, the accuracy of $c_{l_1 l_2 l}(r)$ decreases significantly with increasing values of l_1, l_2, l, which is due to the truncation of the Hankel transform. However, this does not have a strong impact on the values obtained for the poles [83]. Fig. 4.1 shows that the position-position correlation function $c_{000}(r)$ is negative inside the core, while the orientation-orientation correlation function $c_{220}(r)$ is mostly positive, indicating an effective attraction between the rods with similar orientations. Fig. 4.2 shows $c_{000}(r)$ for a hard spherocylinder fluid with $L/D = 5$ and $L/D = 10$ at varying packing fractions. The direct correlation function averaged over all possible orientations, i.e., $c_{000}(r)$, is negative inside the core independent of L/D, while it oscillates close to zero outside the core. This is similar to the case of hard spheres with diameter D. Groot *et al.* found a rapidly decaying tail in $c(r)$ with $|c(r)| \leqslant 0.01$ for $r > 2D$ using simulation data for $h(r)$ in the OZ equation [86]. We observe clearly in Fig. 4.2 that $c_{000}(r)$ becomes more negative inside the core as the packing fraction increases and the effect of repulsion becomes more important.

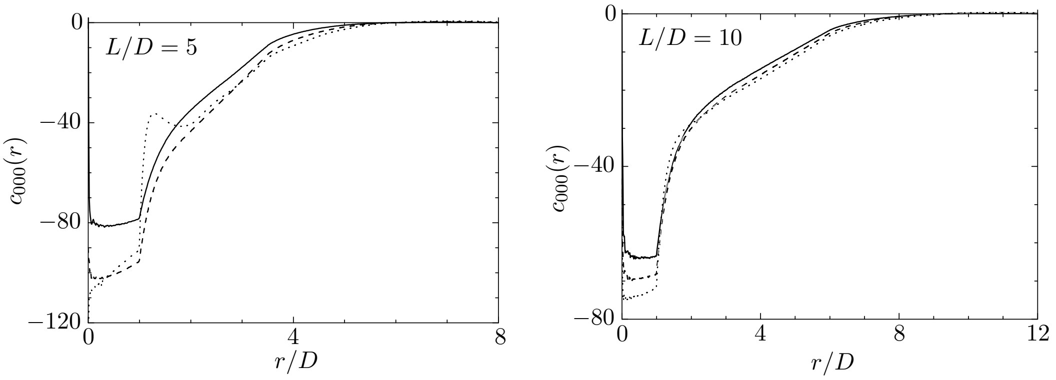

Figure 4.2: Simulation results for the harmonic expansion coefficient of the direct correlation function $c_{000}(r)$ for a fluid of hard spherocylinders with a length-to-diameter ratio $L/D = 5$ (left) and packing fractions — $\eta = 0.0979$, $--$ $\eta = 0.2003$, $\cdots$ $\eta = 0.3694$, and $L/D = 10$ (right) and packing fractions — $\eta = 0.0922$, $--$ $\eta = 0.1257$, $\cdots$ $\eta = 0.1927$.

4.3.2 Model functions

In addition to the simulations, we also use two theoretical model expressions for the direct correlation function. The first one is the Pynn [89] and Wulf [90] Ansatz: $c_{Pynn}(1,2) = c_{HS}(r/\sigma(1,2),\eta)$, where c_{HS} is the hard-sphere function evaluated at the same packing fraction η as the molecular fluid, and $\sigma(1,2) = \sigma(\hat{u}_1,\hat{u}_2,\hat{r}_{12})$ is the closest approach distance for given orientations of molecules and center-center vector. The latter can easily be calculated for hard ellipsoids of revolution [91]. Another Ansatz, we employ is due to Parsons [92] and Lee [93]. It approximates the direct correlation function by a density-scaled Mayer function $c_{Parsons}(1,2) = \varphi(\eta)f(1,2)$. The Mayer function $f(1,2) = -1$ for $r \leqslant \sigma(1,2)$ and $f(1,2) = 0$ for $r > \sigma(1,2)$. The weight function reads $\varphi(\eta) = (1-\eta/4)/(1-\eta)^4$, which produces an accurate equation of state for hard spheres. We calculate the harmonic expansion coefficients for $c_{l_1 l_2 l}(r)$ of a fluid consisting of hard ellipsoids using the Pynn-Wulf and Parsons-Lee approximations. A selection of $c_{l_1 l_2 l}(r)$ is shown in Fig. 4.3 for hard ellipsoids with an elongation of $a/b = 10$ and packing fraction $\eta = \pi a b^2 N/6V = 0.1592$. The major and minor axis of the ellipsoids are denoted by a and b, respectively. For the theoretical Ansätze, we calculate only those harmonics that are required for the low density approximation (4.22) with $l_{max} = 10$. While the particle shape is different in our simulations and in our theories, the overall features of $c_{l_1 l_2 l}(r)$ are similar. For instance, in both simulation and theory, $c_{000}(r)$ is negative, and $c_{220}(r)$ and $c_{440}(r)$ are mostly positive inside the overlap region. In spite of moderate success of the theoretical ansätze in the partial overlap region, inside the core region $r/b < 1$ they fail to provide an adequate description. Indeed, the Parsons scaling depends on the Mayer $f(1,2)$ function which is identically equal to -1 inside the core $r/b < 1$ (so that only $c_{000}(r)$ is different from 0), while the Pynn approximation predicts the isotropic function in the limit $r \to 0$, so it fails to describe the harmonics which are not equal to zero at $r = 0$.

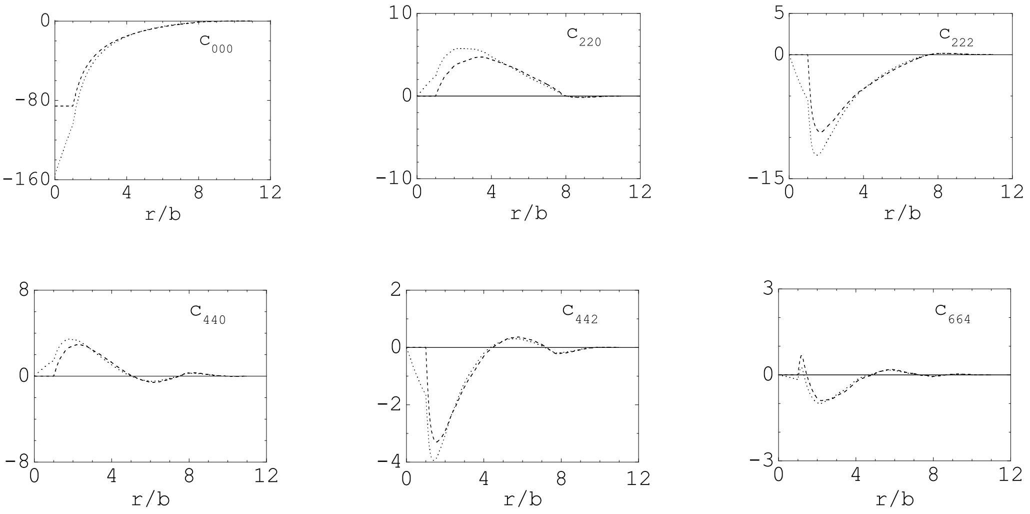

Figure 4.3: The selected harmonic expansion coefficients of the direct correlation function $c_{l_1 l_2 l}(r)$ with $l_1 l_2 l = 000, 220, 222, 440, 442$ and 664 for a fluid of hard ellipsoids with elongation $a/b = 10$ and packing fraction $\eta = 0.1592$ obtained from the Pynn-Wulff [89, 90] (dotted) and Parsons-Lee [92, 93] (short-dashed) Ansätze.

4.4 Results and discussion

We investigate the asymptotic decay of the total pair correlation functions for a fluid of hard rods. We obtain the leading poles of $h_{l_1l_2l}(q)$ for a hard spherocylinder fluid by solving Eq. (4.18) employing the harmonic expansion coefficients of the direct correlation functions obtained from simulations, which were described in Sec. 4.3.1. In order to locate the pure imaginary pole, we consider only the real part of (4.18) with the fixed value of $\alpha_1 = 0$. Results for the pure imaginary pole and the pole off the imaginary axis with the smallest value of α_0 are shown in Fig. 4.4 for hard spherocylinders with $L/D = 5$ and 10, at varying densities in the isotropic phase ranging from very dilute to just below the density at the bulk isotropic-nematic transition, and $l_{max} = 10$. For comparison, we also plot the results for the leading poles by solving Eq. (4.7), i.e, using only $c_{000}(r)$, corresponding to $l_{max} = 0$, as in the case of spherically symmetric pair potential, and by solving Eq. (4.22) with $l_{max} = 10$, which is based on a low density approximation. We also check for convergence with respect to l_{max} in Eq. (4.18) for $L/D = 10$. The results for $l_{max} = 2$ for the lowest lying conjugate pair of poles are shown by a dashed line in Fig. 4.4. We find that it approaches the results of $l_{max} = 10$ very closely. For the pure imaginary pole, we find bad convergence for $l_{max} = 2$, while good agreement is found for $l_{max} = 4$. The crossed squares denote the results for $l_{max} = 4$. For all our simulations, we find that $l_{max} = 10$ is sufficient to provide good convergence. Fig. 4.4 shows that the period $2\pi/\alpha_1$ obtained from the low density approximation (4.22) is larger than that obtained from the $l_{max} = 0$ approximation (4.7). On the other hand, the inverse decay length α_0 from the low density approximation with $l_{max} = 10$ (4.22) is smaller than that of the $l_{max} = 0$ approximation (4.7). The poles calculated using $l_{max} = 10$ in Eq. (4.18)

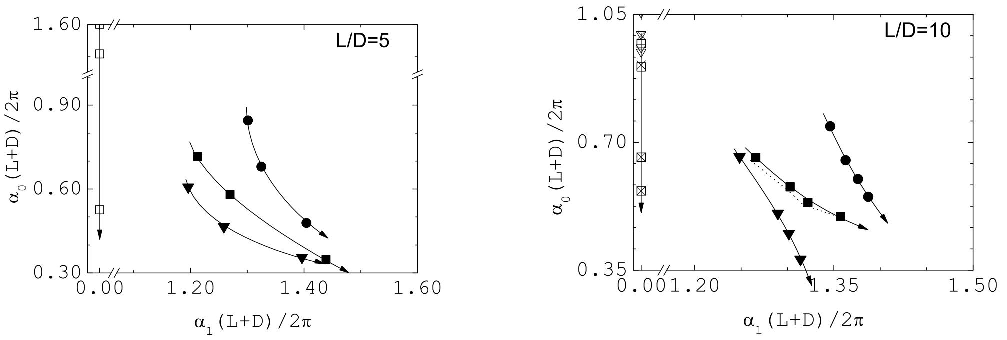

Figure 4.4: The imaginary (α_0) and real (α_1) part of the leading poles obtained from simulations of a fluid of hard spherocylinders with a length-to-diameter ratio $L/D = 5$ (left) and $L/D = 10$ (right). The symbols with $\alpha_1 = 0$ refer to the pure imaginary pole (open symbols) while those with $\alpha_1 L/2\pi \sim 1.3$ refer to the lowest-lying complex pair $q = \pm\alpha_1 + i\alpha_0$ (filled symbols, only the pole with $\alpha_1 > 0$ is shown). The circles denote the results using the $l_{max} = 0$ approximation (4.7), the triangles show the results using the low-density approximation (4.22) with $l_{max} = 10$, and the squares the results for $l_{max} = 10$ in Eq. (4.18). The arrows denote the direction, in which the density is increased. The dashed line show the results for $l_{max} = 2$ in Eq. (4.18) for the complex pole, while the crossed squares denote the results for $l_{max} = 4$ for the pure imaginary pole, showing the good convergence of l_{max} for $L/D = 10$.

	$l_{max} = 0$, Eq. (4.7)	$l_{max} = 10$, Eq. (4.22) low density	$l_{max} = 10$, Eq. (4.18)
$L/D = 0$	no	-	-
$L/D = 5$	no	no	yes
$L/D = 10$	no	yes	yes

Table 4.1: The occurrence of a pure imaginary pole in simulations of hard spheres ($L/D = 0$) and hard spherocylinders ($L/D = 5$ and 10) using different approximations.

lie between the two approximations of Eq. (4.7) and (4.22).

In the case of the low density approximation (4.22) and the $l_{max} = 0$ approximation (4.7), we did not find a pure imaginary pole for $L/D = 5$ and we plot only the lowest lying conjugate pair of poles in Fig. 4.4 for the two approximations. For $L/D = 10$, we do find a pure imaginary pole for the low density approximation (4.22) using $l_{max} = 10$, while it is absent for the $l_{max} = 0$ approximation (4.7). In Table 1, we summarize the presence or absence of the pure imaginary poles using different approximations and varying L/D. We conclude that the appearance of a pure imaginary pole is more related to the positive parts of the higher harmonic expansion coefficients in (4.18) than to the tiny positive tail in $c_{000}(r)$ outside the core region. As for $L/D = 10$, the pure imaginary pole can even be found using the low density approximation with $l_{max} = 10$ in contrast with $L/D = 5$, it is tempting to argue that the occurrence of the monotonic pole is less sensitive for larger L/D. In addition, we found good convergence for the value of the monotonic pole using $l_{max} = 4$ in Eq. (4.18) for $L/D = 10$, and we can argue that the occurrence of the monotonic pole is due to the positive part of $c_{220}(r)$ and $c_{440}(r)$.

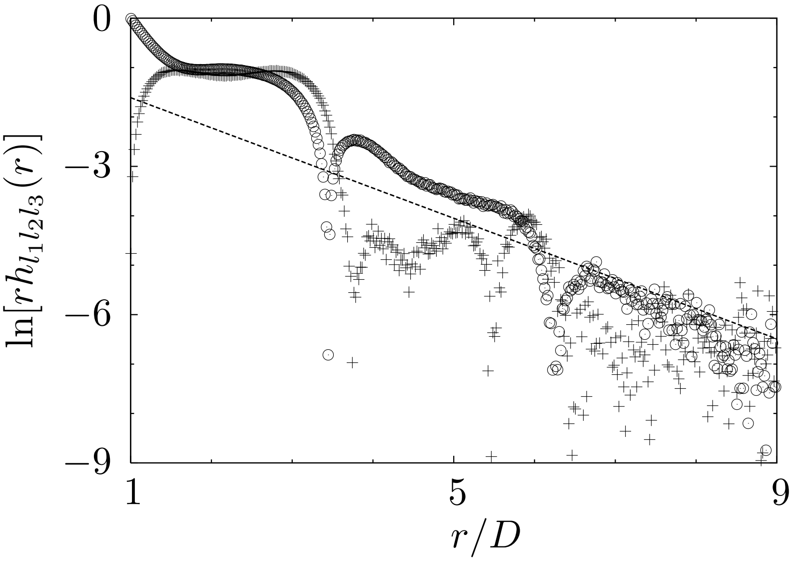

Figure 4.5: The harmonic expansion coefficients of the total correlation functions obtained from simulations for a fluid of hard spherocylinders with a length-to-diameter ratio $L/D = 5$, and packing fraction $\eta = 0.2003$: ∘ ∘ ∘ $\ln[rh_{000}(r)]$, + + + $\ln[rh_{220}(r)]$. The dashed line is the slope predicted for the exponential decay using the pole analysis (4.18).

As expected, the inverse decay length α_0 decreases with increasing density. The variation of the period $2\pi/\alpha_1$ is weak and changes roughly from $0.85\ L$ to $0.70\ L$ with increasing density. We find that the imaginary part of both the pure imaginary pole and the lowest lying complex pole becomes smaller, upon increasing the density toward the value at the isotropic-nematic transition. In addition, the difference between the two imaginary parts decreases with increasing density. However, we find that for all statepoints in Fig. 4.4, the complex pole has always the smallest value of α_0. Consequently, the asymptotic decay of the total pair correlation function is exponentially damped oscillatory for a fluid of hard spherocylinders with $L/D \leqslant 10$ at all densities in the isotropic fluid phase. For packing fractions just below the bulk isotropic-nematic transition, the pure imaginary pole and the lowest lying complex pole $(\alpha_1(L+D)/2\pi, \alpha_0(L+D)/2\pi)$ are given by (0, 0.53) and (1.44, 0.35) for $L/D = 5$, and for $L/D = 10$ by (0, 0.57) and (1.36, 0.50). The difference between the imaginary parts of the imaginary and the complex pole decreases from 0.18 for $L/D = 5$ to 0.07 for $L/D = 10$. As our simulations are limited to $L/D \leqslant 10$, we are unable to investigate whether the monotonic pole will have a smaller imaginary part than the complex pole and will become dominant upon increasing the aspect ratio. It remains therefore an open question whether the asymptotic decay of the total pair correlation function crosses over from exponentially damped oscillatory to monotonic upon increasing the aspect ratio.

In addition, we performed very long simulations (5×10^6 cycles) in order to study the similarity of the decay of the harmonic expansion coefficients. In Fig. 4.5, we compare the simulation results for two harmonic expansion coefficients of the total correlation function $h_{000}(r)$ and $h_{220}(r)$ for $L/D = 10$ and $\eta = 0.2003$. For comparison, we also show the slope predicted for the exponential decay using the pole analysis (4.18). As the statistical accuracy of $h_{000}(r)$ and $h_{220}(r)$ is poor, it is hard to make any definite statements on the decay of the harmonics. However, it is tempting to conclude that the two expansion coefficients $h_{000}(r)$ and $h_{220}(r)$ decay similarly at intermediate range and seem to agree with the decay predicted by the pole analysis.

We also employ the theoretical results for the direct correlation function as described in Sec. 4.3.2 in our pole analysis. We obtain the leading poles of $h_{l_1 l_2 l}(q)$ for a fluid of hard ellipsoids using the $l_{max} = 0$ approximation (4.7) and the low-density approximation (4.22) with $l_{max} = 10$ employing $c_{l_1 l_2 l}(r)$ obtained from the Pynn-Wulff and Parsons-Lee Ansätze. We did not find a pure imaginary pole using these Ansätze. Comparing $c_{220}(r)$ and $c_{440}(r)$ in Fig. 4.1 and 4.3, we observe that the positive part, which is responsible for the occurrence of the monotonic pole in the simulations, is smaller in the theoretical Ansätze and apparently too weak to predict a pure imaginary pole. Fig. 4.6 shows only results for the lowest lying complex pole with the smallest value of α_0 for a fluid of hard ellipsoids with an elongation of $a/b = 5$ and 10, at varying densities. The inverse decay length α_0 decreases upon increasing the density using the Parsons-Lee approximation in agreement with simulations. However, the Pynn-Wulff approximation shows that the value of α_0 decreases and increases later upon increasing the density.

In Fig. 4.7, we show the lowest lying complex pole using the Parsons-Lee approximation for a fluid of hard ellipsoids for several packing fractions and varying elongations $1 \leqslant a/b \leqslant 25$. We only show results using the low-density approximation (4.22) with $l_{max} = 10$. Fig. 4.7 shows that the period of the oscillations $2\pi/\alpha_1$ scales roughly with the major axis of the ellipsoids, but decreases slightly upon increasing a/b. For an elongation equal to one, the results are in agreement with those for hard spheres [83].

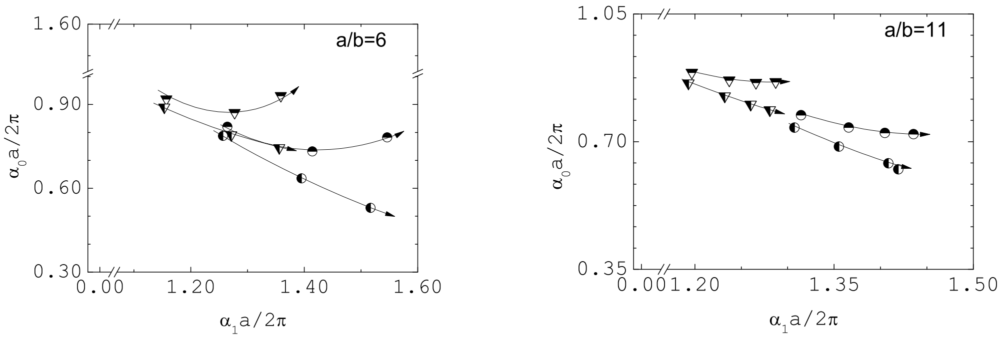

Figure 4.6: The imaginary (α_0) and real (α_1) part of the lowest-lying conjugate pole $q = \pm\alpha_1 + i\alpha_0$ (only the pole with $\alpha_1 > 0$ is shown) of a fluid of hard ellipsoids with an aspect ratio $a/b = 5$ (left) and $a/b = 10$ (right). The circles denote the results using the $l_{max} = 0$ approximation (4.7) and the triangles the results using the low-density approximation (4.22) with $l_{max} = 10$ employing the Pynn-Wulff [89, 90] (upper half filled) and the Parsons-Lee [92, 93] (left half filled) Ansätze. The arrows denote the direction, in which the density is increased. No pure imaginary pole is found.

In conclusion, we have investigated the asymptotic decay of the total pair correlation functions in fluids consisting of hard spherocylinders and hard ellipsoids. We determined the harmonic expansion coefficients of the direct correlation function $c_{l_1 l_2 l}(r)$ by simulations for hard spherocylinders using the OZ equation and by different theoretical Ansätze for hard ellipsoids. We have shown that the anisotropy of the particles plays an important role in the asymptotic decay of molecular fluids. Although the pair potential is purely repulsive for hard rods, we do find the occurrence of a pure imaginary pole in our simulation results. However, for all densities in the isotropic fluid phase, the oscillatory pole has a smaller imaginary part than the pure imaginary pole, and the asymptotic decay of the total pair correlation function is damped oscillatory for length-to-diameter ratios $L/D \leqslant 10$. It remains an open question whether the decay of the total correlation function at longest range crosses over from damped oscillatory to monotonic upon increasing L/D. Employing the $c_{l_1 l_2 l}(r)$ for hard ellipsoids obtained from the Parsons-Lee and Pynn-Wulff approximations, no pure imaginary pole was found. Consequently, the asymptotic decay is predicted to be exponentially damped oscillatory for all elongations. In this chapter, we have limited ourselves to the asymptotic decay of pair correlations in bulk fluids of particles interacting with anisotropic pair potentials. It is interesting to investigate whether the pole structure given by $h_{l_1 l_2 l}(q)$ determines not only the decay of the total correlation functions in a bulk fluid but also the decay of the one body density profiles at wall-fluid interfaces. We plan to study this in future work.

Acknowledgments

We thank René van Roij, Bob Evans, and Matthias Schmidt for stimulating discussions. We also thank René van Roij for a critical reading of the manuscript. We acknowledge the Dutch National Computer Facilities Foundation for access to the SGI Origin3800.

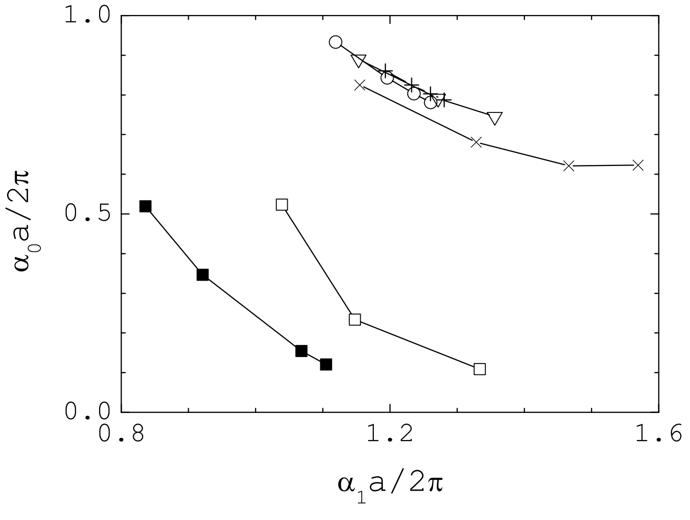

Figure 4.7: The imaginary (α_0) and real (α_1) part of the lowest-lying conjugate pole $q = \pm\alpha_1 + i\alpha_0$ (only the pole with $\alpha_1 > 0$ is shown) of a fluid of hard ellipsoids for varying densities in the isotropic fluid phase and varying aspect ratios $a/b = 1\ (\blacksquare), 1.5\ (\square), 3.2\ (\times), 6.0\ (\bigtriangledown), 11\ (+), 25\ (\circ)$ using the low-density approximation (4.22) with $l_{max} = 10$ and employing the Parsons-Lee [92, 93] Ansätze.

4.A Appendix

4.A.1 Binary fluid mixtures

The pole analysis can easily be extended to binary mixtures. The OZ equation for a binary (α, β) mixture in Fourier space reads [77]

$$h_{\alpha\beta}(q) = c_{\alpha\beta}(q) + \sum_{\gamma} \rho_\gamma c_{\alpha\gamma}(q) h_{\gamma\beta}(q) \tag{4.A.1}$$

where ρ_γ is the number density of species γ. It is convenient to write the OZ equation in a simple matrix equation of the form $A_{ij}h_j = c_i$, where component j of vector h is short for $j = (\alpha\beta)$, the q-dependence is dropped for clarity, and the elements of matrix A_{ij} are functions of $c_{\alpha\beta}$:

$$\begin{pmatrix} 1-\rho_1 c_{11} & -\rho_2 c_{12} & & \\ -\rho_1 c_{12} & 1-\rho_2 c_{22} & & \\ & & 1-\rho_1 c_{11} & -\rho_2 c_{12} \\ & & -\rho_1 c_{12} & 1-\rho_2 c_{22} \end{pmatrix} \begin{pmatrix} h_{11} \\ h_{21} \\ h_{12} \\ h_{22} \end{pmatrix} = \begin{pmatrix} c_{11} \\ c_{21} \\ c_{12} \\ c_{22} \end{pmatrix} \tag{4.A.2}$$

The coefficients matrix A_{ij} has a block structure with identical blocks for each β. We define $|A^{(\beta)}|$ as the determinant of block β, which are identical for each β. It is straightforward to derive that $h_j = (A^{-1})_{ji}\, c_i$ where $(A^{-1})_{ji} = |A|_{ij}/|A|$ with $|A|$ the product of two identical determinants, $|A| = \prod_\beta |A^{(\beta)}|$, and $|A|_{ij} = |A^{(\beta)}|_{ij} \prod_{\alpha\neq\beta} |A^{(\alpha)}|$ the cofactor of matrix element A_{ji}. Hence, $(A^{-1})_{ji}$ reduces to $(A^{-1})_{ji} = |A^{(\beta)}|_{ij}/|A^{(\beta)}|$. The asymptotic behavior of the total correlation functions are determined by the poles and residues of h_j. As these are determined by the zeros of a denominator $|A^{(\beta)}|$, which is identical for each β, all $h_j \equiv h_{\alpha\beta}(q)$ exhibit the same pole structure and all $h_{\alpha\beta}(r)$'s have the same asymptotic decay. However, the amplitudes are dependant on indices $\alpha\beta$. It is straightforward to extend the pole analysis to multi-component mixtures yielding that there is only one decay length and (if applicable) one oscillatory wavelength that specifies the asymptotic decay of all partial total correlation functions $h_{\alpha\beta}(r)$.

4.A.2 Molecular Fluids

In a similar way, the OZ equation for molecular fluids (4.11) can be expressed as a simple matrix equation of the form $A_{ij}h_j = c_i$. The component j of vector h corresponds to $j = (l_1 l_2 l)$. We give explicit expressions for A_{ij} for $l_{max} = 2$. We first set $K^{l_1 l_2 l}_{l'' l' l_3}$ to one for all values of $(l'', l', l_3, l_1, l_2, l)$ and ignore the selection rules for the indices $l_1 l_2 l$. The matrix equation reads

$$\left(\begin{array}{c|c} A_{ij}^{(l_2=0)} & \emptyset \\ \hline \emptyset & A_{ij}^{(l_2=2)} \end{array}\right) \begin{pmatrix} h_{000} \\ h_{002} \\ h_{200} \\ h_{202} \\ h_{020} \\ h_{022} \\ h_{220} \\ h_{222} \end{pmatrix} = \begin{pmatrix} c_{000} \\ c_{002} \\ c_{200} \\ c_{202} \\ c_{020} \\ c_{022} \\ c_{220} \\ c_{222} \end{pmatrix} \tag{4.A.3}$$

where $A_{ij}^{(l_2=0)} = A_{ij}^{(l_2=2)}$ and reads

$$A_{ij}^{(l_2)} = \begin{pmatrix} 1-\hat{\rho}c_{000}-\hat{\rho}c_{002} & -\hat{\rho}c_{000}-\hat{\rho}c_{002} & -\hat{\rho}c_{020}-\hat{\rho}c_{022} & -\hat{\rho}c_{020}-\hat{\rho}c_{022} \\ -\hat{\rho}c_{000}-\hat{\rho}c_{002} & 1-\hat{\rho}c_{000}-\hat{\rho}c_{002} & -\hat{\rho}c_{020}-\hat{\rho}c_{022} & -\hat{\rho}c_{020}-\hat{\rho}c_{022} \\ -\hat{\rho}c_{200}-\hat{\rho}c_{202} & -\hat{\rho}c_{200}-\hat{\rho}c_{202} & 1-\hat{\rho}c_{220}-\hat{\rho}c_{222} & -\hat{\rho}c_{220}-\hat{\rho}c_{222} \\ -\hat{\rho}c_{200}-\hat{\rho}c_{202} & -\hat{\rho}c_{200}-\hat{\rho}c_{202} & -\hat{\rho}c_{220}-\hat{\rho}c_{222} & 1-\hat{\rho}c_{220}-\hat{\rho}c_{222} \end{pmatrix} \tag{4.A.4}$$

We define $\hat{\rho} = (4\pi)^{-3/2}\rho$. The coefficients matrix A_{ij} decouples into separate subsets, which are all equal, for each value of l_2. However, if we include $K^{l_1 l_2 l}_{l'' l' l_3}$ and employ the selection rules, certain values of l_1, l_2, l for the expansion coefficients vanish and, we find:

$$\left(\begin{array}{c|c} A_{ij}^{(l_2=0)} & \emptyset \\ \hline \emptyset & A_{ij}^{(l_2=2)} \end{array}\right) \begin{pmatrix} h_{000} \\ h_{202} \\ h_{022} \\ h_{220} \\ h_{222} \end{pmatrix} = \begin{pmatrix} c_{000} \\ c_{202} \\ c_{022} \\ c_{220} \\ c_{222} \end{pmatrix} \tag{4.A.5}$$

where

$$A_{ij}^{(l_2=0)} = \begin{pmatrix} 1-\hat{\rho}c_{000} & -5\hat{\rho}c_{022} \\ -\hat{\rho}c_{202} & 1-\sqrt{\frac{1}{5}}\hat{\rho}c_{220}+\sqrt{\frac{10}{7}}\hat{\rho}c_{222} \end{pmatrix}, \tag{4.A.6}$$

and

$$A_{ij}^{(l_2=2)} = \begin{pmatrix} 1-\hat{\rho}c_{000} & -\sqrt{\frac{1}{5}}\hat{\rho}c_{022} & \sqrt{\frac{10}{7}}\hat{\rho}c_{022} \\ -\sqrt{5}\hat{\rho}c_{202} & 1-\sqrt{\frac{1}{5}}\hat{\rho}c_{220} & -\sqrt{5}\hat{\rho}c_{222} \\ -\sqrt{\frac{10}{7}}\hat{\rho}c_{202} & -\sqrt{\frac{1}{5}}\hat{\rho}c_{222} & 1-\sqrt{\frac{1}{5}}\hat{\rho}c_{220}-\frac{3}{7}\sqrt{\frac{5}{14}}\hat{\rho}c_{222} \end{pmatrix}. \qquad (4.A.7)$$

The coefficients matrix A_{ij} has still a block structure and decouples into separate subsets corresponding to different values of l_2. However, the dimension of the subsets differ for different values of l_2. We define $|A^{(l_2)}|$ as the determinant of block l_2. The expansion coefficient can now be expressed as $h_j = (A^{-1})_{ji}\, c_i$ where $(A^{-1})_{ji} = |A|_{ij}/|A|$ with $|A| = \prod_{l'_2} |A^{(l'_2)}|$, and $|A|_{ij} = |A^{(l_2)}|_{ij} \prod_{l'_2 \neq l_2} |A^{(l'_2)}|$. Hence, $(A^{-1})_{ji}$ reduces to $(A^{-1})_{ji} = |A^{(l_2)}|_{ij}/|A^{(l_2)}|$. The asymptotic behavior of the total correlation functions is determined by the poles and residues of $h_j \equiv h_{l_1 l_2 l}(q)$ and are, thus, determined by the zeros of a denominator $|A^{(l_2)}|$. Consequently, only the harmonics belonging to a particular subset corresponding to a certain value of l_2 share the same determinant and the same pole structure. Employing the symmetry property that the harmonic expansion coefficients are invariant under $l_1 \leftrightarrow l_2$ permutation, we find that the determinants of different blocks, which are not equal in general, should share the zeros, i.e., $h_{l_1 l_2 l}(q)$ should exhibit the same pole structure as $h_{l_2 l_1 l}(q)$, resulting in the same asymptotic decay of $h_{l_1 l_2 l}(r)$ and $h_{l_2 l_1 l}(r)$. More explicitly, in the case of $l_{max} = 2$, we find a common asymptotic decay for $h_{000}(r)$ and $h_{202}(r)$ and for $h_{022}(r)$, $h_{220}(r)$, and $h_{222}(r)$. The $l_1 \leftrightarrow l_2$ symmetry property yields that the asymptotic decay of $h_{202}(r)$ and $h_{022}(r)$ are equal and, hence, all $h_{l_1 l_2 l}(r)$ have the same asymptotic decay.

4.B Asymptotic decay of the pair correlation function in Onsager theory.

The approach that we used to determine the pole structure for the two Ansätze is identical to the one that was used in simulations. However, the Onsager theory as well as the Parsons-Lee ansätz allows for a more straightforward treatment. Here we will only discuss the Onsager theory, although the derivation follows the same line for the Parsons-Lee ansätze.

The Onsager theory describes a fluid of long rods with an aspect ratio $L/D \to \infty$. Using the second virial approximation, the excess free enrgy reads

$$\beta F[\rho] = \int d\vec{r} d\hat{\omega} \rho(\vec{r},\hat{\omega})(\log\rho(\vec{r},\hat{\omega})-1) - \frac{1}{2}\int d\vec{r} d\hat{\omega} d\vec{r}' d\hat{\omega}' f_M(\vec{r},\hat{\omega};\vec{r}'\hat{\omega}')\rho(\vec{r},\hat{\omega})\rho(\vec{r}',\hat{\omega}'), \qquad (4.B.1)$$

one can see that the direct correlation function for this model is simply equal to the Mayer function

$$c_{Ons}(\vec{r},\hat{\omega};\vec{r}'\hat{\omega}') = f_M(\vec{r},\hat{\omega};\vec{r}'\hat{\omega}'), \qquad (4.B.2)$$

where the Mayer function $f_M(\vec{r},\hat{\omega};\vec{r}'\hat{\omega}') = \exp[-\beta u(\vec{r},\hat{\omega};\vec{r}'\hat{\omega}')] - 1$ equals -1 for overlapping rods and 0 if the rods do not overlap.

Then the Fourier transform $c(\vec{q};\hat{\omega}_1,\hat{\omega}_2)$ of the direct correlation function can be calculated analytically. In the limit $L/D \to \infty$ we can neglect contributions due to cap-cap and cap-cylinder interactions, and thus only the cylinder-cylinder contributions are discussed here.

Two cylinders with orientations $\hat{\omega}_1$ and $\hat{\omega}_2$, length L and diameter D overlap if the separation $\vec{r}_{cc}$ of the two centers of mass is in the parallelepiped described by

$$\vec{r}_{cc} = \frac{L}{2} r_1 \hat{\omega}_1 + \frac{L}{2} r_2 \hat{\omega}_2 + D r_3 \hat{v} \quad (-1 \leqslant r_i \leqslant 1 \text{ for } i = 1, 2, 3), \tag{4.B.3}$$

where the unit vector $\hat{v}$ is given by $\hat{v} = (\hat{\omega}_1 \times \hat{\omega}_2)/\sin\gamma$, and $\sin\gamma$ is the sine of the angle between $\hat{\omega}_1$ and $\hat{\omega}_2$. The integration with Jacobian $d\vec{r}_{cc} = \frac{1}{4} L^2 D \sin\gamma dr_1 dr_2 dr_3$ yields

$$\begin{aligned} c(\vec{q}; \hat{\omega}_1, \hat{\omega}_2) &= -\int d\vec{r}_{cc} \exp(i\vec{q}\vec{r}_{cc}) \\ &= -2L^2 D \sin\gamma j_0(D\vec{q} \cdot \hat{v}) j_0(\frac{L}{2}\vec{q} \cdot \hat{\omega}_1) j_0(\frac{L}{2}\vec{q} \cdot \hat{\omega}_2). \end{aligned} \tag{4.B.4}$$

It is most convenient to expand the direct correlation function (4.B.4) in molecular frame, i.e. the frame with one of the axes aligned along $\vec{r}_2 - \vec{r}_1$ direction

$$c_{l_1 l_2 m}(q) = \int d\Omega_1 d\Omega_2 c_{mf}(q, \hat{\omega}_1, \omega_2) Y_{l_1 \underline{m}}(\omega_1) Y_{l_2 m}(\omega_2), \tag{4.B.5}$$

with the c_{mf} standing for the direct correlation function (4.B.4) with the arguments of the Bessel functions j_0 calculated in molecular frame

$$\begin{aligned} &c_{mf}(q, \hat{\omega}_1, \hat{\omega}_2) = \\ &\quad -2L^2 D \sin\gamma j_0\left(\frac{L}{2} q \cos\theta_1\right) j_0\left(\frac{L}{2} q \cos\theta_2\right) j_0\left(\frac{Dq \sin\theta_1 \sin\theta_2}{\sin\gamma} \sin(\phi_2 - \phi_1)\right). \end{aligned} \tag{4.B.6}$$

After some manipulation the expansion coefficients of the direct correlation function in Fourier space can written as

$$c_{l_1 l_2 m}(q) = a_{l_l l_2 m} \int_{-1}^{1} dx_1 P_{l_1 m}(x_1) j_0\left(\frac{L}{2} q x_1\right) \int_{-1}^{1} dx_2 P_{l_2 m}(x_2) j_0\left(\frac{L}{2} q x_2\right) K_m(x_1, x_2), \tag{4.B.7}$$

with x_1, and x_2 standing for $\cos\theta_1$ and $\cos\theta_2$ correspondingly,

$$a_{l_1 l_2 m} \equiv (-)^{m+1} 8\pi L^2 D \sqrt{\frac{(2l_1+1)(2l_2+1)}{(4\pi)^2} \frac{(l_1-m)!(l_2-m)!}{(l_1+m)!(l_2+m)!}}, \tag{4.B.8}$$

and

$$\begin{aligned} K_m(x_1, x_2) &\equiv \lim_{D \to 0} \int_0^\pi d\varphi \cos m\varphi \sin\gamma j_0\left(\frac{Dq\sqrt{(1-x_1^2)(1-x_2^2)}}{\sin\gamma} \sin\varphi\right) \\ &= \int_0^\pi d\varphi \cos m\varphi \sin\gamma. \end{aligned} \tag{4.B.9}$$

Harmonic expansion coefficients in laboratory frame, which enter the pole analysis, can be then easily calculated via

$$c_{l_1 l_2 l}(q) = (4\pi)^{1/2} \sum_{m=-l}^{l} \begin{pmatrix} l_1 & l_2 & l \\ m & \underline{m} & 0 \end{pmatrix} c_{l_1 l_2 m}(q). \tag{4.B.10}$$

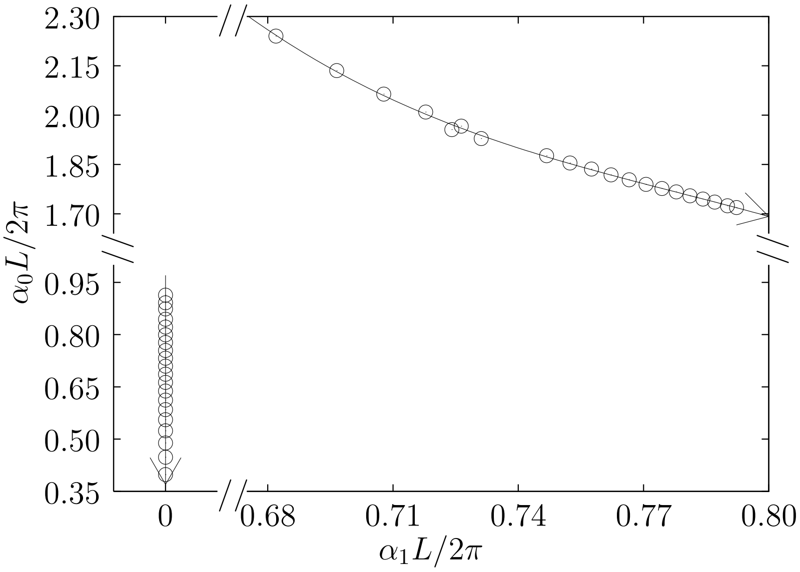

Figure 4.8: The imaginary (α_0) and real (α_1) parts of the lowest-lying conjugate poles $q = \pm\alpha_1 + i\alpha_0$ for the spherocylinders in Onsager approximation. Density ranges from $0.15 \leqslant \rho_{Ons} \leqslant 3.10$ which covers the whole isotropic part of the phase diagram. The arrows denote the direction in which the density is increased.

The expression (4.B.7) shows that in Onsager limit any solution of equation (4.18) scales exactly as $1/L$ which was conjectured in section 4.4, and which is not surprising as this is the only relevant length scale in the system.

Figure 4.8 shows the two lowest lying poles of the isotropic phase for varying density. The figure 4.8 suggests that the asymptotic decay of the pair correlation function is monotonic for all densities in the isotropic phase. It illustrates that the introduction of orientational degrees of freedom can result in monotonic asymptotic decay. However no leading monotonic poles were found in the previous sections for finite L/D ratios. This suggests that there must be a crossover at L/D ratios larger then studied there. The study of the Parsons-Lee ansätz using a procedure as described here should be able to answer this question.

5

Phase behavior of a suspension of colloidal hard rods and non-adsorbing polymer

We study the phase behavior of a mixture of colloidal hard rods with a length-to-diameter ratio of $L/\sigma_c = 5$ and non-adsorbing ideal polymer. We map our binary mixture onto an effective one-component system by integrating out the degrees of freedom of the polymer coils. We derive a formal expression for the exact effective Hamiltonian of the colloidal rods, i.e., it includes all effective many-body interactions and it is related to the exact free volume available for the polymer. We determine numerically on a grid the free volume available for the ideal polymer coils "on the fly" for each colloidal rod configuration during our Monte-Carlo simulations. This allows us to go beyond first-order perturbation theory, which employs the pure hard-rod system as reference state. We perform free energy calculations for the isotropic, nematic, smectic, and crystal phase using thermodynamic integration. We use common tangent constructions at fixed polymer fugacities to map out the phase diagram. We determine the phase behavior for size ratios $q = \sigma_p/\sigma_c = 0.15$, 0.5, and 1, where σ_p is the diameter of the polymer coils. We compare the phase diagrams based on the full effective Hamiltonian with those obtained from first-order perturbation theory, from simulations using the effective pair potential approximation to the effective Hamiltonian and with those based on an empiric effective depletion potential for the rods. We find that the many-body character of the effective interactions stabilizes the nematic and smectic phase for large q, while the effective pair potential description overestimates the attractive interactions and favors, hence, a broad isotropic-crystal coexistence.

5.1 Introduction

The addition of non-adsorbing polymer to a suspension of colloidal rods can be used to purify the rods [94] or to modify the effective interactions between the rodlike particles [95]. The presence of polymer leads to an effective attraction between the rods due to the so-called depletion effect [96]. The range of this attraction is equal to the radius of gyration of the polymer coils and the strength of the attraction is proportional to the fugacity of the polymers [96, 97].

For spherical colloids, a particularly simple model for colloid-polymer mixtures was proposed by Vrij [97], which is often referred to as the Asakura-Oosawa-Vrij (AO) model. In this model, the colloids are modeled as hard spheres with diameter σ_c, while the polymer coils with diameter σ_p are assumed to be ideal and non-interacting. Moreover, the polymer coils are excluded by a center-of-mass distance of $(\sigma_c + \sigma_p)/2$ from the colloids. In this simple model colloid-polymer mixture, Vrij showed the existence of a spinodal instability. Moreover, the effective two-body or Asakura-Oosawa depletion potential can be calculated analytically for this highly idealized model. Gast *et al.* calculated phase diagrams using this effective pair potential in first-order thermodynamic perturbation theory and employing the hard-sphere system as a reference state [98]. They found that the addition of polymer can give broad fluid-solid coexistence regions, but also stable fluid-fluid and colloidal gas-liquid-solid coexistence, for sufficiently large polymer coils. Similar phase diagrams were determined by Lekkerkerker *et al.* using the so-called free-volume approach [99] and by Meijer and Frenkel using computer simulations with lattice polymers [100, 101]. Recently, another approach was followed in Ref. [102–106], which is based on a mapping of the binary mixture onto an effective one-component system. A formal expression for the effective colloid Hamiltonian can be derived by integrating out formally the degrees of freedom of the polymer coils in the partition function [105–107]. This effective Hamiltonian consists of zero-body, one-body, two-body, and higher-body terms, where the two-body (pairwise-additive) term is precisely that given by the Asakura-Oosawa depletion potential. For size ratios $q < 2/\sqrt{3} - 1 = 0.1547$, three- and higher-body terms are zero and the mapping onto an effective Hamiltonian truncated at the effective pair-potential level is exact. Full phase diagrams using the two-body (Asakura-Oosawa pair potential) approximation to this effective Hamiltonian were determined by computer simulations [108]. For higher size ratios, however, three- and higher-body effective interactions are not necessarily small. We therefore developed an efficient Monte-Carlo simulation scheme for the AO model, based on the exact or full effective colloid Hamiltonian, i.e., it includes all the effective many-body interactions [105, 106]. Employing this scheme, we are able to study the full phase diagram and we found that the effective many-body interactions can significantly alter the phase behavior of colloid-polymer mixtures. In conclusion, the AO model is well-studied and well-understood by now for colloidal hard spheres. This should be contrasted to the case of non-spherical particles.

The effect of non-adsorbing polymer on the isotropic-nematic transition of rod-like colloids was investigated by Lekkerkerker *et al.* [109, 110] using perturbation theory. The free volume accessible to the polymers was calculated using scaled particle theory. Simulations of mixtures of colloidal hard rods with polymer are, however, less advanced. Approximate phase diagrams are determined for hard spherocylinders and ideal polymer using thermodynamic perturbation theory and measuring the free volume available for the polymer in a pure hard-spherocylinder system in simulations [110]. The isotropic-isotropic coexistence was, however, determined by performing Gibbs ensemble simulations of the true binary colloidal rod-polymer mixture [110]. As there is no general expression for the effective polymer-mediated pair potential for two rods with arbitrary orientations and positions, Bolhuis *et al.* used a generalized square-well potential to draw some qualitative conclusions on the phase behavior of short-ranged attractive rods [110]. The crystal phase was, however, not included in this study.

In the present chapter, we describe simulations of mixtures of colloidal hard rods and ideal polymer using the exact effective one-component Hamiltonian, i.e., it includes all the effective many-body interactions. We therefore extended our Monte-Carlo simulation scheme [105, 106] for the effective colloid Hamiltonian to rodlike particles. Employing this scheme, we are able to study the full phase diagram for arbitrary values of q. We compare our simulation results with those obtained from thermodynamic perturbation theory using the hard-spherocylinder system as reference state. In addition, we compare the phase diagrams with those obtained from simulations using the effective pair potential approximation to the effective Hamiltonian. This allows us to estimate the significance of the effective many-body interactions. We also propose a new two-parameter effective pair potential to approximate the volume of two overlapping depletion zones.

This chapter is organized as follows. In Sec. 5.2, we describe the model and present an explicit expression for the effective one-component Hamiltonian by integrating out the degrees of freedom of the polymer coils in the partition function. We also introduce the two-parameter effective pair potential to approximate the depletion pair potential, i.e., the volume of two overlapping depletion zones. In Sec. 5.3 we describe the simulation scheme based on the exact or full effective colloid Hamiltonian, and in Sec. 5.4 we present phase diagrams based on i) the exact effective Hamiltonian, ii) the exact effective Hamiltonian but using first-order perturbation theory, iii) the effective pair potential approximation to the effective Hamiltonian and iv) an empiric effective depletion potential for the rods. We end with some concluding remarks.

5.2 Model

5.2.1 Effective Hamiltonian

A simple model for a mixture of sterically-stabilised colloidal particles and non-adsorbing polymer is the so-called Asakura-Oosawa-Vrij (AO) model [96, 97]. In this model, the colloids are treated as hard particles, while the non-interacting polymer coils are treated as point particles, which are excluded from the surface of the colloids by a distance equal to the radius of gyration of the polymer R_g. The diameter of the polymer coils is $\sigma_p = 2R_g$. The colloids are represented by hard spherocylinders, which consist of cylinders of diameter σ_c and length L with semi-spherical caps at both ends with diameter σ_c. The pair potentials in this model are given by:

$$\begin{aligned}\phi_{cc}(\mathbf{R}_{ij};\hat{\omega}_i,\hat{\omega}_j) &= \begin{cases}\infty & \text{for } d_m(\mathbf{R}_{ij};\hat{\omega}_i,\hat{\omega}_j)<\sigma_c\\ 0 & \text{otherwise}\end{cases}\\ \phi_{cp}(\mathbf{R}_i-\mathbf{r}_j;\hat{\omega}_i) &= \begin{cases}\infty & \text{for } d_m(\mathbf{R}_i-\mathbf{r}_j;\hat{\omega}_i)<\sigma_{cp}/2\\ 0 & \text{otherwise}\end{cases}\\ \phi_{pp}(r_{ij}) &= 0,\end{aligned}$$

where $\sigma_{cp} = \sigma_c + \sigma_p$, $\mathbf{R}_{ij} = \mathbf{R}_i - \mathbf{R}_j$ with $\mathbf{R}_i$ and $\mathbf{R}_j$ the center-of-masses of the spherocylinders and $d_m(\mathbf{R}_{ij};\hat{\omega}_i,\hat{\omega}_j)$ denotes the minimum distance between the central axes of the two spherocylinders with orientations $\hat{\omega}_i$ and $\hat{\omega}_j$, $d_m(\mathbf{R}_i-\mathbf{r}_j;\hat{\omega}_i)$ the minimum distance between the spherocylinder axis and the polymer center-of-mass at $\mathbf{r}_j$ in the case of colloid-polymer interactions, and $r_{ij} = |\mathbf{r}_i - \mathbf{r}_j|$ the distance between the two polymer center-of-masses.

The total Hamiltonian of a mixture of N_c colloidal rods and N_p ideal polymer coils in a volume V and at temperature T reads $H = H_{cc} + H_{cp} + H_{pp}$, where $H_{cc} = \sum_{i<j}^{N_c} \phi_{cc}(\mathbf{R}_{ij};\hat{\omega}_i,\hat{\omega}_j)$, $H_{cp} = \sum_{i=1}^{N_c}\sum_{j=1}^{N_p} \phi_{cp}(\mathbf{R}_i-\mathbf{r}_j;\hat{\omega}_i)$, and $H_{pp} = \sum_{i<j}^{N_p} \phi_{pp}(r_{ij}) = 0$.

In this chapter, we map the rod-polymer mixture with interaction Hamiltonian H onto an effective one-component colloid system interacting with the effective Hamiltonian H^{eff}. Here we briefly sketch the derivation of a formal expression for the effective Hamiltonian for colloidal particles that possess orientational degrees of freedom, obtained by integrating out the degrees of freedom of the polymer coils in the partition function. For more details, we refer the reader to Refs. [102–106].

We fix the number of colloidal rods N_c and the fugacity $z_p = \Lambda_p^{-3}\exp(\beta\mu_p)$ of the polymer coils, where Λ_ν denotes the thermal wavelength of species $\nu = c, p$, μ_p the chemical potential of the reservoir of polymer coils and $\beta = 1/k_BT$ the inverse temperature. The thermodynamic potential $F(N_c, V, z_p, T)$ of this system can be written as

$$\exp[-\beta F] = \frac{1}{N_c!\Lambda_c^{3N_c}}\text{Tr}_c \exp[-\beta H^{\text{eff}}], \tag{5.1}$$

where $H^{\text{eff}} = H_{cc} + \Omega$ and the trace Tr_c is short for the integrals over the coordinates and the orientations of the rods $\int_V d\mathbf{R}^{N_c} \int d\hat{\omega}^{N_c}$. Because of the ideal character of the polymer-polymer interactions in the AO model, $\beta\Omega$ simplifies to

$$-\beta\Omega = z_p \int_V d\mathbf{r} \exp[-\beta \sum_{i=1}^{N_c} \phi_{cp}(\mathbf{R}_i - \mathbf{r};\hat{\omega}_i)] = z_p V_f, \tag{5.2}$$

where $V_f = V_f(\{\mathbf{R};\hat{\omega}\};z_p)$ is the volume available for polymer, which depends on the static configuration of N_c colloidal rods with positions $\{\mathbf{R}_i\}$ and orientations $\{\hat{\omega}_i\}; i = 1, 2, \ldots N_c$. Non-vanishing contributions to V_f stem from those positions $\mathbf{r}$ that are outside any of the N_c depletion zones. Once V_f, and thus H^{eff}, are known for each colloidal rod configuration, the thermodynamics and the phase behavior of the mixture can be determined. We first show that V_f, and hence, the polymer-induced colloid interactions Ω can be split into zero-body, one-body, two-body, etc. contributions. To this end, we expand V_f in terms of the colloid-polymer Mayer-function $f(\mathbf{R}_i - \mathbf{r};\hat{\omega}_i)$, which for the present model equals -1 for $0 < d_m(\mathbf{R}_i - \mathbf{r}; \hat{\omega}_i) < \sigma_{cp}/2$, and 0 otherwise, with $d_m(\mathbf{R}_i - \mathbf{r}; \hat{\omega}_i)$ the minimum distance between the spherocylinder axis and position $\mathbf{r}$. We arrive at

$$\begin{aligned} V_f = \int d\mathbf{r} \prod_i^{N_c} [1 + f(\mathbf{R}_i - \mathbf{r}; \hat{\omega}_i)] = V_f^{(0)} + \sum_i^{N_c} V_f^{(1)}(\mathbf{R}_i; \hat{\omega}_i) + \\ + \sum_{i<j}^{N_c} V_f^{(2)}(\mathbf{R}_i, \mathbf{R}_j; \hat{\omega}_i, \hat{\omega}_j) + \dots \\ + \sum_{i_1<\ldots<i_k}^{N_c} V_f^{(k)}(\mathbf{R}_{i_1}, \dots, \mathbf{R}_{i_k}; \hat{\omega}_{i_1}, \dots, \hat{\omega}_{i_k}) + \dots, \end{aligned} \tag{5.3}$$

where the zero-body contribution $V_f^{(0)}$ is equal to the volume of the system V. For $k \geqslant 1$, we find

$$V_f^{(k)} = \int d\mathbf{r} \prod_{m=1}^{k} f(\mathbf{R}_{i_m} - \mathbf{r}; \hat{\omega}_{i_m}). \tag{5.4}$$

The one-body contribution can be interpreted as the volume that is excluded for a polymer coil by a single rod. The two-body term is the overlap volume of two depletion zones of two colloidal rods. Introducing $n = n(\mathbf{r}) \equiv -\sum_{i=1}^{N_c} f(\mathbf{R}_i - \mathbf{r}; \hat{\omega}_i)$, the number of simultaneously overlapping depletion layers in $\mathbf{r}$, one finds the identity

$$\sum_{i_1<\ldots<i_k}^{N_c} V_f^{(k)}(\mathbf{R}_{i_1}, \dots, \mathbf{R}_{i_k}) = (-1)^k \int_{n \geq k} d\mathbf{r} \frac{n(\mathbf{r})!}{(n(\mathbf{r}) - k)!k!}. \tag{5.5}$$

All $k' \geq k$ terms in Eq. (5.3) can be summed to obtain (for the present Mayer function only)

$$\begin{aligned} V_f^{(k+)} &= \sum_{k' \geqslant k} \left[\sum_{i_1<\ldots<i_{k'}}^{N_c} V_f^{(k')}(\mathbf{R}_{i_1}, \dots, \mathbf{R}_{i_{k'}}; \hat{\omega}_{i_1}, \dots, \hat{\omega}_{i_{k'}}) \right] \\ &= \frac{(-)^k}{(k-1)!} \int_{n \geq k} d\mathbf{r} \prod_{i=1}^{k-1} (n(\mathbf{r}) - i). \end{aligned} \tag{5.6}$$

The terms $V_f^{(0)}$, $V_f^{(1)}$ are irrelevant offsets that do not influence the thermodynamic properties of the bulk mixture [104]. Setting $V_f^{(3+)}$ equal to zero, the pairwise additivity approximation is recovered.

5.2.2 Effective pair potential description

In the case of spherical colloids, it can be shown explicitly that for sufficiently small polymer coils, the three-body and higher-body terms are identically zero, and that the mapping onto an effective Hamiltonian truncated at the effective pair-potential level is exact. Hence, the pairwise additivity approximation to the effective Hamiltonian, i.e., $V_f^{(3+)} = 0$, proves to be a reasonable approximation to predict the phase behavior of the AO model for polymer coils that are small compared to the size of the colloids. For spherical colloids, the effective pair-potential is given by the Asakura-Oosawa depletion potential [96], which is known analytically, while $V_f^{(3+)}$ can only be evaluated numerically [106]. In the case of colloidal rods, the overlap volume of two infinitely long cylindrical depletion zones can be calculated exactly [111, 112]. However, no analytic expression exists for the overlap volume of two depletion zones of finite spherocylinders with arbitrary orientations and positions and, hence, $V_f^{(2)}$ can only be calculated numerically. The numerical evaluation of $V_f^{(2)}$ is almost as expensive as $V_f^{(2+)}$, that includes all the effective many-body interactions. It is therefore useful to have a good model pair potential that is mathematically simple and fits reasonably well the exact overlap volume of two depletion zones. Bolhuis *et al.* [110] approached this problem by using a generalized square-well potential, which provides qualitatively correct phase diagrams, when the size of the polymer is small compared to the diameter of the rods. It lacks, however, quantitative agreement with the exact overlap volume of the depletion zones of two spherocylinders, thereby overestimating significantly the attraction (especially at larger distances).

Here we propose a two-parameter pairwise additive depletion potential $\beta\phi_{dep}(\mathbf{R}_{ij}, \hat{\omega}_i, \hat{\omega}_i)$ to approximate the exact overlap volume of the depletion zones of two spherocylinders $V_{overlap}(\mathbf{R}_{ij}, \hat{\omega}_i, \hat{\omega}_j)$, and hence $\beta\phi_{dep}(\mathbf{R}_{ij}, \hat{\omega}_i, \hat{\omega}_i) \simeq -z_p V_f^{(2)} = -z_p V_{overlap}(\mathbf{R}_{ij}, \hat{\omega}_i, \hat{\omega}_j)$. We start with the assumption that the overlap volume of the depletion zones can be fitted by the overlap of two axially symmetric anisotropic Gaussian functions. The overlap integral of two Gaussian distributions can be calculated exactly to give [91]

$$\phi_{dep}(\mathbf{R}_{ij}, \hat{\omega}_i, \hat{\omega}_j) = \varepsilon(\hat{\omega}_i, \hat{\omega}_j) e^{-R_{ij}^2/\sigma(\hat{\mathbf{R}}_{ij}, \hat{\omega}_i, \hat{\omega}_j)^2} \tag{5.7}$$

where $\hat{\mathbf{R}}_{ij}$ is the unit vector in the direction of the center-of-mass distance of two rods, $R_{ij} \equiv |\mathbf{R}_i - \mathbf{R}_j|$, $\varepsilon(\hat{\omega}_i, \hat{\omega}_j)$ is the angle-dependent strength parameter given by $\varepsilon(\hat{\omega}_i, \hat{\omega}_j) = \varepsilon_0(1-\chi^2(\hat{\omega}_i \cdot \hat{\omega}_j)^2)^{-1/2}$, with the parameter χ determined by the anisotropy of the particles, and $\sigma(\hat{\mathbf{R}}_{ij}, \hat{\omega}_i, \hat{\omega}_j)$ is the angle-dependent range parameter. Various modifications of these single site potentials with angle-dependent strength and range parameters exist [113–115] tailored to fit the wide range of anisotropic interactions.

Here we construct a modified single-site potential that fits reasonably well the exact overlap volume of the depletion zones. The first modification is to replace the center-to-center distance R_{ij} in (5.7) to the minimum distance $x = d_m(\mathbf{R}_{ij}; \hat{\omega}_i, \hat{\omega}_j)/\sigma_{cp}$ between the spherocylinder axes together with a replacement of the angle-dependent range parameter $\sigma(\hat{\mathbf{R}}_{ij}; \hat{\omega}_i, \hat{\omega}_j)$ by simply the isotropic interaction range σ_{cp}, such that the range of the potential at the minimum distance is independent of the orientation. The second modification is to replace the Gaussian potential in Eq. (5.7) by a more realistic expression. The first option is to use the volume excluded by two spheres, which fits accurately the interaction of perpendicular cylinders, or parallel ellipsoids. Moreover this choice is convenient for an extrapolation from hard rods to hard spheres using a Parsons approach. As this chapter is focused on the liquid crystalline behavior of elongated rods, we use here the overlap volume of two parallel cylinders with diameter σ_{cp} per unit length at a minimum distance x

$$f(x) = \frac{\sigma_{cp}^2}{2}\left[\arccos(x) - x\sqrt{1-x^2}\right]. \tag{5.8}$$

In addition, we define a new strength parameter, which is a function of $\hat{\omega}_i$ and $\hat{\omega}_j$ as well as on $\mathbf{R}_{ij}$. To this end, we replace the anisotropy parameter χ in $\varepsilon(\mathbf{R}_{ij}; \hat{\omega}_i, \hat{\omega}_j)$ by an angle-and distance-dependent anisotropy parameter $\chi(\mathbf{R}_{ij};\hat{\omega}_i,\hat{\omega}_j)$, which is used to ensure that the overlap volume remains constant when two non-parallel cylinders slide along each other, and changes when two nearly parallel rods shift along each other. To achieve this, we introduce the concept of interaction length, which can be interpreted as the length of the spherocylinder that is felt by the other spherocylinder. We illustrate this in Fig. 5.1. This length is defined as the length of that part of the central axis of the spherocylinder for which there are points on the axis of the other spherocylinder within a distance σ_{cp}, i.e., that part of the cylinder that lies within the other spherocylinder with a length-to-diameter ratio $L/2\sigma_{cp}$. The anisotropy parameter is now based not on the actual length and diameter of the spherocylinder, but rather on the interaction length of the two spherocylinders, say λ and μ. For large polymer diameters, however, it is possible that when two aligned spherocylinders shift along each other, they still feel each other by the full length of the cylinder axis even for considerable shifts. We correct this by the following constraint. We take the shortest distance from the two endpoints of one spherocylinder axis to the other spherocylinder axis. This yields two points on the central axis of the other spherocylinder (or an extension thereof). Our second constraint is that the interaction length lies between these two points.

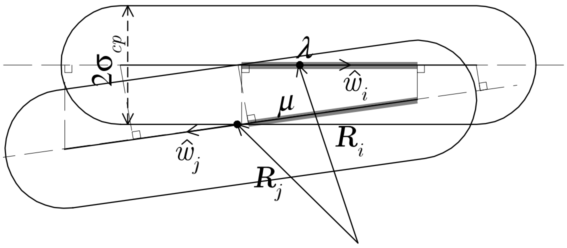

Figure 5.1: A schematic sketch of the interaction lengths for two spherocylinders with a length-to-diameter ratio L/σ_c and non-adsorbing polymer coils with diameter σ_p. The positions and the orientations of the spherocylinders are denoted by $\mathbf{R}_i$, $\mathbf{R}_j$, $\hat{\omega}_i$, and $\hat{\omega}_j$. The interaction length is defined as the length of that part of the cylinder axis of the spherocylinder for which there are points on the axis of the other spherocylinder within a distance σ_{cp}. Moreover, the interaction length should also satisfy a second constraint, which can be determined as follows: Take the shortest distance from the two endpoints of one spherocylinder axis to the other spherocylinder axis. This yields two points on the central axis of the other spherocylinder (or an extension thereof). The interaction length should lie in between these two points. The interaction lengths μ and λ are denoted by the thick lines.

The anisotropy parameter for two identical ellipsoids was calculated by Berne [91]. Here, we use a simple multiplication of the square root of the anisotropy parameter of an ellipsoid with major and minor axis $\lambda + \sigma_{cp}$ and σ_{cp} times the square root of the anisotropy parameter of an ellipsoid with major and minor axis $\mu + \sigma_{cp}$ and σ_{cp}.

$$\chi(\mathbf{R}_{ij};\hat{\omega}_i,\hat{\omega}_j) = \chi^2(\lambda,\mu) = \frac{(\xi\lambda+\sigma_{cp})^2-(\sigma_{cp})^2}{(\xi\lambda+\sigma_{cp})^2+(\sigma_{cp})^2} \times \frac{(\xi\mu+\sigma_{cp})^2-(\sigma_{cp})^2}{(\xi\mu+\sigma_{cp})^2+(\sigma_{cp})^2}. \tag{5.9}$$

Moreover, we introduce the fitting parameter ξ to correct for the difference in overlap volumes of ellipsoids and of spherocylinders. This anisotropy parameter yields the correct results for identical rods and vanishes in the case when only the spherocylinder cap interacts with the cylinder, i.e., when μ or λ equals zero.

q	$\varepsilon_0/2$	ξ
0.15	0.277089	4.14477
0.50	0.546528	2.74785
1.00	0.875059	2.29393

Table 5.1: The values of the fitting parameters ε_0 and ξ of the two-parameter depletion potential for a system of colloidal hard rods with a length-to-diameter ratio $L/\sigma_c = 5$ and non-adsorbing polymer coils with diameter σ_p and varying diameter ratios $q = \sigma_p/\sigma_c$.

Finally, our modified two-parameter depletion pair potential that approximates the exact overlap volume of two depletion zones reads

$$\phi_{dep}(\mathbf{R}_{ij}, \hat{\omega}_i, \hat{\omega}_j) = \frac{\varepsilon_0 \sigma_{cp}^2}{2} \frac{\arccos(x) - x\sqrt{1-x^2}}{\sqrt{1-\chi^2(\lambda,\mu)(\hat{\omega}_i \cdot \hat{\omega}_j)^2}} \tag{5.10}$$

with $\chi^2(\lambda, \mu)$ given by (5.9). The two fitting parameters ε_0 and ξ can be determined independently from each other. To this end, we employed a fit of $\int dr r \exp(z_p V_{overlap}) = \int dr r \exp(-\beta\phi_{dep})$ for a pair of spherocylinders that are perpendicular to each other and for two spherocylinders that are parallel. The exact overlap volume of two depletion zones $V_{overlap}$ can be calculated analytically in a few cases or otherwise numerically. We like to stress that for spherocylinders of fixed diameter σ_c and polymer size σ_p, ξ is rather independent of the spherocylinder length L, which justifies the use of the interaction length. Fig. 5.2 shows the good agreement between the exact overlap volume with the two-parameter depletion pair potential (5.10) for a system of colloidal hard rods with $L/\sigma_c = 5$ and non-adsorbing polymer coils with diameter σ_p and $q = \sigma_p/\sigma_c = 0.5$. The values of the fitting parameters are displayed in Table 5.1 for the size ratios employed in this work.

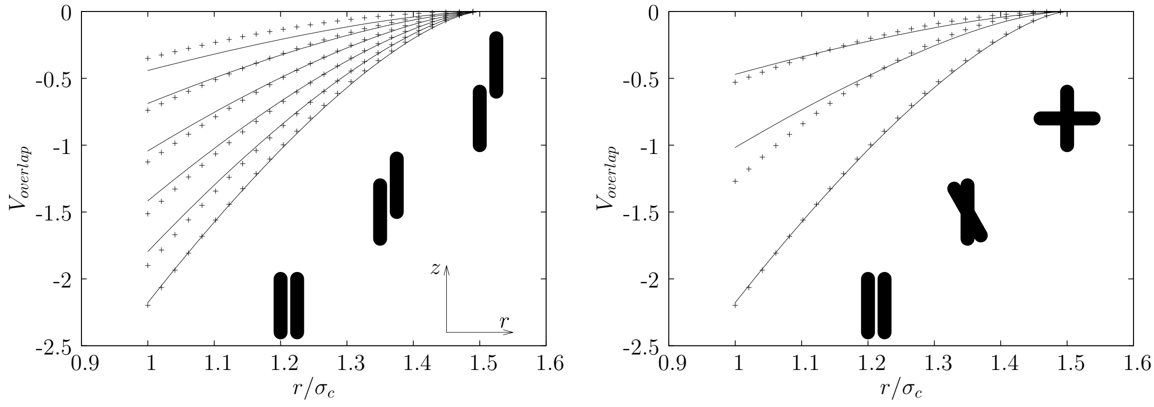

Figure 5.2: The negative of the exact overlap volume of two depletion zones $-V_{overlap}$ (plusses) and the approximate effective pair potential (solid lines) for two spherocylinders with $L/\sigma_c = 5$, and $\sigma_p/\sigma_c = 0.5$ as a function of a center-of-mass displacement in the r-direction. a) Parallel spherocylinders oriented in the $z-$direction for a fixed shift of the center-of-mass of the second spherocylinder in the $z-$direction. The curves from bottom to top denote a shift of $z/\sigma_c = 0, 1, 2, 3, 4, 5$. b) Two spherocylinders with zero z-shift, the second one rotated about the line through the center-of-masses by $\theta = 0, \arccos(12/13), \pi/2$ from bottom to top.

5.3 Simulations

In section 5.2 we derived the effective Hamiltonian of the colloids by integrating out the degrees of freedom of the polymer coils in the partition function. The key quantity in the effective Hamiltonian is the available volume V_f for the polymer coils which depends on the instantaneous colloid positions $\{\mathbf{R}_i\}$ and orientations $\{\hat{\omega}_i\}$. We calculate V_f numerically on a smart grid, which allows us to employ the full effective Hamiltonian or to employ the pairwise additivity assumption for the effective Hamiltonian by setting $V_f^{(3+)} = 0$. As already noted in Refs. [105, 106], the standard Metropolis algorithm in Monte Carlo simulations is based on the acceptance probability $\min(1, \exp[-\beta \Delta H^{\text{eff}}])$, with ΔH^{eff} the change of H^{eff} due to a displacement of a single colloidal rod at position $\mathbf{R}_1 \to \mathbf{R}_1'$ with orientation $\hat{\omega}_1 \to \hat{\omega}_1'$. The only contributions to ΔV_f and hence to ΔH^{eff} occurs inside the two spherocylinders with length-to-diameter ratio L/σ_{cp} centered about $\mathbf{R}_1$ with orientation $\hat{\omega}_1$ and about $\mathbf{R}_1'$ with orientation $\hat{\omega}_1'$. We mesh these two spherocylinders by a uniform grid with typically $0.8 - 1.8 \times 10^6$ gridpoints. It is convenient to use the coordinate frame of the spherocylinder, in which the central axis of the spherocylinder coincides with the z-axis. Subsequently, all the other spherocylinders whose depletion zones overlap with the depletion zone of this spherocylinder, are transformed to this coordinate frame. We also correct for the gridpoints that belong to both grids of the spherocylinders.

We performed NVT Monte Carlo simulations of the isotropic and nematic phase using 762 particles in a cubic box. For the smectic and crystal phase, we employed 462 and 240 particles, respectively. In addition, we allowed for box shape fluctuations during our simulations of the smectic and crystal phase, while the total volume of the system was kept fixed. Equilibration is checked by monitoring the free volume accessible for the polymers. In order to determine the phase diagram of the effective one-component system, we first calculate the thermodynamic potential F, defined in Eq. (5.1), as a function of N_c, V, z_p. The polymer fugacity z_p is related to the reservoir packing fraction $\eta_p^r \equiv \pi \sigma_p^3 z_p / 6$. We use thermodynamic integration to relate the free energy $F(\eta_c, z_p)$ of the effective system to that of a reference system of pure hard rods at the same colloidal rod packing fraction $\eta_c \equiv \pi \sigma_c^3 N_c / 6V$.

$$\beta F(\eta_c, z_p) = \beta F(\eta_c, 0) - \int_0^{z_p} dz_p' \langle V_f(z_p') \rangle. \tag{5.11}$$

The free energies for the reference system of pure hard spherocylinders are determined from the equation-of-state data obtained from simulations of Ref. [18]. The thermodynamic integration is based on typically $20 - 30$ points in the (η_c, z_p) plane for each phase. Once the free energies are known for each phase as a function of η_c and z_p, we can determine the densities of the coexisting phases by equating the pressures and chemical potentials in both phases.

5.4 Results and discussion

The procedure described above was used to determine the phase behavior of mixtures consisting of colloidal hard rods with a length-to-diameter ratio $L/\sigma_c = 5$ and non-adsorbing polymer coils with a radius-of-gyration $R_g = \sigma_p/2$. We mapped out the phase diagram for diameter ratios $q = \sigma_p/\sigma_c = 0.15, 0.5$, and 1. Fig. 5.3 shows the phase diagrams for

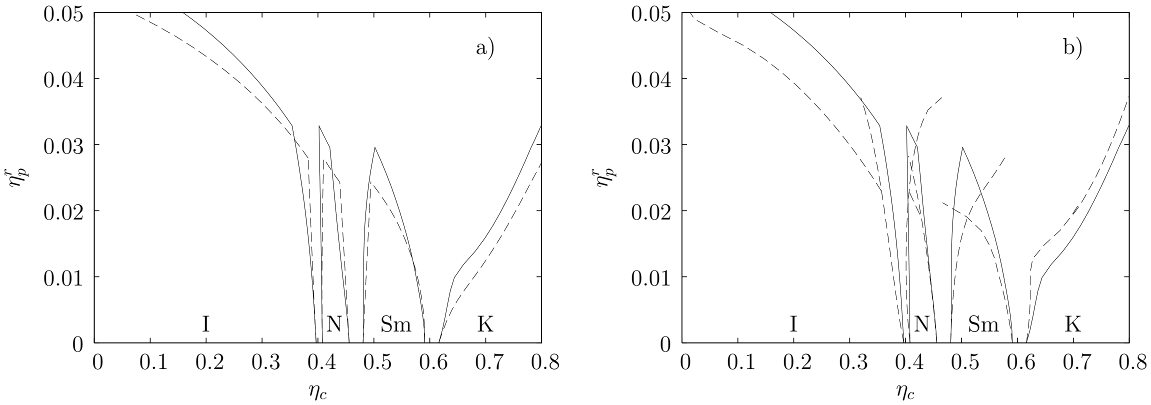

Figure 5.3: Phase diagrams for a mixture of hard spherocylinders with $L/\sigma_c = 5$ and non-adsorbing polymer coils with a diameter σ_p. The size ratio $q = \sigma_p/\sigma_c = 0.15$. a) phase diagram based on the full effective Hamiltonian, i.e., including all effective many-body interactions, thermodynamic integration —, first-order perturbation theory, $- - -$, and b) phase diagram based on the effective pair potential approximation to the effective Hamiltonian, i.e., $V_f^{(3+)} = 0$ —, and using the two-parameter effective depletion potential (5.10) $--$.

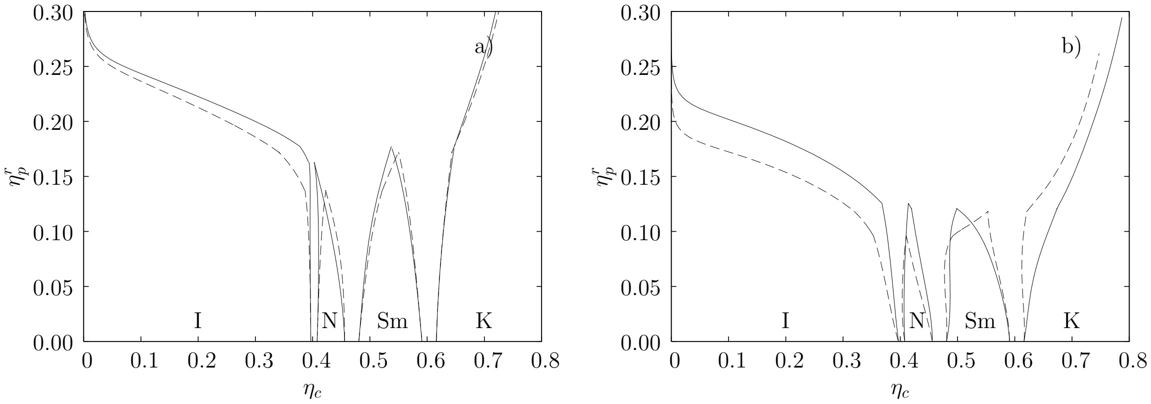

Figure 5.4: Same as in Fig. 5.3, but for $q = 0.5$.

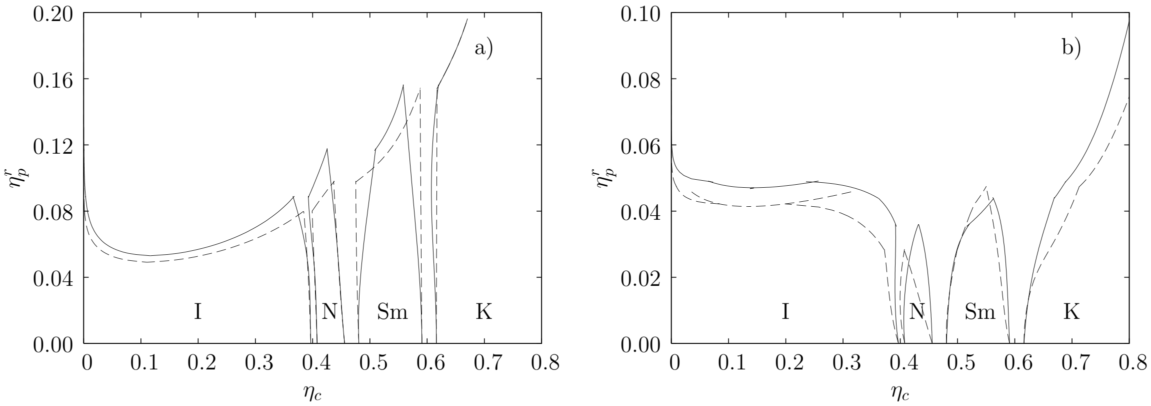

Figure 5.5: Same as in Fig. 5.3, but for $q = 1$.

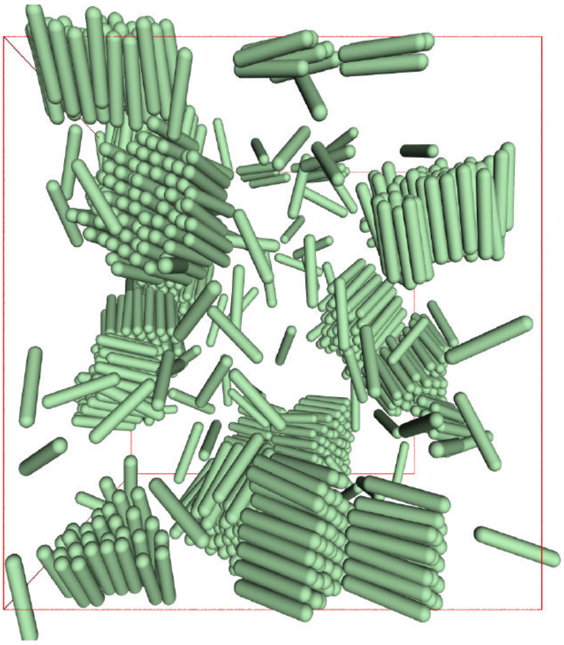

Figure 5.6: Typical configuration of a mixture of colloidal hard rods with $L/\sigma_c = 5$ and non-adsorbing polymer (not visible) with $q = 0.5$ well inside the broad isotropic-crystal coexistence region at a colloidal rod packing fraction $\eta_c = 0.0884$ and a polymer reservoir packing fraction $\eta_p^r = 1.83$.

$q = 0.15$ in the (η_c, η_p^r) plane. In Fig. 5.3a, we present the resulting phase diagram based on the full effective many-body Hamiltonian. The binodals are shown by the solid lines. In this representation, the tielines connecting coexisting state points are horizontal. The phase diagrams show thermodynamically stable regions of the isotropic (I), nematic (N), smectic-A (Sm) and crystalline (K) phases. At $\eta_p^r = 0$, we recover the I-N, N-Sm, Sm-K transition of the pure hard-rod system. Increasing η_p^r, we observe an enormous broadening of the Sm-K coexistence region, while the I-N and N-Sm coexistence region broadens only slightly. We also find that the smectic phase becomes metastable with respect to the nematic phase for η_p^r higher than the N-Sm-K triple point, resulting in a broad N-K coexistence region. At slightly higher η_p^r, the phase diagram shows a I-N-K triple point and a I-K coexistence, which widens upon increasing η_p^r. For comparison, we also plot the phase diagram based on first-order perturbation theory (dashed lines), where we assume that the available free volume for the polymer does not depend on the polymer fugacity, i.e., we set $V_f(\eta_c, z_p) = V_f(\eta_c, 0)$. Note that the phase diagrams presented in Ref. [110] are also based on first order perturbation theory. We observe that in first-order perturbation theory all the binodals and triple points are slightly shifted to lower polymer reservoir packing fractions compared to the exact phase diagrams. For this size ratio the mapping of the binary mixture onto an effective one-component system with only effective pair potentials, i.e., $V_f^{(3+)} = 0$, is exact. In Fig. 5.3b, we compare the phase diagram based on the effective pair potential description to the effective Hamiltonian (solid lines) with the one based on the two-parameter effective depletion potential (5.10) (dashed lines). Fig. 5.3b shows that employing the effective depletion potential yields a shift of the binodals to lower polymer reservoir packing fractions, but the overall agreement is reasonable.

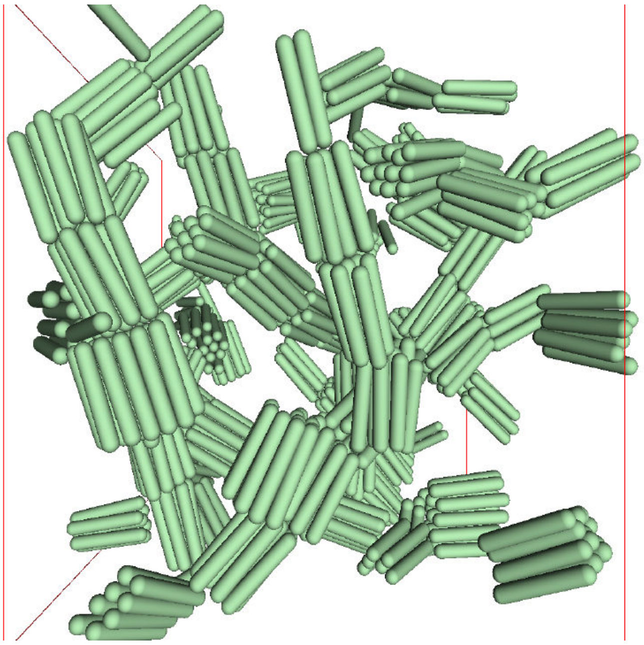

Figure 5.7: Same as Fig. 5.6, but at $\eta_p^r = 2.09$.

In Fig. 5.4, we present the phase diagrams for $q = 0.5$. We now observe a broadening of both the N-Sm and the Sm-K coexistence region upon increasing η_p^r. At sufficiently high η_p^r, a I-N-Sm triple point and subsequently, a broad I-Sm coexistence region appears. At slightly higher η_p^r, we find a I-Sm-K triple point and a broad I-K coexistence region, which widens even further upon increasing η_p^r. The first-order perturbation theory (dashed lines) results again in a shift of all binodals towards lower polymer reservoir packing fractions. For $q = 0.5$, the effective three- and higher-body many-body interactions are not identical to zero and Fig. 5.4b shows the phase diagram based on the effective pair potential approximation to the effective Hamiltonian (solid lines), i.e., $V_f^{(3+)} = 0$. We find that neglecting the effective many-body interactions results in a shift of the broad I-K coexistence region to lower η_p^r, and it widens the I-N coexistence region. Fig. 5.4b also shows the phase diagram based on the two-parameter effective depletion potential (5.10) (dashed lines). Again, we find that employing the effective depletion potentials results in a shift of the binodals to lower polymer reservoir packing fractions.

In Fig. 5.5, we present the phase diagrams for $q = 1$. We now observe a slight widening of the N-Sm and the Sm-K coexistence region upon increasing η_p^r. Moreover, we find at sufficiently high η_p^r, a I-I coexistence region ending in a critical point. For polymer packing fraction higher than the critical point a phase separation occurs in an isotropic ”gas” phase which is dilute in colloidal rods and an isotropic ”liquid” phase which is dense in rods. Upon increasing η_p^r, a I-I-N triple point is found and the ”liquid” phase becomes metastable with respect to the nematic phase. A broad I-N coexistence region is observed for η_p^r higher than the I-I-N triple point. Upon increasing η_p^r, we observe successively an I-N-Sm triple point, a broad I-Sm coexistence, a I-Sm-K triple point and finally, a broad I-K coexistence region. First-order perturbation theory (dashed lines) shows an overall shift of all binodals, triple points, and the critical point towards lower polymer reservoir packing fractions. Fig. 5.4b shows the phase diagram based on the effective pair potential approximation to the effective Hamiltonian (solid line). We find that the main effect of the many-body interactions is that the I-I demixing transition is enhanced and that the binodals are shifted to higher η_p^r. Moreover, we find that the nematic and smectic phase are stabilized by the many-body interactions, resulting in broad I-N and I-Sm coexistence regions. Fig. 5.4b also shows the phase diagram based on the two-parameter effective depletion potential (5.10) (dashed lines). Again, we find that employing the effective depletion potential results in a shift of the binodals to lower polymer reservoir packing fractions.

In summary, we find that the phase diagram for large polymer coils displays an isotropic ”gas-liquid” phase separation ending in a critical point and a I-I-N triple point. Moreover, the phase diagram shows I-N-Sm and I-Sm-K triple points and broad coexistence of I-N, I-Sm, and I-K phases. For smaller polymer coils, we find that the polymer reservoir packing fractions of the I-N-Sm triple point moves to higher values and consequently, we only find broad I-K coexistence regions. Reducing the polymer coils even further, we observe a I-N-K and a N-Sm-K triple point. The topologies of these phase diagram as a function of q are consistent with the first order perturbation theory calculations in Ref. [110]. In addition, we find that the two-parameter depletion potential yields reasonable agreement with the exact phase diagrams, in particularly at small q. This potential can be used in nucleation studies where the simulations based on the exact effective Hamiltonian is computationally too expensive. Very recent experiments on mixtures of fd virus particles and dextran (non-adsorbing polymer) by Dogic and Fraden showed different kinetic pathways of the formation of the smectic or crystal phase as a function of the exact dextran concentration [4]. At low polymer concentrations, they observe the nucleation of colloidal membranes, that consist of a single layer of rods, which can coalesce laterally. At higher polymer concentrations, the membranes can stack on top of each other to form long thin filaments. Figs. 5.6 and 5.7 show typical configurations of a mixture of colloidal hard rods with $L/\sigma_c = 5$ and non-adsorbing polymer (not visible) with a diameter ratio $q = 0.5$ well inside the broad isotropic-crystal coexistence region at $\eta_c = 0.0884, \eta_p^r = 1.83$ and at $\eta_c = 0.0884, \eta_p^r = 2.09$, respectively. In Fig. 5.6, we find the formation of single membranes, while Fig. 5.7 shows the formation of long filaments. These results are in agreement with these experimental findings. The formation of such filaments was studied theoretically by Frenkel and Schilling [116]. The nucleation of the crystal phase in a fluid of hard rods with $L/\sigma_p = 2$ was investigated in an earlier simulation study [117]. This work shows that in the earliest stages of nucleation, a colloidal crystalline membrane is formed, but nucleation growth is then hampered by the fact that the top and bottom surfaces of this crystallite are preferentially covered by rods that align parallel to the surface; the surface poisons itself [117]. Nucleation studies of longer rods are hampered due to severe equilibration problems. The widening of the biphasic regions due to the presence of non-adsorbing polymer may circumvent the equilibration problems and more detailed nucleation studies of mixtures of colloidal rods with polymer-mediated effective attractions will be future work.

References

[1] F. Reinitzer, Montash. Chem. **9**, 421 (1888).

[2] G. Friedel, Ann. Phys. **18**, 273 (1922).

[3] Z. Dogic and S. Fraden, Langmuir **16**, 7820 (2000).

[4] Z. Dogic and S. Fraden, Phil. Trans. R. Soc. Lond. A **359**, 997 (2001).

[5] R. Best, J. Austral. Inst. Agric. Sci. **5**, 94 (1939).

[6] S. Fraden, G. Maret, D. L. D. Caspar, and R. Meyer, Phys. Rev. Lett. **63**, 2068 (1989).

[7] A. Leadbetter and E. Norris, Mol. Phys. **38**, 669 (1979).

[8] K. R. Purdy, Z. Dogic, S. Fraden, A. Ruhm, L. Lurio, and S. G. J. Mochrie, Phys. Rev. E **67**, 031708 (2003).

[9] L. Onsager, Ann. N.Y. Acad. Sci. **51**, 627 (1949).

[10] J. Straley, Mol. Cryst. Liq. Cryst. **24**, 7 (1973).

[11] D. Frenkel, J. Phys. Chem. **91**, 4912 (1988).

[12] L. Blum and A. Torruella, J. Chem. Phys. **56**, 303 (1972).

[13] C. Gray and K. Gubbins, *Theory of molecular fluids*, volume 1, Oxford University Press, 1984.

[14] N. Metropolis, A. Rosenbluth, M. Rosenbluth, A. Teller, and E. Tel, J. Chem. Phys. **21**, 1087 (1953).

[15] B. J. Alder and T. E. Wainwright, J. Chem. Phys. **31**, 459 (1959).

[16] K. Fichthorn and W. Weinberg, J. Chem. Phys. **95**, 1090 (1991).

[17] M. Allen, G. Evans, D. Frenkel, and B. Mulder, Adv. Chem. Phys **LXXXVI** (1993).

[18] P. Bolhuis and D. Frenkel, J. Chem. Phys. **106**, 666 (1997).

[19] J. M. Polson and D. Frenkel, Phys. Rev. E **56(6)**, R6260 (1997).

[20] J. Perrin, J. Phys. **9**, 5 (1910).

[21] T. Biben, J. Hansen, and J. Barrat, J. Chem. Phys. **98**, 7330 (1993).

[22] R. Piazza, T. Bellini, and V. Degiorgio, Phys. Rev. Lett. **71**, 4267 (1993).

[23] S. Hachisu and K. Tokano, Adv. Colloid. Interface Sci. **16**, 233 (1982).

[24] T. Biben and J. Hansen, J. of Phys.: Condens. Matter **6**, A345 (1994).

[25] G. Téllez and T. Biben, Eur. Phys. J. E **2**, 137 (2000).

[26] R. van Roij, J. of Phys.: Condensed Matter **15**, 53569 (2003).

[27] A.-P. Hynninen, R. van Roij, and M. Dijkstra, Europhys. Lett. **65**, 719 (2004).

[28] A. Philipse and G. Koenderink, Adv. Colloid Interface Sci. **100**, 613 (2003).

[29] M. Rasa and A. Philipse, Nature **429**, 857 (2004).

[30] H. Wensink, *Ph.D. Thesis Utrecht University*, 2004.

[31] H. Wensink and H. Lekkerkerker, Europhys. Lett. **66**, 125 (2004).

[32] M. Schmidt, M. Dijkstra, and J. Hansen, Phys. Rev. Lett. **93**, 088303 (2004).

[33] M. Schmidt, M. Dijkstra, and J. Hansen, J. Phys.: Condens. Matter **16**, S4185 (2004).

[34] T. Biben and J. Hansen, Mol. Phys. **80**, 853 (1993).

[35] T. Odijk, Macromolecules **19**, 2313 (1986).

[36] V. A. Baulin and A. R. Khokhlov, Phys. Rev. E **60**, 2973 (1999).

[37] R. Allen, D. Goulding, and J. Hansen, Phys. Chem. Comm. **7** (1999).

[38] S. McGrother, D. Williamson, and G. Jackson, J. Chem. Phys. **104**, 6755 (1996).

[39] L. D. Landau and E. M. Lifschitz, *Statistical Physics*, Pergamon Press, 1959.

[40] R. van Roij, M. Dijkstra, and R. Evans, Europhys. Lett. **49**, 350 (2000).

[41] R. van Roij, M. Dijkstra, and R. Evans, J. Chem. Phys. **113**, 7689 (2000).

[42] M. Dijkstra, R. van Roij, and R. Evans, Phys. Rev. E **63**, 051703 (2001).

[43] D. Frenkel and B. Smit, *Understanding Molecular Simulations*, Academic Press, 2002.

[44] H. N. W. Lekkerkerker, P. Buining, J. Buitenhuis, G. J. Vroege, and A. Stroobants, NATO ASI series C, Vol. 460, in *'Observation, prediction and simulation of phase transitions in complex fluids'*, Kluwer Academic, Dordrecht, 1995.

[45] S. Fraden, NATO ASI series C, Vol. 460, in *'Observation, prediction and simulation of phase transitions in complex fluids'*, Kluwer Academic, Dordrecht, 1995.

[46] A. Stroobants, H. Lekkerkerker, and D. Frenkel, Phys. Rev. A **36**, 2929 (1987).

[47] J. Veerman and D. Frenkel, Phys. Rev. A **41**, 3237 (1990).

[48] D. Frenkel and B. Mulder, Mol. Phys. **55**, 1171 (1985).

[49] D. Frenkel, H. Lekkerkerker, and A. Stroobants, Nature **332**, 822 (1988).

[50] E. E. Maier, R. Krause, M. Deggelmann, M. Hagenbuchle, R. Weber, and S. Fraden, Macromolecules **25**, 1125 (1992).

[51] A. Leadbetter and P. Wrighton, J. Phys. (Paris) Colloq. **40**, C3 (1979).

[52] M. Deutsch, Phys. Rev. A **44**, 8264 (1991).

[53] P. Davidson, Prog. Polym. Sci. **21**, 893 (1996).

[54] B. J. Lemaire, P. Pannie, J. Gabriel, and P. Davidson, Europhys. Lett. **59**, 55 (2002).

[55] R. Kamien and G. Grest, Phys. Rev. E **55**, 1197 (1997).

[56] A. Saupe, Z. Naturf. **19a**, 161 (1964).

[57] R. Oldenbourg, X. Wen, R. B. Meyer, and D. L. D. Caspar, Phys. Rev. Lett. **61**, 1851 (1988).

[58] P. van der Schoot and T. Odijk, J. Chem. Phys. **93**, 3580 (1990).

[59] P. van der Schoot, J. Chem. Phys. **117**, 3537 (2002).

[60] P. Davidson, D. Petermann, and A. M. Levelut, J. Phys. II **5**, 113 (1995).

[61] A. Paranjpe and V. Kelkar, Mol. Cryst. Liq. Cryst. Lett. **102**, 289 (1984).

[62] V. Kelkar and A. Paranjpe, Mol. Cryst. Liq. Cryst. Lett. **104**, 139 (1987).

[63] A. P. Prudnikov, Y. A. Brychkov, and O. I. Marichev, *Integrals and Series, Vol. 2: Special Functions*, New York: Gordon and Breach, 1990.

[64] G. Watson, *A treatise on the theory of Bessel functions*, Cambridge, University Press, 1922.

[65] A. Tikhonov and A. Samarskiy, *Equations of Mathematical Physics*, Moscow University Press, 1999.

[66] J. G. Kirkwood, J. Chem. Phys **7**, 919 (1939).

[67] J. Henderson, Phys. Rev. E **50**, 4836 (1994).

[68] R. Evans, J. Henderson, D. Hoyle, A. Parry, and Z. Sabeur, Mol. Phys. **80**, 755 (1993).

[69] A. A. Chernov and L. V. Mikheev, Physica A **157**, 1042 (1989).

[70] P. Tarazona, E. Chacon, M. Reinaldo-Falagan, and E. Velasco, J. Chem. Phys. **117**, 3941 (2002).

[71] M. Fisher and B. Widom, J. Chem. Phys. **50**, 3756 (1969).

[72] R. L. de Carvalho, R. Evans, D. Hoyle, and J. Henderson, J. Phys.: Condens. Matter **6**, 9275 (1994).

[73] C. Vega, R. Rull, and S. Lago, J. Chem. Phys. **51**, 3146 (1995).

[74] R. L. de Carvalho and R. Evans, Mol. Phys. **83**, 619 (1994).

[75] R. L. de Carvalho, R. Evans, and Y. Rosenfeld, Phys. Rev. E **59**, 1435 (1999).

[76] W. Brown, R. L. de Carvalho, and R. Evans, Mol. Phys. **88**, 579 (1996).

[77] R. Evans, R. L. de Carvalho, J. Henderson, and D. Hoyle, J. Chem. Phys. **100**, 591 (1994).

[78] R. L. de Carvalho and R. Evans, Mol. Phys. **92**, 211 (1997).

[79] A. Archer and R. Evans, Phys. Rev. E **64**, 041501 (2001).

[80] M. Schmidt, H. Löwen, J. Brader, and R. Evans, J. Phys.: Condensed Matter **14**, 9353 (2002).

[81] A. Archer, C. Likos, and R. Evans, J. Phys.: Condensed Matter **14**, 12031 (2002).

[82] C. Grodon, M. Dijkstra, R. Evans, and R. Roth, J. Chem. Phys. **121**, 7869 (2004).

[83] M. Dijkstra and R. Evans, J. Chem. Phys. **112**, 1449 (2000).

[84] I. Gelfand, M. Kapranov, and A. Zelevinsky, *Discriminants, Resultants and Multidimensional Determinants*, Birkhauser, 1994.

[85] M. Abramowitz and I. A. Stegun, editors, *Handbook of Mathematical Functions with Formulas, Graphs, and Mathematical Tables*, New York: Dover, 1972.

[86] R. D. Groot, J. van der Eerden, and N. Faber, J. Chem. Phys. **87**, 2263 (1987).

[87] J. Haile and C. Gray, Chem. Phys. Lett. **76**, 583 (1980).

[88] M. Allen, C. Mason, E. de Miguel, and J. Stelzer, Phys. Rev. E **52**, R25 (1995).

[89] R. Pynn, J. Chem. Phys. **60**, 4579 (1974).

[90] A. Wulf, J. Chem. Phys. **67**, 2254 (1977).

[91] B. Berne and P. Pechukas, J. Chem. Phys. **64**, 4213 (1972).

[92] J. Parsons, Phys. Rev. A **19**, 1225 (1979).

[93] S. Lee, J. Chem. Phys. **87**, 4972 (1987).

[94] S. S. Cohen, J. Biol. Chem. **144**, 353 (1942).

[95] P. Buining, Y. S. J. Veldhuizen, C. Pathmamamnoharan, and H. N. W. Lekkerkerker, Colloid Surfaces **64**, 47 (1993).

[96] S. Asakura and F. Oosawa, J. Chem. Phys. **22**, 1255 (1954).

[97] A. Vrij, Pure and Appl. Chem. **48**, 471 (1976).

[98] A. P. Gast, C. K. Hall, and W. B. Russel, J. Colloid Interface Sci. **96**, 251 (1983).

[99] H. N. W. Lekkerkerker, W. C. K. Poon, P. N. Pusey, A. Stroobants, and P. B. Warren, Europhys. Lett. **20**, 559 (1992).

[100] E. J. Meijer and D. Frenkel, Phys. Rev. Lett. **67**, 1110 (1991).

[101] E. J. Meijer and D. Frenkel, J. Chem. Phys. **100**, 6873 (1994).

[102] M. Dijkstra, R. van Roij, and R. Evans, Phys. Rev. Lett. **81**, 2268 (1998).

[103] M. Dijkstra, R. van Roij, and R. Evans, Phys. Rev. Lett. **82**, 117 (1999).

[104] M. Dijkstra, R. van Roij, and R. Evans, Phys. Rev. E **59**, 5744 (1999).

[105] M. Dijkstra and R. van Roij, Phys. Rev. Lett. **89**, 208303 (2002).

[106] M. Dijkstra, R. van Roij, R. Roth, and A. Fortini, to be published (2006).

[107] M. Dijkstra, Current Opinion in Colloid & Interface Science **6**, 372 (2001).

[108] M. Dijkstra, J. M. Brader, and R. Evans, J. Phys.: Condens. Matt. **11**, 10079 (1999).

[109] H. Lekkerkerker and A. Stroobants, Nuovo Cimento **D16**, 949 (1994).

[110] P. G. Bolhuis, A. Stroobants, D. Frenkel, and H. N. W. Lekkerkerker, J. Chem. Phys. **107**, 1551 (1997).

[111] P. B. Warren, J. Phys. I France **4**, 237 (1994).

[112] C. W. Trigg, *Mathematical Quickies*, Dover, 1985.

[113] S. H. Walmsley, Chem. Phys. Letters **49**, 390 (1977).

[114] J. G. Gay and B. J. Berne, J. Chem. Phys **74**, 3316 (1981).

[115] B. Martinez-Haya, A. Cuetos, S. Lago, and L. F. Rull, J. Chem. Phys. **122**, 024908 (2005).

[116] D. Frenkel and T. Schilling, Phys. Rev. E **66**, 041606 (2002).

[117] T. Schilling and D. Frenkel, Phys. Rev. Lett. **92**, 085505 (2004).

Summary

In this thesis, we present simulation studies on the structure and phase behavior of colloidal rod suspensions. The interest in these systems is due to the fact that these suspensions form so-called liquid crystalline phases. The properties of liquid-crystalline states are intermediate between those of an isotropic liquid and of a crystalline solid. The discovery of liquid crystals is attributed to Reinitzer and dates back to 1888. However, the industrial needs and introduction of computer simulations as an investigation tool caused a significant progress in understanding the physical properties of liquid crystals in recent years.

The first chapter of this thesis provides a general background on this subject. An overview of experimental results and some key theoretical developments is given and the simulation methods are briefly discussed.

In Chapter 2, the sedimentation and multi-phase equilibria in a suspension of hard colloidal rods are explored by analyzing the (macroscopic) osmotic equilibrium conditions. We observe that gravity enables the system to explore a whole range of phases varying from the most dilute phase to the densest phase, i.e., from the isotropic (I), nematic (N), smectic (Sm), to the crystal (K) phase. We determine the phase diagrams for hard spherocylinders with a length-to-diameter ratio of 5 for a semi-infinite system and a system with fixed container height using a bulk equation of state obtained from simulations. Our results show that gravity leads to multiphase coexistence for the semi-infinite system, as we observe I, I+N, I+N+Sm, or I+N+Sm+K coexistence, while the finite system show I, N, Sm, K, I+N, N+Sm, Sm+K, I+N+Sm, N+Sm+K, and I+N+Sm+K phase coexistence. In addition, we compare our theoretical predictions for the phase behavior and the density profiles with Monte-Carlo simulations for the semi-infinite system and we find good agreement with our theoretical predictions.

Experimental techniques that are frequently used to distinguish the different liquid crystalline phases are e.g. birefringence measurements and X-ray diffraction. The accuracy of measuring the nematic order from X-ray diffraction is the subject of Chapter 3. The determination of the nematic order parameter S and the orientational distribution function (ODF) from scattering data involve severe approximations. The validity of these are studied here using Monte-Carlo simulations of hard spherocylinders with an aspect ratio of 15 for varying densities in the isotropic and nematic phase. The "exact" ODF of the rods, the "exact" value of S, and the scattered intensity $I(\vec{q})$ are determined directly in simulation. In addition, we determine the ODF and S from the simulated scattered intensity which includes spatial and orientational correlations of the particles. We investigate whether correlations present in the interparticle scatter influences the determination of the single particle orientational distribution function by comparing the results obtained from scattering with the “exact” results measured directly in our simulations. We find that the nematic order parameter determined from the scattered intensity underestimates the

actual value by 2-9$\%$. We also find that the values of S and the ODF are insensitive to the absolute value of the scattering vector for $1.2\pi < |\vec{q}|D < 2\pi$ which agrees well with the assumption proposed by Leadbetter that $I(q, \psi)$ along the equatorial arc is independent of $|\vec{q}|$. We also observe that the best fit of the "exact" ODF is given by the Maier-Saupe distribution when nematic director fluctuations are ignored, while the Gaussian distributions provides the best fit when these fluctuations are included.

The structure of a fluid can be described by means of correlation functions. The correlation functions determine the thermodynamics of a system, while the asymptotic behavior of the pair correlation function is important for understanding the interfacial properties. The asymptotic behavior of the total correlation function $h(1, 2)$ in molecular fluids is investigated in Chapter 4. To this end, we expand the angular dependence of $h(1, 2)$ and the direct correlation function $c(1, 2)$ in the Ornstein-Zernike equation in a complete set of rotational invariants. We show that all the harmonic expansion coefficients $h_{l_1 l_2 l}(r)$ are governed by a common exponential decay length and a common wavelength of oscillations in the isotropic phase. We determine the asymptotic decay of the total correlation functions by investigating the pole structure of the reciprocal (**q**-space) harmonic expansion coefficients $h_{l_1 l_2 l}(q)$. The expansion coefficients in laboratory frame of reference $h_{l_1 l_2 l}(r)$ are calculated in computer simulations for an isotropic fluid of hard spherocylinders. We find that the asymptotic decay of $h(1, 2)$ is exponentially damped oscillatory for hard spherocylinders with a length-to-diameter ratio $L/D \leqslant 10$ for all statepoints in the isotropic fluid phase. We compare our results on the pole structure using different theoretical Ansätze for $c(1, 2)$ for hard ellipsoids. The theoretical results show that the asymptotic decay of $h(1, 2)$ is exponentially damped oscillatory for all elongations of the ellipsoids. However in the limit $L/D \to \infty$ the dominant poles for Onsager model are monotonic for all densities in the isotropic phase.

Finally, Chapter 5 is devoted to the phase behavior of a mixture of colloidal hard rods with a length-to-diameter ratio of $L/\sigma_c = 5$ and non-adsorbing ideal polymer. We map our binary mixture onto an effective one-component system by integrating out the degrees of freedom of the polymer coils. We derive a formal expression for the exact effective Hamiltonian of the colloidal rods, i.e., it includes all effective many-body interactions and it is related to the exact free volume available for the polymer. We determine numerically on a grid the free volume available for the ideal polymer coils "on the fly" for each colloidal rod configuration during our Monte-Carlo simulations. This allows us to go beyond first-order perturbation theory, which employs the pure hard-rod system as reference state. We perform free energy calculations for the isotropic, nematic, smectic, and crystal phase using thermodynamic integration. We use common tangent constructions at fixed polymer fugacities to map out the phase diagram. We determine the phase behavior for size ratios $q = \sigma_p/\sigma_c = 0.15$, 0.5, and 1, where σ_p is the diameter of the polymer coils. We compare the phase diagrams based on the full effective Hamiltonian with those obtained from first-order perturbation theory, from simulations using the effective pair potential approximation to the effective Hamiltonian and with those based on an empiric effective depletion potential for the rods. We find that the many-body character of the effective interactions stabilizes the nematic and smectic phase for large q, while the effective pair potential description overestimates the attractive interactions and favors, hence, a broad isotropic-crystal coexistence.

Samenvatting

In dit proefschrift presenteren we computersimulatie-studies van de structuur en het fasengedrag van suspensies van colloïdale staafjes. De interesse in deze systemen komt voort uit hun vermogen om zogenaamde vloeibaar-kristallijne fasen te vormen. De eigenschappen van de vloeibaar-kristallijne toestand liggen tussen die van een isotrope vloeistof en een kristallijne vaste stof in. De ontdekking van vloeibare kristallen wordt toegeschreven aan Reinitzer en gaat terug tot 1888. Echter, de industriële behoefte en de introductie van computersimulaties als onderzoeksmethode hebben in recente jaren geleid tot een significante vooruitgang in ons begrip van de fysische eigenschappen van vloeibare kristallen.

Het eerste hoofdstuk van dit proefschrift geeft de algemene achtergrond van dit onderwerp. Er wordt een overzicht gegeven van de experimentele resultaten en de belangrijkste theoretische ontwikkelingen. Daarnaast worden de simulatiemethoden kort besproken.

In hoofdstuk 2 onderzoeken we de sedimentatie en meerfasenevenwichten in een suspensie van harde colloïdale staven door de (macroscopische) osmotische evenwichtscondities te analyseren. We zien dat de zwaartekracht er voor zorgt dat het systeem een heel scala van fasen vertoont, reikend van de meest verdunde tot de meest dichte fase. Dit betekent dat zowel de isotrope (I), nematische (N), smectische (Sm) als de kristallijne (K) fase kan worden waargenomen. We verkennen het fasediagram van harde staven met een lengte-diameter verhouding van 5 door de uit simulaties verkregen bulk-toestandsvergelijking te gebruiken. Hierbij bekijken we een semi-oneindig systeem en een systeem met een vaste reservoirhoogte. Onze resultaten laten zien dat de zwaartekracht leidt tot meerfasencoexistentie. Voor het semi-oneindige systeem vinden we naast de isotrope fase (I), ook coexistentie tussen I+N, I+N+Sm, en I+N+Sm+K. Het eindige systeem vertoont een nog rijker fasegedrag, in dit geval zien we de volgende (combinaties van) fasen: I, N, Sm, K, I+N, N+Sm, Sm+K, I+N+Sm, N+Sm+K en I+N+Sm+K. Tenslotte vergelijken we onze theoretische voorspellingen voor het fasengedrag en de dichtheidsprofielen met Monte-Carlo simulaties van het semi-oneindige systeem en vinden daarbij goede overeenkomsten.

Enkele experimentele technieken die vaak gebruikt worden om de verschillende fasen van een vloeibaar kristal te onderscheiden zijn dubbelbreking en röntgenverstrooiing. In hoofdstuk 3 wordt bestudeerd hoe nauwkeurig de nematische ordening bepaald kan worden uit röntgenverstrooiingsdata. Bij het bepalen van de nematischeordeparameter S en de oriëntationeledistributiefunctie (ODF) uit verstrooiingsdata worden er grove aannames gemaakt. De geldigheid van deze aannames wordt hier bestudeerd met behulp van Monte Carlo simulaties voor verschillende dichtheden in een systeem van harde spherocilinders in zowel de isotrope als de nematische fase. De verhouding tussen de lengte en de diameter van de spherocilinders is 15. De 'exacte' ODF van de staafjes, de 'exacte' waarde voor S en de verstrooide intensiteit $I(\vec{q})$ worden direct gemeten in simulaties. Verder onderzoeken we of de correlaties in de onderlinge verstrooiing tussen de deeltjes invloed hebben op de bepaling van de ODF van één enkel deeltje. Dit doen we door de uit de verstrooiing afgeleide resultaten voor de ODF te vergelijken met de 'exacte' resultaten uit de simulaties. We concluderen dat de nematischeordeparameter die uit de verstrooiingsdata gehaald wordt 2-9$\%$ kleiner is dan de eigenlijke waarde. We concluderen verder dat de waarde van S en de ODF niet afhangen van de absolute waarde van de verstrooiingsvector $\vec{q}$, mits $1.2\pi < |\vec{q}|D < 2\pi$. Dit komt overeen met de door Leadbetter voorgestelde aanname dat $|I(q,\psi)|$ langs de (equatoriale arc) onafhankelijk is van de lengte van de verstroоingsvector $\vec{q}$ ($|\vec{q}|$). We merken daarnaast op dat de 'exacte' resultaten het best gefit kunnen worden met behulp van de Maier-Saupeverdeling, mits de fluctuaties van de nematische voorkeursrichting genegeerd worden. Als die fluctuaties wel meegenomen worden, dan is het juist een Gaussische verdeling die de beste fit oplevert.

De structuur van een vloeistof kan worden beschreven door middel van correlatiefuncties. Deze correlatiefuncties bepalen de thermodynamica van het systeem. Het asymptotische gedrag van de paar-correlatiefunctie is belangrijk voor het begrip van vloeistoffen in de buurt van grensvlakken. Het asymptotische gedrag van de totale paar-correlatiefunctie $h(1,2)$ in moleculaire vloeistoffen word onderzocht in hoofdstuk 4. Dit doen we door de hoekafhankelijkheid van de totale en de directe paar-correlatiefunctie (uit de Ornstein-Zernikevergelijking) te expanderen in een complete verzameling van rotatie invarianten. We laten zien dat in de isotrope fase al de harmonische coëfficiënten $h_{l_1l_2l}(r)$ van deze expansie dezelfde vervalsexponent en dezelfde golflengte hebben. We bepalen het asymptotische verval van de totale correlatiefunctie door de structuur van de polen van de coëfficiënten van de reciproke harmonische expansie (in de $\mathbf{q}$-ruimte) $h_{l_1l_2l}(q)$ te onderzoeken. Deze coëfficiënten $h_{l_1l_2l}(r)$, in het laboratoriumstelsel, worden uitgerekend door middel van computersimulaties van een isotrope vloeistof van harde spherocilinders. We vinden dat het asymptotische gedrag van $h(1,2)$ exponentieel gedempt en oscillerend afvalt voor harde spherocilinders met een lengte-diameter-verhouding van $L/D \leqslant 10$ voor alle toestanden in de isotrope vloeistof. We vergelijken onze resultaten met verschillende theoretische aannames voor $c(1,2)$ van harde ellipsoiden. Deze theorieën voorspellen dat het verval van de totale correlatie $h(1,2)$ exponentieel gedempt en oscillerend is voor alle lengte-diameter-verhoudingen van ellipsoiden. Echter, in de limiet $L/D \to \infty$ zijn de dominante polen van het Onsager model monotoon voor alle dichtheden in de isotrope phase.

Tenslotte bestuderen we in hoofdstuk 5 het fasengedrag van een mengel van colloïdale staafjes met een lengte-diameter verhouding van 5 en niet-adsorberende ideale polymeren. We beschouwen het binaire mengsel als een effectief een-component systeem, waarin de polymeer vrijheidsgraden uitgeïntegreerd zijn. We leiden een formele uitdrukking af voor de exacte effectieve Hamiltoniaan van de colloïdale staafjes, die alle effectieve veeldeeltjes interacties bevat en gerelateerd is aan het vrije volume dat beschikbaar is voor het polymeer. We bepalen numeriek op een rooster het vrij beschikbare volume voor het polymeer voor elke configuratie van staafjes tijdens een Monte-Carlo simulatie. Hierdoor kunnen we verder gaan dan eerste-orde storingsrekening, waarbij het pure systeem van harde staafjes als referentie wordt gebruikt. We berekenen de vrije energie voor de isotrope, nematische, smectische, en kristallijne fase met behulp van thermodynamische integratie. De diameterverhoudingen van de polymeer kluwens en de staafjes zijn 0.15, 0.5, en 1. We vergelijken de fasendiagrammen gebaseerd op de exacte effectieve Hamiltoniaan met die verkregen uit eerste-orde storingsrekening, uit simulaties met de effectieve paar potentiaal en met een empirische effectieve paar potentiaal voor de staafjes. We vinden dat de veel-deeltjes interacties de nematische en de smectische fase stabiliseren voor grote diameterverhoudingen, terwijl de effectieve paar potentiaal beschrijving de attractieve interacties overschat, wat een brede isotroop-kristal overgang geeft.

List of publications

This thesis is based on the following publications:

- S.V. Savenko and M. Dijkstra, *Phase behavior of a suspension of colloidal hard rods and non-adsorbing polymer*, submitted
- S.V. Savenko and M. Dijkstra, *Asymptotic decay of the pair correlation function in molecular fluids: application to hard rods*, Phys. Rev. E, 72, 021202, 2005
- S.V. Savenko and M. Dijkstra, *Sedimentation and multiphase equilibria in suspensions of colloidal hard rods*, Phys. Rev. E, 70, 051401, 2004
- S.V. Savenko and M. Dijkstra, *Accuracy of measuring the nematic order from intensity scatter: A simulation study*, Phys. Rev. E, 70, 011705, 2004

Other publications:

- V.T. Shvets, S.V. Savenko and V.B. Rogankov *Perturbation theory for the conductivity of metallic hydrogen*, submitted
- V.T. Shvets, S.V. Savenko, S. Datsko, *The electroconductivity of the liquid alloys of transition metals*, Condensed Matter Physics, 7, 275-284, 2004
- V.T. Shvets, S.V. Savenko, S. Datsko, *Perturbation theory for electrical resistivity of liquid transition metals*, Condensed Matter Physics, 5, 511-522, 2002

Acknowledgements

I would like to express my gratitude to all the people I met during the years of my PhD. I have gained something from all of you, thanks. However I feel some of the people should be mentioned separately. First of all I want to acknowledge my thesis advisor Marjolein Dijkstra, who introduced me to the field of computer simulations. She was the source of motivation and scientific inspiration for me and her patience was really beyond belief. I also would like to thank my promotor prof. Alfons van Blaaderen who guided my research. Unfortunately we did not collaborate closely, so the limits of his patience are left unexplored yet. Next I like to thank all the people whose help made my scientific life easier, namely Rene van Roij, Mathias Schmidt, Kostya Shundyak, Lidiya Mykhaylovskaya, Anti-Pekka Hynninen and all the people from Ornstein Lab. I also appreciate much the support of Prof. Valerii Shvets as well as Prof. Alexander Zatovskiy whose opinion was crucial for my decision to do PhD instead of military service. It was my pleasure to provide assistantship to Dr. Ernst van Faassen on his problem classes, his attitude to the science influenced me a lot.

The next category is the people with whom I shared the roof. Those are Kostya and Lyuda and Yura Shundyak, Carmen Zoldeci, and Alex Sokolov. And certainly the people with whom (wa-hoo-hum) I shared my time: Vovan Shchetinin is acknowledged for a great portion of chaos he is kindly sharing with those around him, Vlad Ivanov for the rare but resulting meetings, Sasha Argonskaya for instructive talks, Andrey Kirillyuk for meatball talks, Petruha Yakovlev and Marat for beauty of the mountains, Sergei Dobrovolskiy for the ice-axe, Masha Sholkina for Zen lessons, Dima Mazurenko for the chess lessons, Masha Zhuravleva for a good mood, Misha Korobeinik for the proper mood, Olegi Selikhanovich and Kozlovskiy for their hinterland service. Thanks to these people go without any explanation: Yura Vatis and Elena Svetnaya, Shurik and Natasha Zelinskie, Max and Olechka Maximovy and Marie Shvartsapel.

And finally my deepest acknowledgements go to my family members. Mom and Dad, Grand- Mom and Dad, uncles and aunts... the words are too slim to express how slim they are, but as you have been learning to understand me since I did not use any words you probably know what I would like to say. Alina and Margarita, my wife and daughter, you get my warmest gratitude for unconditional support in all my undertakings, thank you.

Curriculum Vitae

The author of this thesis was born on 27-th of December 1978 in Odessa, USSR. In 1995 he finished the Physics class in the Richelieu Lyceum in Odesa Ukraine. The same year he continued his education at Odessa State University in the Faculty of Physics. In June 2000 he obtained his Master of Science degree in Theoretical Physics. From 2000 to 2002 he was working as a junior research fellow at the Mathematical department in Odessa Low Temperature Academy, where he was involved in research of electron transport phenomena in disordered metals. In 2002 he started his PhD research in the Soft Condensed Matter group of prof. dr. Alfons van Blaaderen, Utrecht University, in the Netherlands. The results of this research are presented in this thesis and are published in high-impact factor journals.